Master thesis and internship[BR]- Master's thesis : Achromatic phase shifter in nulling interferometry for exoplanet detection[BR]- Integration internship

Auteur : Fayt, Casimir
Promoteur(s) : Loicq, Jerome
Faculté : Faculté des Sciences appliquées
Diplôme : Master en ingénieur civil en aérospatiale, à finalité spécialisée en "aerospace engineering"
Année académique : 2020-2021
URI/URL : http://hdl.handle.net/2268.2/11604

LIÈGE université

CENTRE SPATIAL DE LIÈGE

Achromatic Phase Shifter in nulling interferometry for exoplanet detection

University of Liège - School of Engineering and Computer Science

Master's thesis carried out to obtain the degree of Master of Science in Aerospace Engineering specialised in Space and Optics Engineering

Casimir Fayt

Supervisor
Pr Jérôme Loicq

Co-supervisor
Ir Colin Dandumont

Research Center
CSL - Centre Spatial de Liège

Academic year
2020 - 2021

Abstract

"Achromatic Phase Shifter (APS) in nulling interferometry for exoplanet detection" by Casimir Fayt. University of Liège (ULiège), Master's degree in aerospace engineering with a focus on space engineering, 2020-2021.

Nulling interferometry is a recent technology in exoplanet detection and has enormous potential for future discoveries. Only achieved in terrestrial telescopes, its implementation in space could give rise to a new momentum in exoplanet science. The main figure of merit of the nulling interferometer is the nulling ratio, which describes the intensity ratio between the bright and dark fringes.. Clear measurements imply a ratio greater than the radiance ratio between the star and the planet (typically in the order of 10^4).

The nulling ratio is deeply impacted by the phase shifter. In the context of implementing this technique within a new observation satellite, the different phase shifter concepts must be updated and carefully selected. This work is part of this approach.

Various existing concepts are compared before selecting the most promising candidates: dispersive prisms, Fresnel rhombs, and integrated optics. These three systems are investigated and simulated to obtain their performance. Several constraints such as size, scientific requirements, or manufacturing considerations are taken into account. The different mission sizes considered define four spectral bands across which the phase shifter must be tested: [0.3 - 0.7], [0.9 - 2.1], [1.5 - 3.5], [2.6 - 6.4] microns.

For the smallest mission sizes, wedge prisms and Fresnel rhombs seemed unsuitable for the size requirement. For larger missions, the wider spectral band implies long propagation in a medium such that the intrinsic material dispersion seems to become problematic. Those two concepts were, therefore, quickly discarded because of room considerations and spectral bandwidth, and considering the advantages offered by integrated optics.

Considering the integrated optics, an algorithm based on a mode solver for dielectric rectangular waveguide was computed. A polynomial fit of the effective index difference between waveguides of different widths allowed to define a matrix system. Solving this system provides the length of the elements resulting in the desired phase shift as achromatic as possible. Integrated phase shifters in silica of fewer than four centimetres could provide the required rejection ratio for the two first spectral bands. For the two larger bands, the integrated optics do not meet the requirement within a technically acceptable size. The mirror approach seems the most promising concept for those spectral bands because of the intrinsic achromaticity of metallic reflections.

Keywords

Achromatic phase shifter, integrated optics, satellite, nulling interferometry, exoplanet, astronomy.

Résumé

"Achromatic Phase Shifter (APS) in nulling interferometry for exoplanet detection" by Casimir Fayt. Université de Liège (ULiège), Master en ingénierie aérospatiale à finale ingénierie spatiale, 2020-2021.

L'interférométrie de nulling est une technologie récente avec un potentiel énorme pour de futures découvertes. Seulement implémentée dans des téléscopes terrestres, sa mise en place sur des satellites pourrait donner naissance à un nouvel essor dans la science des exoplanètes. La principale figure de mérite de l'interféromètre de nulling est son quotient d'annulation qui décrit le rapport d'intensité entre les franges constructrives et destructrives. Des mesures claires nécessitent un quotient supérieur au rapport de radiance entre l'étoile et la planète (typiquement de l'ordre de 10^4).

Le quotient de nulling dépend fortement du déphaseur. Cet élément est responsable du déphasage entre les champs collectés, qui est d'une importance capitale dans l'annulation, et doit montrer stabilité temporelle et achromaticité spectrale. Dans le contexte de l'implémentation de cette technique dans un nouveau satellite d'observation, les différents concepts de déphaseur doivent être revus et sélectionnés soigneusement. Ce travail s'inscrit dans cette approche.

Différents concepts existants sont comparés avant de sélectionner les candidats les plus prometteurs : les prismes dispersifs, les rhomboèdres de Fresnel, et l'optique intégrée. Ces trois systèmes sont étudiés et simulés dans le but d'obtenir et de comparer leurs performances. Plusieurs contraintes sont prises en compte comme la taille, les spécifications scientifiques, ou les considérations de fabrication. Les différentes tailles de mission considérées définissent quatre bandes spectrales sur lesquelles le déphaseur doit être testé : [0.3 - 0.7], [0.9 - 2.1], [1.5 - 3.5], [2.6 - 6.4] microns.

Comme les prismes dispersifs et rhombs de Fresnel impliquent une longue propagation dans un milieu, la dispersion intrinsèque du matériau est problématique étant donné les largeurs spectrales considérées. Ces deux concepts ont été rapidement abandonnés de par leur encombrement et les largeurs spectrales, et au vu des avantages proposés par l'optique intégrée.

Concernant l'optique intégrée, un algorithme basé sur un solveur de mode pour des guides d'onde rectangulaires diélecriques a été programmé. Un fit polynomial sur la différence d'indice effectif entre des guides d'onde d'épaisseur différente permit de définir un système matriciel. Sa résolution calcule la longueur des éléments nécessaires pour le phase shift visé aussi achromatique que possible. Des déphaseurs intégrés en silice de moins de quatre centimètres pourrait générer le quotient d'annulation pour les deux premières bandes spectrales. Pour les deux suivantes, l'optique intégrée ne satisfait pas les spécifications en restant de taille techniquement réalisable. L'approche des miroirs semble le concept le plus intéressant pour ces bandes spectrales grâce à l'achromaticité intrinsèque des réflections métalliques.

Mots-clefs

Déphaseur achromatique, optique intégrée, satellite, interférométrie de nulling, exoplanète, astronomie.

Acknowledgements

First things first, I have to thank the people who taught me the most about space optics, and shared a lot of their time this year. Professor Loicq and Colin, thanks a lot for your help and the knowledge you gave me. This field is surely of the uttermost interest to me and confirms my desire to engineer by looking up.

At CSL, thanks also to Juriy Hastanin and Victor Laborde for your time about the integrated optics elements or about the OptiFDTD software.

Special thanks as well to Pr. Labeye and Pr. Labadie, for their insight about their work. Shedding light on the questions of an unknown MA2 student is very kind and was totally helpful.

From a more humorist and personal point of view, thanks to the unbeatable, unrivalled, incomparable, and unsurpassed BrolKot team : Armand, Eliott and Hadrien. Thanks for this whole year: between chess games, interminable ping-pongs, shitty shows like Mars, great shows like TH2H, amazing shows like Salvation, countless DBs and packs of cheese, you made this monotonous period quite enjoyable. I would feel angry at myself if ever I forgot to mention two of the best living beings on this planet : Rambo and Thérèse. Stay the same, keep the hard work. Some day, it will pay off, and I'll be there !

Little thought as well for AA who still let me pursue almost weekly dwellings and with whom I finally reached the quintessence.

Final thanks to my family who allowed me to pursue for two more years. The field is definitely the one I was looking for, it was not in vain ! I promise, now it is over.

Table of contents

List of Tables

List of Figures

Acronyms

SYNAPSE SYmmetric Nuller for Achromatic Phase Shifters Evaluation 29

AIC Achromatic Interfero Coronagraph 34

APS Achromatic Phase Shifter i, ii, v, viii, ix, xi, xii, 1, 2, 22, 26, 27, 31, 32, 38, 39, 42, 43, 46, 47, 61, 67, 73, 75, 78, 81–92, 94, 95

CSL Centre Spatial de Liège iii, 1

EMA WMS Extended Marcatili's Approach Waveguide Mode Solver xii, 77, 79, 80, 90

ESA European Space Agency 2, 19, 21, 22, 29, 32, 94

ESPRESSO Echelle SPectrograph for Rocky Exoplanet and Stable Spectroscopic Observations 11

ESTEC European Space Research and Technology Centre 29

FC-APS Focus Crossing Achromatic Phase Shifter 29, 33, 34

FDTD Finite Difference Time Domain vi, 91, 95

FKSI Fourier-Kelvin Stellar Interferometer 1, 2, 21, 47, 94

FR-APS Field Reversal Achromatic Phase Shifter xi, 29, 30, 33, 34

FV WMS Full Vectorial Waveguide Mode Solver 77, 80

FWHM Full Width at Half Maximum 6

GR General Relativity 12

GRB Gamma-Ray Burst 19

HMW Hollow Metallic Waveguide 64–67

HMW Hollow Metallic Waveguides vi, viii, xii, 43, 61, 64, 67, 68, 70

HST Hubble Space Telescope 12

LED Light-Emitting Diodes 50

LIFE Large Interferometer For Exoplanet v, 2, 21, 94

LRG Luminous Red Galaxy 12

NA Numerical Aperture 69, 70

NASA National Aeronautics and Space Administration 2, 20

NPOI Navy Precision Optical Interferometer iv, x, 20

OPD Optical Path Difference 22, 27, 32, 33, 45, 47–49

PROBA PRoject for On-Board Autonomy 1, 47

SNR Signal-to-Noise Ratio 30

TE Transverse Electric vi, 64–66, 70–72

TEM Transverse ElectroMagnetic 64

TIR Total Internal Reflection xi, 35, 36, 46, 57, 59, 68

TM Transverse Magnetic vi, 64, 65

TPF Terrestrial Planet Finder iv, 20, 94

TPF-C Terrestrial Planet Finder Coronograph 20

TPF-I Terrestrial Planet Finder Interferometer x, 2, 20, 21

VLT Very Large Telescope iv, x, 19

VLTI Very Large Telescope Interferometer 19

Introduction

For a long time, scientists have tried to gain information by comparison and study of similar systems. This way forward led to complex sample collections, e.g. at the bottom of oceans or top of volcanoes. Turning towards astronomy and more particularly the study of star-planets systems, interesting knowledge resides in the detection and measurement of other planets. For a long time, our solar system has been the only examples of star and planets we could observe, and not until 1969 were we able to set foot on another celestial body. Yet it was the Moon, only a rock throw away when compared to usual astronomical distances. Setting foot on another planet is the next objective of space exploration pursued by pioneer companies and national agencies, with the expected first human on Mars before 2030.

At the cost of severe technological challenges, astronomy tries to answer big questions such as how old is the Universe, how does it evolve, are there other Earth-like planets, could we live on other planets, etc. The interrogations related to the presence, behaviour, and study of planets orbiting around other stars and potentially habitable all are part of the exoplanet detection and characterisation branch of astronomy.

The knowledge gained through numerous missions devoted to exoplanets allows learning more about the genesis of planets and star-planet(s) systems in general as well as planets formation. The collected data helps to validate or discard models and improve simulations. Furthermore, the ever-advancing technology that we humans reach sets a wind flowing forward new discoveries and let shine an encouragingly bright future for such missions.

This work is a continuation of a project of the Centre Spatial de Liège (CSL). This project aims at studying the feasibility and prospects of exoplanet detection via nulling interferometry in a satellite of various configurations. Colin Dandumont *et al.* have studied the performance and detection yield of such project in recent papers. [1] They decided to set several operating spectral bands related to different mission sizes:

	CubeSat 6U	CubeSat 12U	PROBA-size	FKSI concept
Optimal wavelength (μm)	0.5	1.5	2.5	4.5
Waveband (μm)	$0.3 - 0.7$	$0.9 - 2.1$	$1.5 - 3.5$	$2.6 - 6.4$

Operating wavelength according to mission size. [1]

Work description

The main work achieved during this thesis is an update of the previously proposed solutions for an Achromatic Phase Shifter and an evaluation of their performance regarding the specifications of this particular project.

Many concepts have already been discovered. Theses concepts were the subject of many studies and reports during the early 2000s. Those works were in the frame of monumental projects launched by large associations such as ESA (1) and NASA (2), for example: Pegase (1), Darwin (1), Fourier-Kelvin Stellar Interferometer (FKSI) (2), TPF-I (2), Darwin (1). The projects were abandoned around 2010 before a new interest started around 2017 with the Large Interferometer For Exoplanet (LIFE) project started by ESA.

The first step was to gather informations about all concepts and look for further advancements. Then a trade-off concerning the specifications of this mission elected three laureates for further development. Those three concepts were more deeply investigated, with a particular attention to the integrated optics.

Work articulation

This manuscript starts with an explanation of the exoplanet detection methods in Chapter 1. Those methods for detection (radial velocity, transit, gravitational microlensing, coronagraphy) are the main tools used so far to determine the presence of an exoplanet. Afterwards, the characterisation step of the process may begin.

Then Chapter 2 will present an insight about nulling interferometry, one of the most promising detection methods. The Achromatic Phase Shifter (APS) is the subject of this work. It takes a predominant place in the systems performance outputs focusing on nulling interferometry. The concept, implementation, theory and requirements are presented in order to give the reader a strong understanding of the objectives of this work.

As the two previous chapters have provided the background knowledge needed, Chapter 3 gets to the heart of the matter by detailing the APS concepts that scientists have come up with during the design phases of several interferometric projects. The concepts are evaluated according to the specific performance and requirements of the mission this work focuses on, and a comparison is performed in order to determine a minimal number of interesting concepts to be further deep investigated.

Chapter 4 and 5, delineate the study made on the three selected concepts : dispersive plates in the shape of wedged prisms, Fresnel rhombs and integrated optics respectively. The two firsts have been discarded while the third one seems promising. Those studies are only simulation due to the pandemic having restrained access to testing facilities and laboratories. Performances are evaluated mainly in terms of phase shift defect and achromatism, to define a rejection ratio on the spectral band of interest.

The results of the simulation for the integrated optics are presented in Chapter 6 together with prospects for further steps.

Chapter 1

Exoplanet detection

By definition, an exoplanet is a planet that orbits around a star different than our Sun. Their shape, size, nature, position, everything can be hugely different, from a radius $R \approx .01\ R_\oplus$ to $R \approx 40\ R_\oplus$[1]. [2] They can show rocky surface as the four first of the solar system, be gaseous as our giants, ice oceans, etc. The closest one is orbiting the star Proxima Centauri, at a distance of around 4.24 ly or approximately 1.3 pc. This corresponds to $40\,000$ billion kilometres, more than $250\,000$ AU (1 AU is defined as $149\,597\,870.7$ km and corresponds roughly to the average distance between the Earth and the Sun). Considering the fact that the farthest humans have ever been is to the Moon (approximately $380\,000$ km) the time when humans will set foot on an exoplanet has not yet come.

Nevertheless, they represent a considerable source of knowledge about the science of the Universe, and recently humanity has finally mastered technology able to sense and measure them remotely.

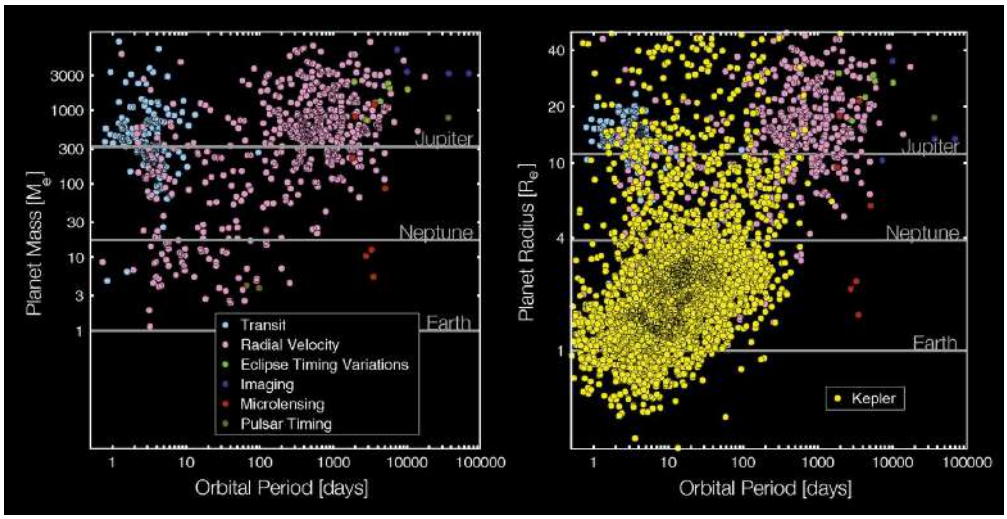

Figure 1.1: Exoplanet discovered outside Kepler program (left) plotted as mass versus orbital period and coloured according to the detection technique. The planetary radius is obtained by a simplified relation (right), and the Kepler discoveries (yellow) are added for comparison. [2]

[1] $R_\oplus$ is the radius of the Earth, defined as $6.3781\ 10^6$ meters.

1.1 The challenges

The first and foremost[2] obstacle to exoplanet observation is the mitigation of the starlight. The star and planets are usually assumed as black bodies. Under this assumption their radiance depending on their wavelength and temperature is given by Planck's law:

$$B(\lambda, T) = \frac{2hc^2}{\lambda^5} \frac{1}{e^{\frac{hc}{\lambda k_B T}} - 1}. \tag{1.1}$$

In this equation $h \approx 6.6\,10^{-34}$ Js is Planck's constant, $c \approx 3\,10^8$ m/s is the speed of light in the vacuum and $k_B \approx 1.38\,10^{-23}$ J/K is the Boltzmann constant. The radiance $B_\lambda(T)$ is usually given in W.m^{-2}.µm^{-1}.sr^{-1}. For example, the solar flux can be very well approximated by Planck's law with a temperature of 5 777 K as shown in Fig. 1.2a. The fit of the black body curve to the measured solar spectral radiance allowed in fact to estimate the solar surface temperature.

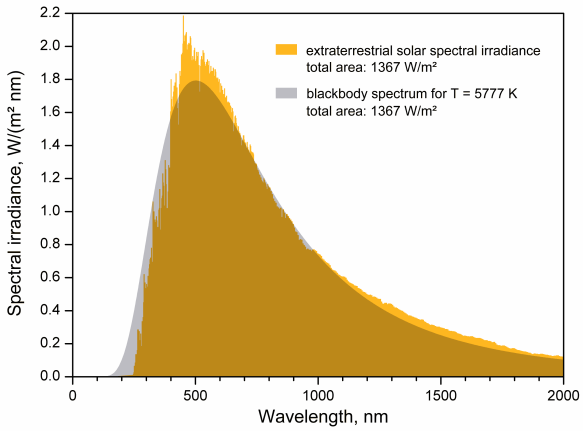

(a) Black body at 5 777 K and solar radiance. [3]

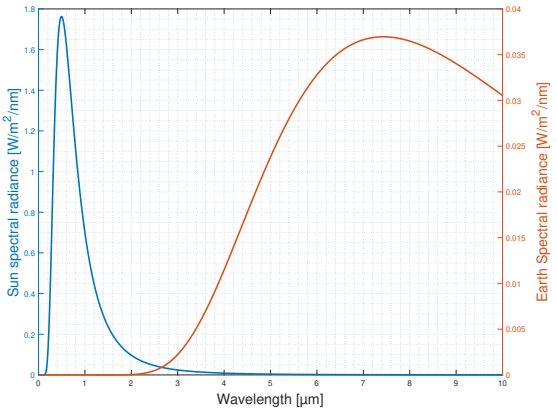

(b) Black bodies radiance at Earth and Sun surface temperature.

Figure 1.2: Black bodies spectral radiance.

As shown in Fig. 1.2b the spectral radiance have different peak wavelengths. The spectral bands of interest depend on the scientific objectives and the mission parameters, and in our case extend up to 6 µm, which is lower than the peak wavelength of the Earth black body spectral radiance. But most importantly the radiance magnitudes are greatly different. This leads to the fact that most of the detected planet flux comes from starlight reflection at the considered wavelengths.

[2]Actually, the angular resolution is also a very challenging aspect but is not the subject of this work. As a quick example, the nearest planetary system is around Proxima Centauri, a star 4.24 light-year away. With a radius estimated to approximately 1.1 $R_\oplus$, the telescope needs an angular resolution of approximately $14\ 10^{-3}$ arcsec. With an estimated surface temperature around 3 000 K its peak wavelength is $\lambda_{peak} \approx 1$ µm. Neglecting atmospheric turbulence (introducing defect corrected by adaptive optics) the angular resolution requires at the peak wavelength a telescope diameter of 18 m to satisfy the Rayleigh criterion.

Taking an example of a star with luminosity L_* we can define its stellar flux as:

$$F_* = \frac{L_*}{4\pi\, R^2}. \tag{1.2}$$

This allows defining the portion of the stellar flux impacting a planet of radius R_P on an orbit[3] with semi-major axis $a_p = r_{orb}$ as:

$$L_p = \alpha\, F_* \pi R_P^2. \tag{1.3}$$

The coefficient α is called the albedo and is defined as the fraction of stellar light reflected by the planet. The luminosity ratio is thus given by:

$$\frac{L_p}{L_*} = \frac{\alpha}{4}\left(\frac{R_P}{r_{orb}}\right)^2. \tag{1.4}$$

Assuming an albedo coefficient of 0.5[4], the intensity ratio for planets of radius ranging from $0.1\ R_\oplus$ to $10\ R_\oplus$ on a orbit of radius 0.1 AU to 10 AU around a Sun-like star is plotted in Fig. 1.3.

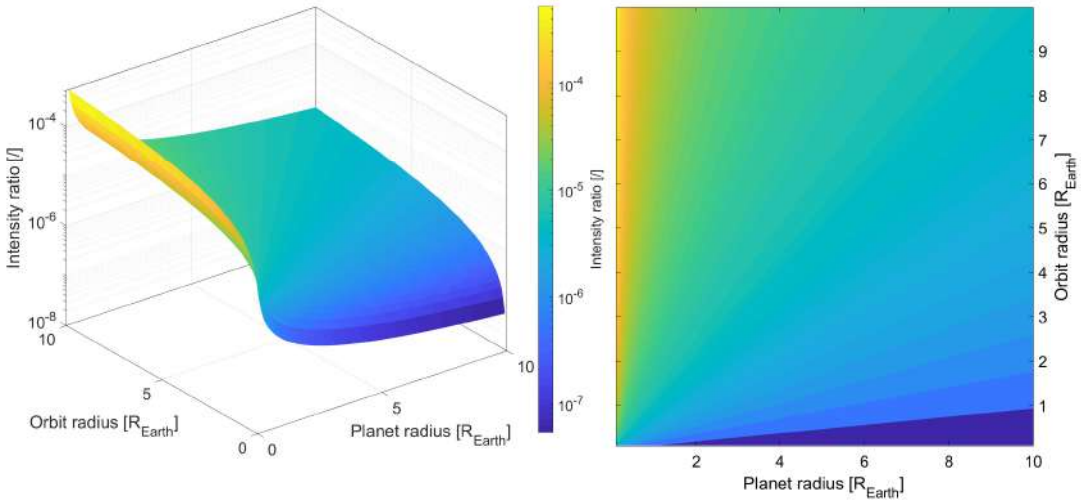

Figure 1.3: Intensity ratio between a Sun-like star and a planet with radius $R \in [.1;\ 10]\ R_\oplus$ on a circular orbit of radius $r_{orb} \in [.1;\ 10]$ AU.

The magnitude of the intensity ratio ranges at very low values. This computation results from very simple calculations to provide an order of magnitude but shows the wide disparity in photon flux between a star and its companion[5].

[3]The orbit is assumed circular for simplicity. In the most general case, an elliptic orbit requires adding a corrective term. The term is given by the ratio of the elliptic surface of revolution of the orbit divided by the surface of the solid sphere.

[4]This value is based on the different measured albedos of the solar system planets.

[5]In this work, the target rejection ratio is 10^4.

The problem, therefore, resides in the glare of the star: the stellar flux mixes with the planetary flux. In most cases, the starlight is too bright and the planet signal is overwhelmed: it is undetectable.

To illustrate such challenge, one may plot the intensity profile of a star. If we assume having an image of an isolated star on a black background, its radial intensity profile may be approximated by a theoretical fit such as: [4]

$$f(r) = I_0 \left(1 + \kappa\, r^2 + r^{3.33}\right)^{-1}. \quad (1.5)$$

The κ parameter accounts for the angular resolution of the star and can be linked to the FWHM of the intensity distribution[6]. The agreement between experimental data and the fit is shown in Fig. 1.4.

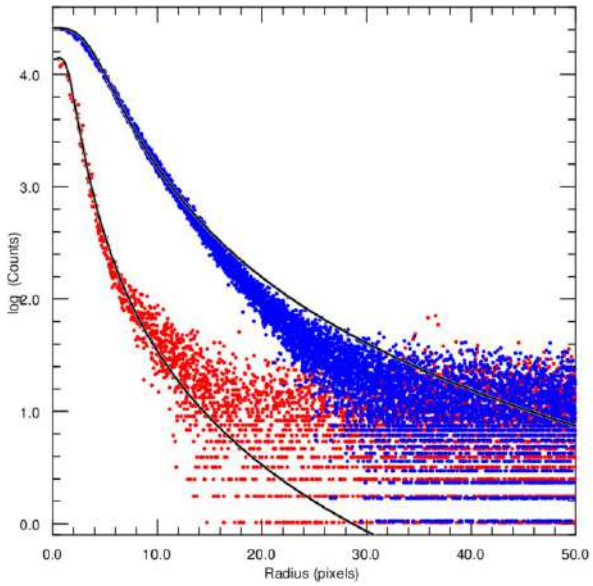

Figure 1.4: Agreement between experimental data and the radial fit from Eq. 1.5. [4]

To simulate the experimental data, the fit from Eq. 1.5 must be completed with photon noise resulting from different sources (dark noise, read noise, shot noise, background noise). This photon noise can be approximated by a Gaussian distribution. This distribution is centred on a mean of 5 photons with a standard deviation of 10 photons[7]. The noise is added to the simulation to represent more truly real data from starlight measurements.

For example, let us take a radial intensity profile of an image with a I_0 intensity star at the centre and two nearby stars (A and B) of intensity $0.01\, I_0$ at different locations. The intensity profiles are given in Fig. 1.5.

[6] In this case the value $\kappa = 1$ is chosen.

[7] Other distributions such as a Poisson can also be used, as long as the result is faithful with relevant noise counting behaviour. The intensity profile of the star is not deeply impacted by this choice here.

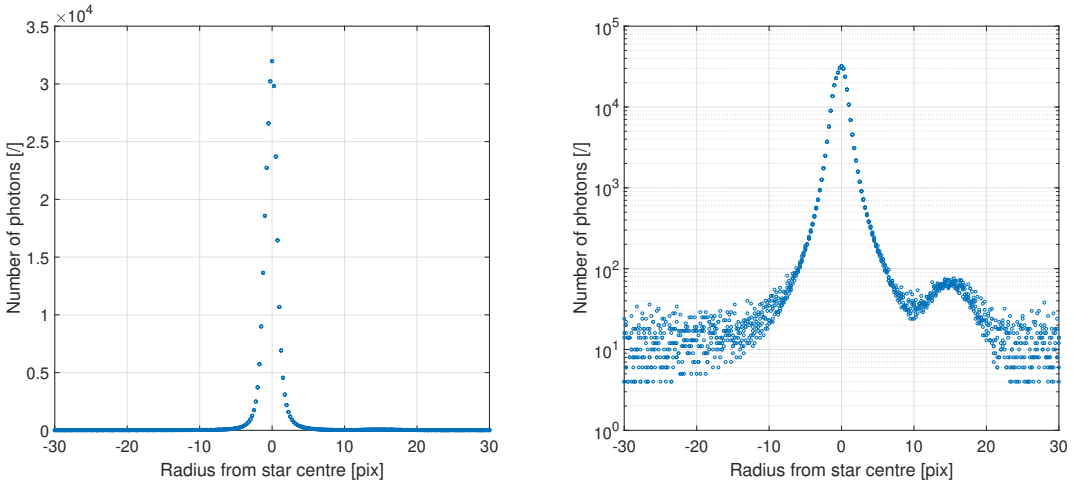

(a) Linear scale.

(b) Logarithmic scale.

Figure 1.5: Simulation of the radial intensity profile of a star assumed on the centre of the image.

The two nearby stars are invisible in the linear scale (Fig. 1.5a), but a bump in intensity is detectable once plotted in a logarithmic scale (Fig. 1.5b). This allows to estimate one of the nearby stars (let us define it star A) at around $r_A = 15$ pix. Nonetheless, the second star B is impossible to find, even if it has the same intensity as the first one.

Fig. 1.6 compares the intensity profiles of the central star alone (blue circles) and together with the star B (orange dots) in a logarithmic scale. When zoomed in (Fig. 1.6b), the intensity discrepancy is finally distinguishable. On the left side of the peak, the points are perfectly aligned. However, on the right side, the orange dots are slightly above the blue circles. This is the photon signal of the star B. Because of its position in a high star signal region, its flux gets completely outnumbered.

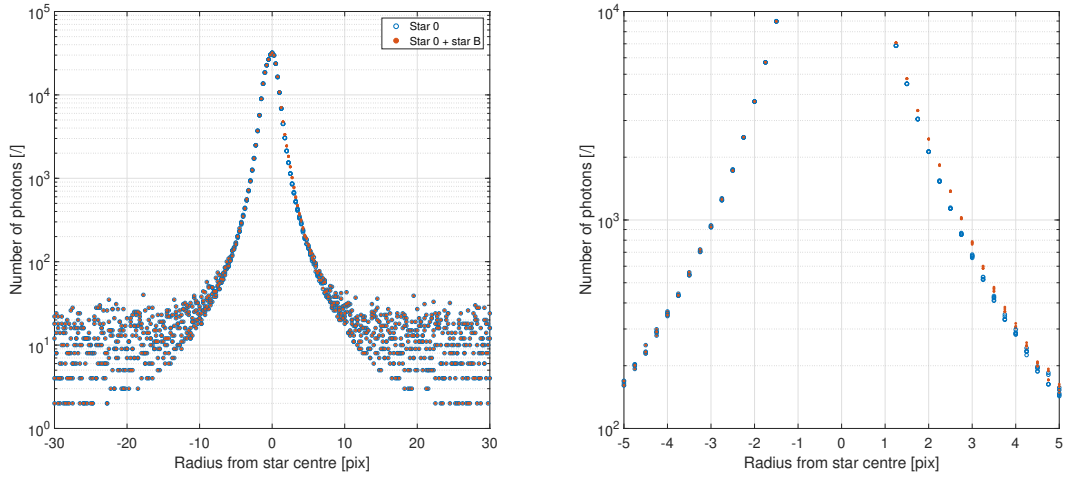

(a) Full intensity profile.

(b) Focus on $r \in [-5; 5]$ pix.

Figure 1.6: Intensity profiles of star 0 alone and stars 0 and B together.

This discussion relies on several assumptions but presents properly and simply the problem of the faint signal of an exoplanet orbiting its host star. Furthermore, we selected here a body with a signal intensity of $0.01\ I_0$, which is far above the usual intensity ratios found in real star-planet systems as explained earlier.

1.2 Detection

The first exoplanet, discovered in 1995, shows a mass close to Jupiter's and orbits around a solar-type star. [5] Since then, more than ten thousands have been detected. Around $4\,300$ are confirmed and the rest are waiting upon confirmation. [6] A statistical estimation based on NASA's Kepler space telescope data concluded that many exoplanets exist, a lot more than we thought. [7, 8, 9] The major part of the detected exoplanets come from two methods: radial velocity ($20\,\%$) and transit ($75\,\%$). [6] When combined, they can measure parameters such as mass, radius, density, orbit elements or even to infer the chemical composition of atmosphere. However, they are particularly used for planets close to their parent star. Other methods exist such as direct imaging or gravitational microlensing. Most of those methods rely on dynamical and photometric effects on the host star state caused by the exoplanet.

1.2.1 Transit method

The idea behind the transit method has been found by Struve in 1952. [10] Exoplanets show an orbital plane around their host star with random inclinations. When the orbital plane orientation matches roughly the line of sight between the Earth and the host star, the stellar flux will exhibit periodic temporary drops because of the exoplanet orbiting in front. Those drops even if undetectable at the time of publication because of their small amplitude, have later been measured, witnessing the presence of an exoplanet around the measured star. Fig. 1.7 represents such system. The upper image represents an exoplanet transiting in front of its host star and the lower one shows the corresponding evolution of the measured star brightness.

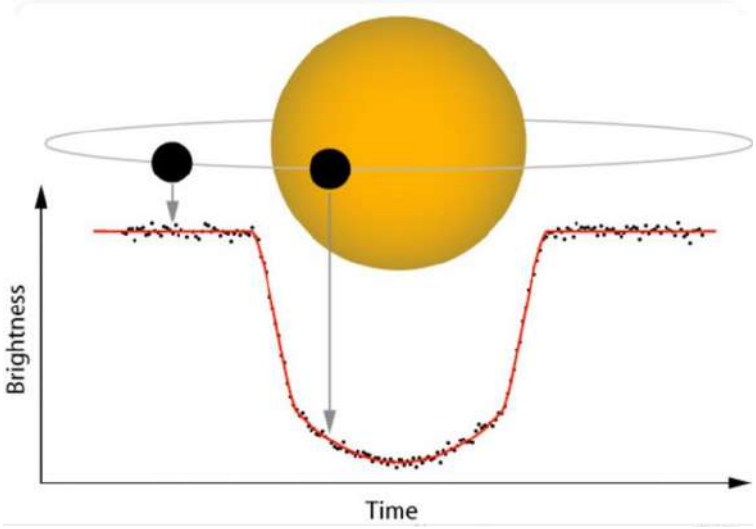

Figure 1.7: Representation of the exoplanet eclipsing orbit (up) and measurement of the host star brightness during the transit (down). [11]

1.2.1.1 Probability of transit

As explained above, a transit will occur for an Earth-based observer if and only if the planet shadow crosses out the line of sight between the Earth and the host star. Due to the spatial extension of the bodies in presence, we can define a full transit (dark blue) and grazing transit (light blue) (see Fig. 1.8. Any observer outside of the blue regions will not measure any drop in stellar flux and will not be able to detect this planet through the transit method.

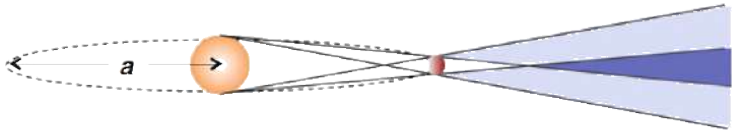

Figure 1.8: Celestial sphere regions for which full and grazing transits are observable. [12]

The probability of orbital parameters leading to a potential transit can be geometrically determined. This probability is given by the ratio of the celestial sphere swept out by the shadow. The transit of a planet with radius R_p orbiting a star with radius R_* will occur only if the following inequality is satisfied, where i is the inclination of the orbit and a its semi-major axis:

$$R_* + R_p > a\cos i > R_* - R_p. \tag{1.6}$$

The inequality restricts to $a\cos i > R_* - R_p$ for a full transit. Taking into account the random orientation of the orbit, the probability is given by: [12]

$$\mathbb{P}\left(\cos i < \frac{R_* + R_p}{a}\right) = \frac{R_* + R_p}{a}. \tag{1.7}$$

Typically R_p can be neglected compared to R_* giving directly:

$$\mathbb{P}\left(\cos i < \frac{R_*}{a}\right) \approx .0046 \left(\frac{R_*}{R_\odot}\right)\left(\frac{1\,\text{AU}}{a}\right). \tag{1.8}$$

Introducing the Sun radius ($R_\odot$) and the typical Earth-Sun distance (1 AU) the transit of the Earth in front of the Sun is observable in 0.46% of the celestial sphere. The probability favours the detection of planets in close orbits around large host stars.

1.2.2 Radial velocity method

This method provided the foundations of the exoplanet research field. It is responsible for the first exoplanet discovered in 1995[8]. [5] This method also provides a mean to assess the mass of the planetary companion, which is needed to determine its density and its nature (gas, rocky, icy).

The principle is straightforward: it consists of measuring the radial velocity (the velocity vector projected on the line of sight between the star and the Earth) through the Doppler shift of the starlight. According to the star-planet system, the star will oscillate around the center of mass, and consequently show a spectral shift as measured from the Earth.

Again, Struve in 1952 already proposed this method. [10] But the first discovery had to wait 40 years because of two major problems: the magnitude of the Doppler shift and the measurement precision. The Doppler shift can be estimated through Kepler's law rewritten in the Newton's form:

$$T^2 = \frac{4\pi^2\, a^3}{G(M_* + M_p)}, \tag{1.9}$$

where T is the orbital period, G the gravitational acceleration constant, a the semi-major axis and the masses of the star (M_*) and the planet (M_p) respectively. Assuming $M_* >> M_p$ and a circular orbit (which is a typical approximation, valid for most), we can determine the radial velocity from Eq. 1.9:

$$v_r[\text{m/s}] = 28.4 \left(\frac{1\,\text{yr}}{T}\right)^{1/3} \left(\frac{M_\odot}{M_*}\right)^{2/3} \left(\frac{M_p\,\sin i}{M_{\text{Jup}}}\right), \tag{1.10}$$

where v_r is the radial velocity to be measured and M_{Jup} is the mass of Jupiter. It can also be rewritten through the third Kepler law according to the semi-major axis of the planetary orbit as:

$$v_r[\text{m/s}] = 28.4 \left(\frac{\text{AU}}{a}\right)^{1/2} \left(\frac{M_\odot}{M_*}\right)^{2/3} \left(\frac{M_p\,\sin i}{M_{\text{Jup}}}\right). \tag{1.11}$$

[8] 51 Peg b is a hot planet very close to its star, with a size of about half of Jupiter.

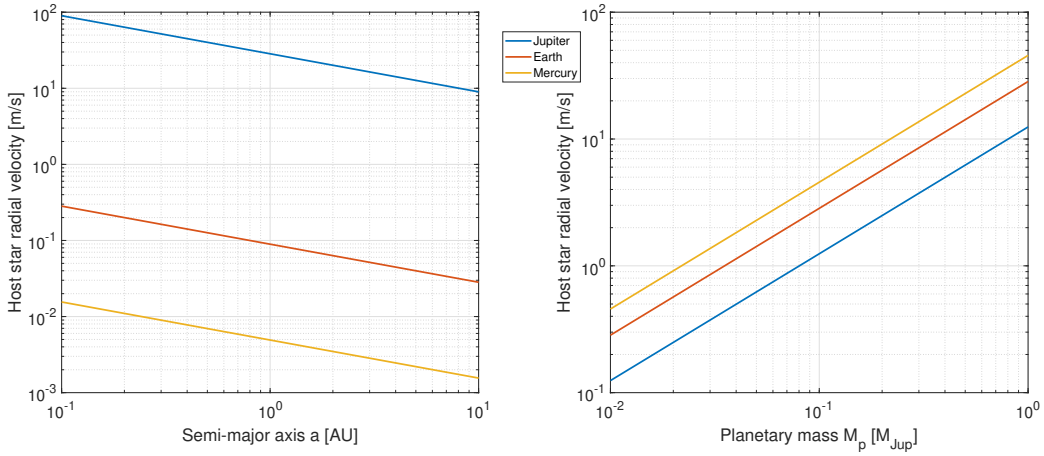

Figure 1.9: Radial velocity evolution of a $M_* = M_\odot$ host star for (left) planets of different masses according to their semi-major axis a and (right) planets at different semi-major axis according to their mass M_p. Perfect alignment of the orbital axis is assumed $i = 90°$.

Fig. 1.9 describes the evolution of the amplitude of the radial velocity variations of the barycentre of the system. On the one hand, the left graph shows relevant magnitudes such as Jupiter inducing an oscillation of around 12 m/s and the Earth causing a 10 cm/s variation, increasing to 1 m/s if we put it at a distance of 0.05 AU (5% of the average distance !). The right graph, on the other hand, tells that a Jupiter-sized planet on the orbit of Mercury would result in a 45 m/s oscillation of the star.

Therefore, a precision of the order of 10 m/s is needed to detect a Jupiter analogue around a Sun-like star. Such measurement was not possible until recently when the technology reached high quantum efficiency detectors and large resolution spectrographs. [12] Amongst the last spectrographs is the Echelle SPectrograph for Rocky Exoplanet and Stable Spectroscopic Observations (ESPRESSO) with a $R = 140\,000$ performance. Its objective is to reach a radial sensitivity of the order of the cm/s. Thus far, only the red detector showed a precision around 10 cm/s while the blue one only achieved 60 cm/s. [13]

1.2.3 Gravitational microlensing

This method allows to probe planets which are further away, orbiting at an intermediate distance from the parent star. It allows finding very distant planets (even in other galaxies) or isolated planets. Unfortunately, the events this method relies on are scarce and non-repeatable. Thus, it is very complicated to refine the planetary measurements further.

This method is based on the equations of gravitation developed under the scope of general relativity in the early XXth century. Such equations imply that light travels through space-time which is distorted by the gravity exerted by a body[9]. When the gravitational field reaches a high magnitude (black hole, star or even galaxies), the space-time distortion induces a deviation of the

[9]This gravity depends directly on the body's density.

light rays. Therefore, gravity is able to warp and bend light.

Einstein assumed that the transverse acceleration is given by:

$$a_{\perp} = \frac{GM\cos^3(\phi)}{b^2}, \tag{1.12}$$

with M the body mass, G the gravitational constant, b the impact parameter. [12] The impact parameter corresponds to the perpendicular distance between the trajectory of a moving object in a potential field and the object generating this very field. The instantaneous distance between the light ray and the body generating the magnetic field is given by $b\sec(\phi)$.

Fig. 1.10a shows the geometry of the system. The angle of deflection α is given by:

$$\alpha = \frac{\Delta v_{\perp}}{c} = \frac{1}{c}\int_{-\infty}^{+\infty} a_{\perp}(t)\,dt = \frac{2GM}{b^2c} \longrightarrow \frac{4GM}{b^2c}, \tag{1.13}$$

where the impulse approximation implying that $t = b\,\tan(\phi)/c$ and the Einstein's General Relativity correction give the final result. [12]

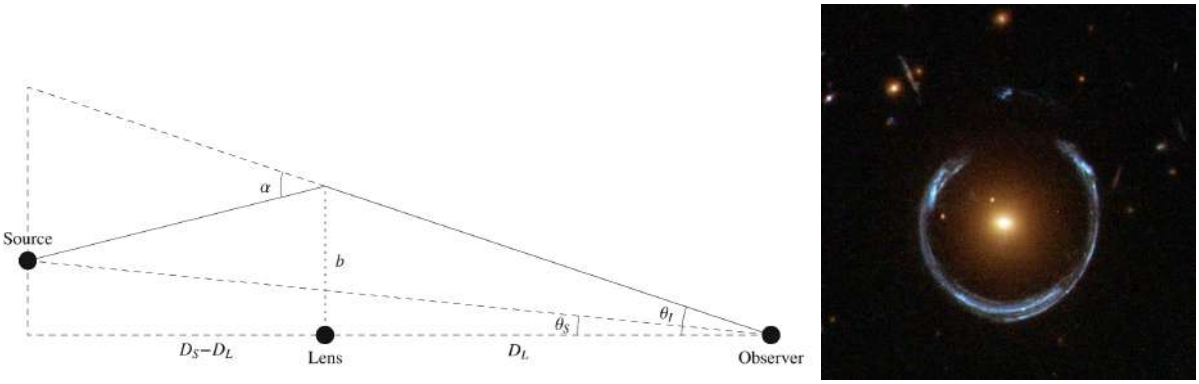

(a) Gravitational lensing geometry. [12]

(b) Example of Einstein ring. [14]

Figure 1.10: Gravitational lensing schematic geometry and example.

Due to the gravitational lensing, the image of the source emitting the detected light is seen at an angle θ_I different from θ_S, the actual angle[10]. For a colinear source and lens, the image is considered a ring whose diameter is called Einstein's diameter. A picture of a Luminous Red Galaxy (called LRG $3-757$) exerting enough gravity to distort the light emitted by a much more distant blue galaxy taken by the Hubble Space Telescope is given in Fig. 1.10b.

The consequence is, for example, the magnification of a background star due to the bending effect of its light by a foreground star. If this latter star is orbited by an exoplanet, the spike in intensity due to the host star will be followed by a fainter, smaller spike due to the exoplanet. The analysis of the spike makes it possible to gain information about the exoplanet. Such measurement is shown in Fig. 1.11.

[10]The angle magnitudes for real cases in astronomy are of the order of the milliarcsecond.

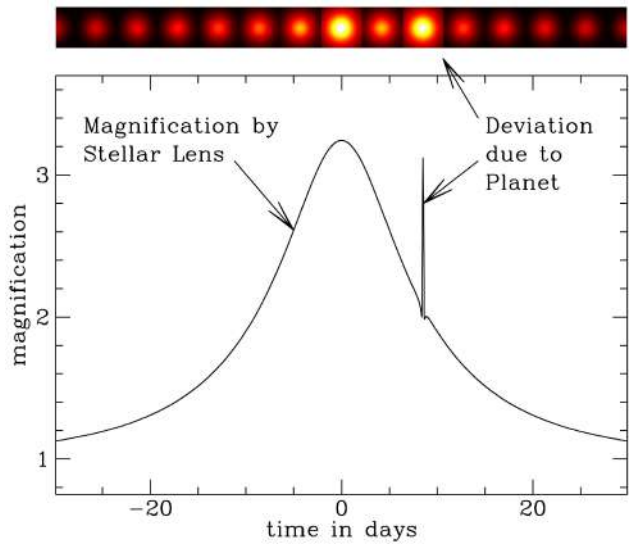

Figure 1.11: Evolution of the stellar magnification. The presence of a second spike hints the presence of an exoplanet. [15]

1.2.4 Direct imaging

This technique is pretty much the most advanced, challenging but rewarding. The objective is to observe the planet outshining over the parent star. Because of the radiance ratio, conventional imaging techniques are not adequate. To produce direct images, the system must suppress the starlight and diffraction pattern as well as scattering imperfections from the telescope. It requires complex and refined adaptive optics and coronographic techniques but allows for some cases to follow orbits and study spectra. Due to the parent star radiance and imaging challenges, it is easier for further bigger and hotter exoplanets, as one can see in Fig. 1.12. However, the hurdles imposed by astrophysics (star - companion contrast), physics (diffraction), and engineering (scattering) made this method rise later than the previous ones.

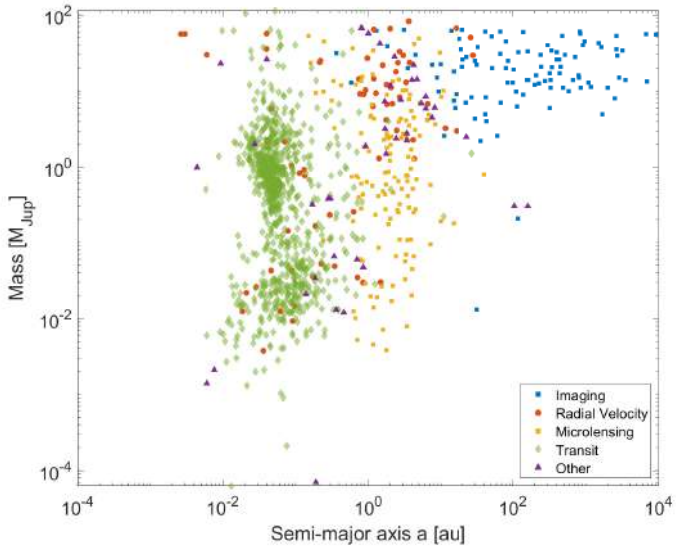

Figure 1.12: Exoplanets discovered according to mass and semi-major axis. Only the planets for which a semi-major axis and mass are given have been plotted, consequently the proportion of detected planets for each method is not faithful. Data from [16]

The advantage of the direct imaging method is the possibility to gather information directly from the planet radiation or reflection, without having to wait for transit. Because of the low flux, the resolution is quite low but many molecular bands can still be detected, and the study of their spectral and temporal behaviour allows to learn the structure and composition of the atmosphere as well as the surface properties and rotation rate.

To reach the high angular resolution needed to achieve direct imaging, one can rely on single pupil telescopes with a very large collecting aperture working close to the diffraction limit or on multiple pupils interferometric systems. The latter one is able to reach better angular resolution, of the order of the milliarsecond.

Chapter 2

Nulling interferometry

2.1 The concept

This chapter provides an overview of the nulling interferometry technology.

As explained in the previous chapter about exoplanet detection, the major difficulties arise from the high angular resolution needed and the luminosity contrast. These constraints make the direct imagery impossible, and the indirect methods show limited performance. In this context, Bracewell proposed in 1978 a solution using a spinning infrared interferometer. [17] The main idea is to design an interferometer such that the bright object (the host star) lies on an interferometric null. This null of the stellar flux results in a relaxed luminosity contrast, allowing the detection and measurement of faint objects (as an exoplanet for example).

2.1.1 The interferometric process

At the heart of this technique is the overlapping of two beams. When the phase of one of the beams is tuned, the transmission map yields a typical interferometric pattern of sinusoidal intensity fringes. This is explained by the wave behaviour of light, which generates an interference term depending on the relative phase between both beams.

The angular periodicity of those fringes corresponds to the parameters of the interferometer and is given by λ/b where λ is the wavelength and b the baseline. Tuning those design parameters allows placing a bright fringe on the hypothetical locus of the exoplanet. However, another problem arises: the exoplanet flux can be mixed with the background flux.

2.1.1.1 Exoplanet flux modulation

The background flux can be composed of stars or galaxies in the line of sight, or the exozodiacal flux[1]. Modulation of the exoplanet signal allows to distinguish it as the background flux can be assumed spatially uniform.

[1]The exozodiacal disk is a region of space around the host star filled with dust and rocks. Their thermal radiation emission generates a diffuse background flux that can interfere with the exoplanet flux.

The modulation can be achieved in two ways.

The first one, proposed by Bracewell, consists of rotating the interferometer perpendicularly to the line of sight[2]. The transmission map, therefore, rotates similarly, and bright and dark fringes cross the exoplanet location on the map. [17] This idea is complex to implement and very costly as the whole formation (or spacecraft) has to be rotated while keeping precise relative positioning. A typical Bracewell setup is represented in Fig. 2.1a, and its typical transmission map along the star and three exoplanets is shown in Fig. 2.1b.

The second one is an alternative proposed in 1999 by Mariotti. [18] The transmission map rotation is introduced by a time-variable phase shift between the nulled outputs of two interferometric subarrays. The phase shift modifies the shape and position of resulting bright fringes without changing the dark fringe profile. This approach allows to modulate the signal without physical rotation of the instrument, and the modulation comes from an internal mechanism inducing the time-variable phase shift.[3]

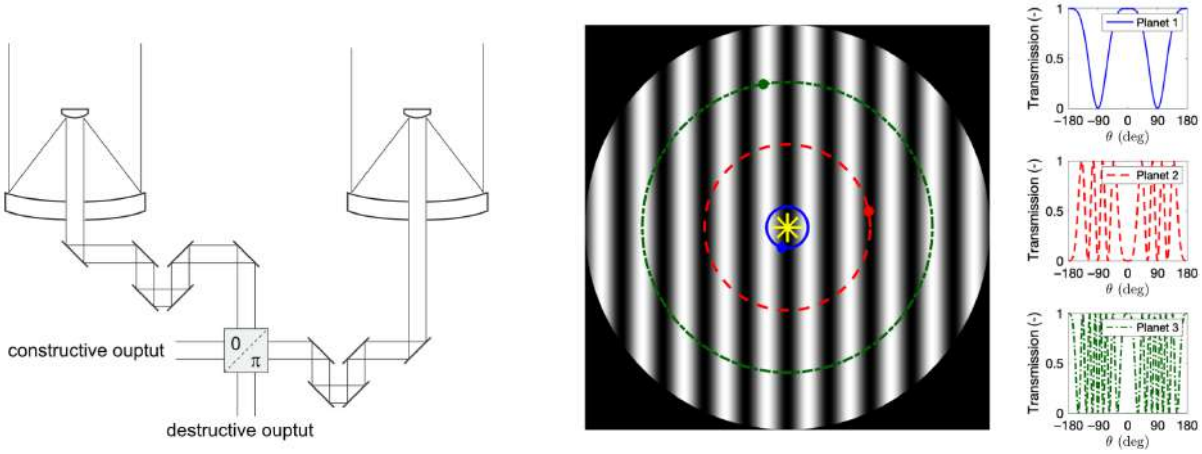

(a) Schematic configuration of a Bracewell interferometer. [19]

(b) Monochromatic transmission map with three hypothetical exoplanets and their corresponding modulated signals. [1]

Figure 2.1: Bracewell interferometer setup representation and transmission map.

An interferometer based on the recombination of two beams has been called a Bracewell interferometer, but other setups rely on more than two telescopes (see Sec. 2.1.2).

The advantage of space-based interferometry lies within the suppression of atmospheric distortion. Moreover, the baseline[4] can be extended almost infinitely, thanks to formation flying spacecraft and laser monitoring of their relative distances. In the case of an interferometer, the angular resolution achieved corresponds to a theoretical telescope whose diameter would be the baseline. In this frame, several missions have been developed. They will be presented in further sections.

[2]The line of sight links the host star (centred on the detection plane to experience a null) to the interferometer.
[3]This internal modulation can also be referred to as phase chopping.
[4]The baseline is the distance between separated telescopes.

2.1.2 Stellar leakage

The interference of the combined beams from both apertures produces a transmission map projected on the observed portion of the sky. As developed earlier, a destructive interference is centred on the star to cancel out its flux. However, the star has a finite diameter, leading to a portion of its flux not being fully cancelled. This effect is called stellar leakage. It is proportional to the interferometer configuration.

As derived in [20] by Dr. L. Escarrat, the complex amplitude resulting from the superposition of the wavefronts from each telescope can be written:

$$\Psi(\theta,\phi) \propto \sum_k D_k e^{i\Theta_k} e^{i\phi_k} = \sum_k D_k e^{i\frac{2\pi}{\lambda} L_k \theta \cos(\delta_k - \phi)} e^{i\phi_k}. \tag{2.1}$$

The telescope k has a diameter D_k and is located in the collecting plane by the vector $\boldsymbol{L}$ of polar coordinates (L_k, δ_k). The angles (θ, ϕ) locate the source considered relatively to the sight axis[5]. Θ_k is the phase of the field collected by the telescope k. Finally, ϕ_k is the phase introduced during the interferometric process in the arm k. The system is represented for the k^{th} aperture along with angular coordinate in Fig. 2.2.

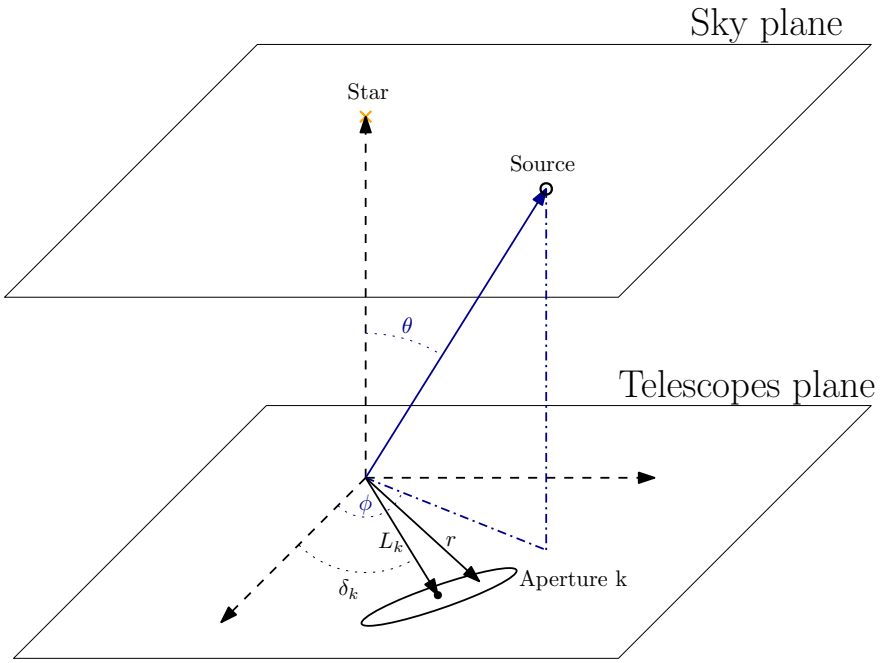

Figure 2.2: Representation of the aperture k coordinates in the telescope plane of the system. Angular coordinates of the source are also represented. Inspired from [20]

As θ (the solid angle between the source and the star) is by definition small, the equation can be developed around 0:

[5]Corresponding to the principle of operation of the interferometer, the source is the exoplanet and the sight axis links the star to the spacecraft.

$$\Psi(\theta,\phi)\propto\sum_k D_k e^{i\phi_k}\left\{1+i\frac{2\pi}{\lambda}L_k\theta\cos(\delta_k-\phi)-\frac{4\pi^2}{\lambda^2}L_k^2\theta^2\cos^2(\delta_k-\phi)+O(\theta^3)\right\}. \tag{2.2}$$

The rejection ratio, given by the transmission map performance on the star and exoplanet fluxes, is directly linked to the cancelling of the successive terms of Eq. 2.2. The cancelling of the first term of this equation induces that any source at the centre of the field ($\theta = 0, \phi = 0$) is extinct:

$$\sum_k D_k e^{i\phi_k} = 0. \tag{2.3}$$

Considering two apertures, the result is:

$$D_1 e^{i\phi_1} + D_2 e^{i\phi_2} = 0. \tag{2.4}$$

If we take telescopes of equal aperture area and induce a phase shift $\phi_1 = 0$ in the first arm and $\phi_2 = \pi$ in the second arm, the term cancels out. This configuration corresponds to a classical Bracewell interferometer.

The following terms of Eq. 2.2 describe the theoretical profile of the central black fringe[6]. As more terms are cancelled out by the configuration, the extinction follows a behaviour in a higher order of θ. The extinction profile for various orders is plotted in Fig. 2.3. A higher-order dependency induces a more flattened extinction profile, therefore the stellar leakage is decreased as the extinction region covers more of the finite size of the star.

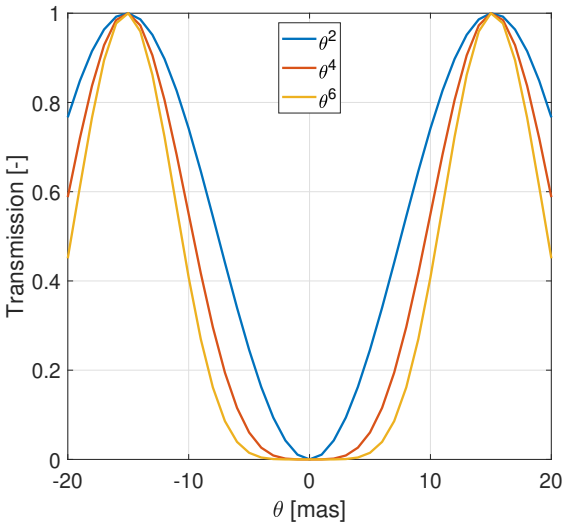

Figure 2.3: Schematic representation of the profile of the intensity map of several interferometer configurations. The first non-cancelled term of Eq. 2.2 dictates the profile of the transmission map according to the order of θ.

[6]Only this fringe is described by the other terms as this equation results from a development for $\theta \approx 0$.

Cancelling out further terms in Eq. 2.2 is only achievable by considering more than two apertures. Several designs have been implemented with various numbers of telescopes.

2.2 Interferometers - Ground-based

This section presents a few of the ground-based interferometers. This list is non-exhaustive, and other ground-based interferometers exist. Nonetheless, they do not observe exoplanets and serve different purposes (synthetic aperture radar, gravitational waves, etc).

2.2.1 Very Large Telescope

The VLT is a ground based complex of eight telescopes of the ESA. It is composed of four fixed units with mirrors of 8.2 meters of diameter (main units) and four movable telescopes of 1.8 meters diameter (auxiliary units). The light beams are combined through mirrors and tunnels to form the Very Large Telescope Interferometer (VLTI) able to reach an angular resolution of the order of the milliarcsecond. However, the four main units are used for interferometry only a few nights per year. Most of the interferometric images processed come from the four auxiliary units, which, thanks to their mobility along different axes, allows to tune finely the baseline and recombine up to four apertures. They are situated at Cerro Paranal in Chile at an altitude of $2\,635$ meters. Figure 2.4 shows the complex. The telescopes are Ritchey-Chrétien telescopes designed for optical and infrared observation.

Figure 2.4: Aerial view of the VLT. The four large buildings are the enclosures of the main telescopes. Three auxiliary telescopes can be observed in the foreground. [21]

Amongst its scientific firsts, one can highlight the first extrasolar planet image or the observation of the afterglow of the furthest known Gamma-Ray Burst. [22]

2.2.2 Navy Precision Optical Interferometer

The Navy Precision Optical Interferometer (NPOI) is an American astronomical interferometer located in Arizona at an altitude of $2\,163$ meters. It is a three-arm Y configuration with a length of 250 meters each. On each arm, stations can be moved to discrete positions. The interferometer is able to provide astrometric data (position measurements) and imaging with up to six telescopes. Four optical infrared telescopes of 1.8 meters aperture have been incorporated in 2009. Vacuum pipes conduct light towards the beam combining facility. Figure 2.5 shows an aerial view of the Y shaped interferometer.

Figure 2.5: Aerial view of the Navy Precision Optical Interferometer. [23]

2.3 Space-based interferometer projects

2.3.1 Terrestrial Planet Finder

This project has been approved in 2004 by the NASA. Planned for the horizon 2015-2020, it has been postponed multiple times and eventually cancelled in 2011. The objective was to find exoplanets by blocking the light of the host star. Two telescope systems were considered: TPF with several small telescopes and TPF-C with one large telescope. The Terrestrial Planet Finder Interferometer (TPF-I) would have relied on the interferometric process as presented earlier, considering formation flying spacecraft. The Terrestrial Planet Finder Coronograph (TPF-C) would implement a coronographic mode, where the starlight is physically blocked.

2.3.2 Darwin

Darwin is the equivalent of the TPF-I on the European side. The most recent design consisted of three telescopes between three and four meters in diameter in formation flying. The collected light would be redirected towards a fourth spacecraft containing the beam combiner,

the spectrometer, and the cameras. This central spacecraft would have been the communication centre of the whole setup. The project was abandoned around 2007.

(a) Square configuration with remote communication and light path.

(b) Linear configuration with physical link between telescopes.

Figure 2.6: Artist views of space-based interferometer configurations envisaged for TPF-I and Darwin projects.

Years later, another project, the Fourier-Kelvin Stellar Interferometer (FKSI), was proposed. It would have consisted of a simplified version of the TPF-I and would have been able to characterise the atmospheres of a large sample of planets. However, it was abandoned as well.

The ESA very recently showed interest back in space-interferometric mission with the advent of the project Large Interferometer For Exoplanet (LIFE). This project, if completed, would finally result in a satellite implementing nulling interferometry to detect and characterise exoplanets.

2.3.3 Large Interferometer For Exoplanet

LIFE was initiated in 2017 with the goal to develop technology and science for a later ambitious space mission. It can be considered as the rebirth of space-based interferometer projects abandoned around 2010 such as Darwin, TPF-I or FKSI. The main objective of LIFE is to detect exoplanets and scrutinise their atmosphere. The mission currently stands in a first study phase. The official website of the space mission reads that the current main activities are:

- Formulating the first set of clear science objectives and science cases for the mission;
- Deriving athefirst set of major science requirements based on the science objectives;
- Assessing the current status and maturity of key technologies required for the mission;
- Drafting a technology development roadmap;
- Seeking funding opportunities for technical as well as scientific work related to LIFE;
- Community building by generating interest in scientific and technological development and expanding the team of collaborators.

Chapter 3

Achromatic Phase Shifter concepts review

As explained in the previous chapter, the nulling interferometry requires a π phase shift achieved by the phase shifter, and the performance of the process is directly linked to its achromaticity.

First, the requirements on the phase shift will be defined, concerning either its achromaticity or accuracy. Then, the different ways able to generate such phase shift are described. To do so, a state of the art of the existing APS concepts will be presented. The concepts may be split between intrinsic and compensated achromatism. The first case relies on the reflection achromatic property and corresponds to light encountering mainly mirrors. The latter case deals with material propagation, yielding an inevitable chromatic behaviour but where the element is designed such that different chromatisms compensate each other to reach the final achromaticity. First of all, the phase shift requirements will be exposed to be able to define figures of merit. The trade-off will select the most promising candidates chosen for further investigation.

Most of this chapter is a concise summary of the work done by scientists and engineers during missions in the scope of ESA projects such as the Darwin project or during PhD thesis.

3.1 Phase shifting requirements

Achromatic phase shift has already been achieved, but one must be careful to watch for the specifications of the phase shifter. In fact, when one talks about achromatic phase shift, it is paramount to verify the specified spectral band. In this case, the objective is to determine an achromatic phase shifter with the best performance across a spectral band of approximately $5\ \mu$m and depending on the platform size of the mission considered.

The figure of merit of the nulling is given by the rejection ratio. Its minimum is given by the average star-planet radiance ratio and it must show good stability. Imperfections in the system[1] result in a worsening of the rejection ratio. Therefore, when one considers the APS alone, its rejection ratio must be high enough to cope with such unrelated errors. The main numerical

[1] Amongst others can be noted Optical Path Difference (OPD) and stability, telescope pointing errors, photometric unbalance and polarisation alignment

figure of evaluation is then the rejection ratio across the whole spectral band, but other criteria must be taken into account such as compactness, robustness, sensitivity, technical feasibility, etc.

Strictly speaking, an element is defined as achromatic when its operation is independent of the wavelength. Therefore, a modification of the incident wavelength will not produce any change in the result. An achromatic element is actually defined as near insensitive to wavelength modification within a peculiar bandwidth. The "near insensitive" part needs to be specified and implies specifying a certain tolerance on the specified band under which the variation does not impact the targeted performance.

The electromagnetic wave generated by an interferometer can be written in the most general way as a sum of the incident waves. For the simplest case of the recombination of two waves, we obtain with $N = 2$:

$$S = A\, e^{i\phi} = \sum_{k=1}^{N} A_k\, e^{i\phi_k} = A_1\, e^{i\phi_1} + A_2\, e^{i\phi_2}, \tag{3.1}$$

where S is the output wave, A the amplitude and ϕ the phase. The simplest case being the recombination of two apertures, the resulting field is given by the sum of the two incoming waves. The intensity I of this wave is given by definition by $|S| = S.S^*$:

$$I = |A_1|^2 + |A_2|^2 + 2\,|A_1|\,|A_2|\,\cos\left(\phi_2 - \phi_1\right). \tag{3.2}$$

We can rewrite it with the intensities of each field I_1, I_2 and their phase difference $\Delta\phi = \phi_2 - \phi_1$ as:

$$I = I_1 + I_2 + 2\sqrt{I_1\, I_2}\,\cos\left(\Delta\phi\right). \tag{3.3}$$

In perfect operation, both intensities are equal $I_1 = I_2$. The intensity in bright fringes (corresponding to $\Delta\phi = 0$) will be $4\, I_0$ while in dark fringes ($\Delta\phi = \pi$) the intensity will be null. This leads to a theoretically infinite rejection ratio $\rho = I_{max}/I_{min}$. But this perfect case does not occur as the field intensities do never perfectly match $I_1 \approx I_2$ nor does the phase shift $\Delta\phi \approx \pi$.

The imperfections of the system in terms of phase (ε_ϕ) and amplitude (ε_I) can be defined according to the goal phase shift $\Delta\phi_0$ as:

$$\begin{aligned} \varepsilon_I &:= \frac{I_2}{I_1} - 1 \quad &\Longleftrightarrow I_2 = I_1\left(1 + \varepsilon_I\right) \qquad &\text{and} \\ \varepsilon_\phi &:= \Delta\phi - \Delta\phi_0 \quad &\Longleftrightarrow \Delta\phi = \Delta\phi_0 + \varepsilon_\phi. \end{aligned} \tag{3.4}$$

The total intensity after recombination (from Eq. 3.3) can be rewritten:

$$I = I_1\left(2 + \varepsilon_I\right) + 2\, I_1\sqrt{1 + \varepsilon_I}\,\cos\left(\Delta\phi_0 + \varepsilon_\phi\right). \tag{3.5}$$

The intensities of bright and dark fringes are therefore given by:

$$\begin{aligned} &\text{Bright fringe:} \quad \Delta\phi_0 = 0 \quad I_{max} = I_1\,(2+\varepsilon_I) + 2\,I_1\,\sqrt{1+\varepsilon_I}\,\cos\left(\varepsilon_\phi\right), \\ &\text{Dark fringe:} \quad \Delta\phi_0 = \pi \quad I_{min} = I_1\,(2+\varepsilon_I) - 2\,I_1\,\sqrt{1+\varepsilon_I}\,\cos\left(\varepsilon_\phi\right). \end{aligned} \tag{3.6}$$

The rejection now reads:

$$\boxed{\rho = \frac{I_{max}}{I_{min}} = \frac{2+\varepsilon_I + 2\,\sqrt{1+\varepsilon_I}\,\cos\left(\varepsilon_\phi\right)}{2+\varepsilon_I - 2\,\sqrt{1+\varepsilon_I}\,\cos\left(\varepsilon_\phi\right)}}. \tag{3.7}$$

It is impacted by both types of errors (amplitude and phase) in the system. The maximum tolerance in terms of these errors has to be determined to compare and reject different concepts.

3.1.1 Amplitude mismatch requirement

The maximum acceptable amplitude mismatch ε_I is defined by setting the phase defect $\varepsilon_\phi = 0$. This tolerance comes from evaluating the impact of the error on the rejection ratio. If the waves are perfectly in phase ($\varepsilon_\phi = 0$), the rejection ratio reads:

$$\rho = \frac{I_{max}}{I_{min}} = \frac{2+\varepsilon_I + 2\,\sqrt{1+\varepsilon_I}}{2+\varepsilon_I - 2\,\sqrt{1+\varepsilon_I}}. \tag{3.8}$$

As we are looking at the behaviour of the rejection ratio when the amplitude mismatch departs from perfect operation, we can assume that ε_I is small. This assumption allows to develop the square root in a Taylor expansion:

$$\sqrt{1+\varepsilon_I} = (1+\varepsilon_I)^{1/2} = 1 + \frac{1}{2}\varepsilon - \frac{1}{8}\varepsilon_I^2 + O(\varepsilon_I^4). \tag{3.9}$$

Replacing the square root by this expansion provides the following rejection ratio:

$$\begin{aligned} \rho &\approx \frac{2+\varepsilon_I + 2\,\left(1+\varepsilon_I/2 - \varepsilon_I^2/8\right)}{2+\varepsilon_I - 2\,\left(1+\varepsilon_I/2 - \varepsilon_I^2/8\right)}, \\ &\approx \frac{4+2\varepsilon_I - \varepsilon_I^2/4}{\varepsilon_I^2/4}, \\ \rho &= \frac{16}{\varepsilon_I^2} + O(\varepsilon_I^{-1}). \end{aligned} \tag{3.10}$$

Finally, the relation between rejection ratio and amplitude mismatch is:

$$\boxed{\rho \approx \frac{16}{\varepsilon_I^2} \leftrightarrow \varepsilon_I \approx \frac{4}{\sqrt{\rho}}}. \tag{3.11}$$

For a target rejection ratio of 10^4 as in this work, the amplitude mismatch must remain below:

$$\rho \geqslant 10^4 \longrightarrow \varepsilon_I \leqslant 4\,10^{-2}. \tag{3.12}$$

This limit requires a flux equivalence up to 4%.

The amplitude mismatch so far has been considered as the ratio of the intensities. This assumes that the polarisation vectors of both fields are perfectly aligned. The amplitude ratio at recombination depends on θ, the angle between the polarisation vectors:

$$\varepsilon_I \propto \cos^2(\theta). \tag{3.13}$$

The amplitude mismatch requirement in terms of polarisation misalignment becomes:

$$\varepsilon_I \geqslant 99.6\ \% \longrightarrow \theta \lesssim 8.95\,10^{-2}\ \text{rad} \approx 5.12\ \text{deg}. \tag{3.14}$$

3.1.2 Phase defect requirement

As for the amplitude mismatch, the phase defect tolerance is defined by considering intensities perfectly equal. With $\varepsilon_I = 0$ the rejection ratio becomes:

$$\rho = \frac{I_{max}}{I_{min}} = \frac{1 + \cos\left(\varepsilon_\phi\right)}{1 - \cos\left(\varepsilon_\phi\right)}. \tag{3.15}$$

Again, ε_ϕ tends towards zero. Under the small angle approximation, the cosine is replaced by its Taylor development:

$$\cos(\varepsilon_\phi) = 1 - \frac{1}{2}\varepsilon_\phi^2 + O(\varepsilon_\phi^4). \tag{3.16}$$

The rejection ratio becomes directly:

$$\rho \approx \frac{2 - \varepsilon_\phi^2/2}{\varepsilon_\phi^2/2} = \frac{4}{\varepsilon_\phi^2} + O(1), \tag{3.17}$$

and its relation with the phase defect is:

$$\boxed{\rho \approx \frac{4}{\varepsilon_\phi^2}} \leftrightarrow \varepsilon_\phi \approx \frac{2}{\sqrt{\rho}}. \tag{3.18}$$

The target rejection of 10^4 thus induces:

$$\rho \geqslant 10^4 \longrightarrow \varepsilon_\phi \leqslant 2\,10^{-2}\ \text{rad} \approx 1.15\ \text{deg}. \tag{3.19}$$

3.1.3 Extension to polychromatic light

Extending the previous requirements to polychromatic light is straightforward, as the results still hold by defining:

$$\varepsilon := \max_{\Delta\lambda}\left(\varepsilon(\lambda)\right) \qquad\qquad \beta := \min_{\Delta\lambda}\left(\beta(\lambda)\right). \tag{3.20}$$

As those restrictions can be very stringent when one considers the whole bandwidth, it is of common usage to split the spectral band according to its scientific interests. Those sub-bands will consequently have to follow different requirements according to the observing interest.

However, one may be interested in the determination of the rejection ratio according to the wavelength. In fact, it has been introduced earlier as one of the main figures of merit of an Achromatic Phase Shifter. For the interferometric case, the source of light is a star. As presented earlier, a star in its perfect state of operation is well described as a black body. The radiance of a black body is described by Planck's law given in Eq. 1.1. The law is rewritten for clarity:

$$B_\lambda(T) = \frac{2hc^2}{\lambda^2}\frac{1}{e^{hc/\lambda kT}-1}. \tag{3.21}$$

The interfering intensity obtained after recombination will be given by the sum of the monochromatic intensities described above multiplied by the black body radiance across the spectral band considered:

$$I = \int_{\lambda_{min}}^{\lambda_{max}} B_\lambda(T)\, I_\lambda\, d\lambda = \int_{\lambda_{min}}^{\lambda_{max}} B_\lambda(T)\left[I_1(2+\varepsilon_I) + 2\, I_1\sqrt{1+\varepsilon_I}\,\cos\left(\varepsilon_\lambda\right)\right] d\lambda. \tag{3.22}$$

The rejection ratio now becomes:

$$\rho = \frac{\displaystyle\int_{\lambda_{min}}^{\lambda_{max}} B_\lambda(T)\left[(2+\varepsilon_I) + 2\, I_1\sqrt{1+\varepsilon_I}\,\cos\left(\varepsilon_\lambda\right)\right] d\lambda}{\displaystyle\int_{\lambda_{min}}^{\lambda_{max}} B_\lambda(T)\left[(2+\varepsilon_I) - 2\, I_1\sqrt{1+\varepsilon_I}\,\cos\left(\varepsilon_\lambda\right)\right] d\lambda}. \tag{3.23}$$

A first assumption can be made concerning the numerator which represents the intensity of bright fringes. As a matter of fact, I_{max} can be considered close to $4\, I_1$ as amplitude and phase defects have a small impact in bright fringes. This allows rewriting the rejection ratio as:

$$\boxed{\rho = \frac{\displaystyle 4\int_{\lambda_{min}}^{\lambda_{max}} B_\lambda(T)\, d\lambda}{\displaystyle\int_{\lambda_{min}}^{\lambda_{max}} B_\lambda(T)\left[(2+\varepsilon_I) - 2\, I_1\sqrt{1+\varepsilon_I}\,\cos\left(\varepsilon_\phi\right)\right] d\lambda}}. \tag{3.24}$$

The main advantage of this formulation is that the numerator can be calculated once and for all. The behaviour of the phase defect according to the APS studied will be incorporated in the $\Delta\phi_\lambda$ term in the denominator and will yield the rejection ratio to be expected. [24]

3.2 Dispersive plates

The idea behind the concept of dispersive plates is a perfect example of compensated achromatism. It is inspired by techniques used by optical designers to minimise lenses chromatic aberrations. In a general way, the phase shift $\Delta\phi$ induced during propagation depends on the propagation length L and the medium refractive index n:

$$\Delta\phi(\lambda) = \frac{2\pi}{\lambda} nL. \tag{3.25}$$

Both depend on the medium in which the light propagates.

3.2.1 Principle

The objective is to propagate light through plates of materials with competing dispersion $\partial n/\partial\lambda$. The thickness and materials are optimised to reach a global linear wavelength dependence of the optical path L to compensate for the $1/\lambda$ behaviour of the phase shift. Fig. 3.1 shows a scheme of an APS working on the dispersive plate principle. In each arm, the light propagates through several plates made of a dielectric medium. Each plate has a precise design taking into account geometry, material, size, purity, etc. They are designed together with the OPD line such that the chromatism of the phase shift is compensated when recombining both beams. Moreover, they can be designed to compensate the remnant dispersion of the interferometer.

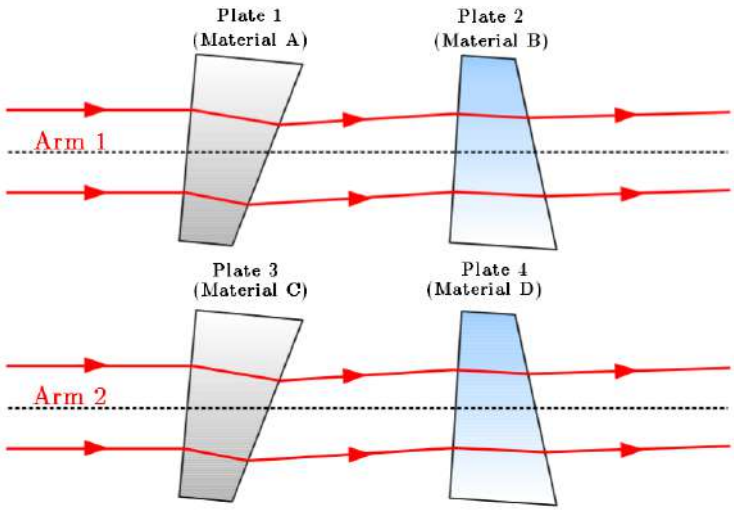

Figure 3.1: Schematic example of an APS made from dispersive plates in an interferometer. The beams propagate through different materials with different geometries, leading to a compensated chromatism between both arms. Extracted and modified from [24].

The system is arranged such that the interferometer stays as symmetrical as possible (number, order, wedge and incidence angle, spacing). The difference between both arms comes from the thickness of some plates. [25]

The optical path through the plate cascade is given by:

$$D(\lambda) = d_0 + \sum_k \left[\left(n_k(\lambda) - 1\right) d_k \right], \tag{3.26}$$

where d_0 is the geometrical path corresponding to propagation in air or in vacuum. The refractive index of air is directly assumed $n_{air} = n_{vac} = 1$. d_k and n_k are the thickness and refractive index of the k$^{\text{th}}$ plate. Through the design of these two parameters, one can obtain any phase shift value, making this concept versatile.

The phase shift defect is given by injecting the optical path (Eq. 3.26) in the phase shift (Eq. 3.25):

$$\varepsilon(\lambda) = \frac{2\pi}{\lambda} D(\lambda) - \pi = \frac{2\pi}{\lambda} \left(d_0 + \sum_k \left[\left(n_k(\lambda) - 1\right) d_k \right] \right) - \pi. \tag{3.27}$$

3.2.2 Implementation

The use of dispersive plates induces new constraints to take into account such as spurious reflections at the plates interfaces (front, end, and within each plate). The system is also sensitive to input parameters and beam stability. A modification of the input incidence angle, for example, can lead to different output angles and optical paths, generating a different output.

Wedged prisms are usually preferred over parallel plates. The reasons are twofold. First, the phase shift depends on the propagation length in the material. This length is given by the thickness of the prism which can be adjusted by mere translation parallel to the wedge angle. Second, the spurious reflections are overcome by the wedge angle deflecting the parasitic reflections out of the optical path (see Fig. 3.2).

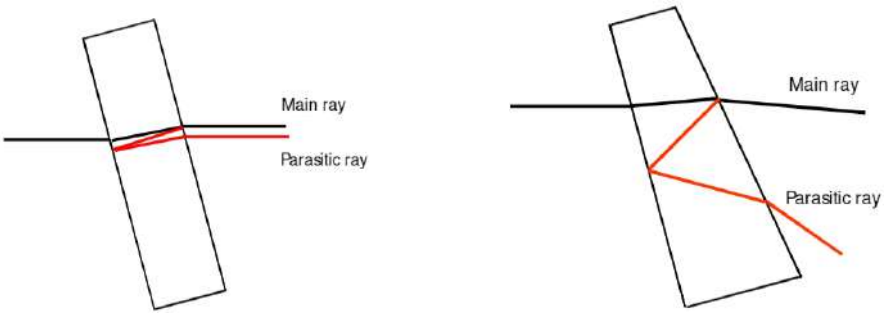

(a) Parallel plate. (b) Wedged plate.

Figure 3.2: Straylight rejection by use of a wedged plate. [25]

A drawback of the wedge prisms comes from the introduction of angular deviation and dispersion. This can be managed by optimisation of the design by combining three (or more) plates. However, this would lead to further losses.

Finally, another advantage is given by the possibility to design the prisms of the phase shifter to compensate a residual chromatism from other components of the interferometer. As a matter of fact, the refractive index of the material in the optical path from Eq. 3.26 can be expanded in a spectral development. This spectral expansion is given by the Sellmeier equation, a polynomial fit of the (n, λ) curve of the material. It has usually the following form:

$$n(\lambda) - 1 = \sum_{i=1}^{N} \frac{A_i^2 \, \lambda^2}{\lambda^2 - B_i^2}. \tag{3.28}$$

This equation, together with the optical thickness of the material, is used to define the operating point $(d_k, n_k(\lambda))$. Residual chromatism from the system can also be expanded in a spectral development:

$$P_{sys} = \sum_{i=0}^{N} A_i^{sys} \, \lambda^i. \tag{3.29}$$

To compensate for the residual chromatism, this polynomial is injected together with the Sellmeier equation in the optical path of Eq. 3.26. The additional term from the system chromatism leads to another design point $(d_k, n_k(\lambda))$.

3.2.3 Past studies

This concept has been studied by Dr. Frank Brachet for his PhD thesis [24]. The objective of his thesis was to develop an achromatic phase shifter. His phase shifter would be tested inlaboratory on the SYNAPSE[2] bench to evaluate its interferometric rejection performance. This work was done in the frame of the future Darwin mission. The ESA at the European Space Research and Technology Centre (ESTEC) also had issued a report on several concepts amongst which the dispersive plates had been evaluated [25].

3.3 The mirror approach

Mirrors intrinsically present an achromatic behaviour concerning phase shift. Thus, if one achieves a phase shift relying only on reflection properties, its achromaticity will automatically be satisfied.

A complete phase-shifter reflective setup comes in two different concepts: the Field Reversal Achromatic Phase Shifter (FR-APS) and the Focus Crossing Achromatic Phase Shifter (FC-APS).

[2]SYNAPSE stands for SYmmetric Nuller for Achromatic Phase Shifters Evaluation

They show two main drawbacks. First, they generate a pupil flip decreasing spatial coherence on the extinction map. A pupil flip results in the generation of two twin images of the planet, leading to a a different spatial distribution of the phase. [20] This leads to SNR[3] worsening and detection capacity weakening. [26]. Second, they only allow a fixed phase shift. Together with a very complex optomechanical adjustment, a possible ellipticity of the beam can be produced due to the dependence of the Fresnel reflection coefficients on the wavelength and the incidence angle[4].

3.3.1 Field reversal

The FR-APS setup takes advantage of the reversal of the s-type polarisation component of the field upon reflection. Any polarisation state can be described by the superposition of two linear polarisations. In the case of incidence on a surface, one is interested mainly in the linear polarisations parallel and perpendicular to the plane of incidence. Those are defined as the s- (perpendicular) and p-(parallel) type polarisations.

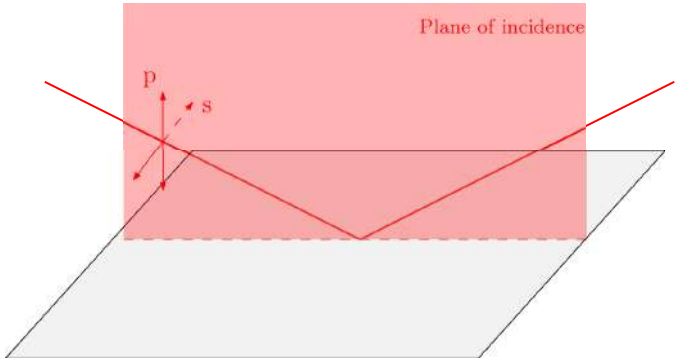

Figure 3.3: Representation of the s and p orthogonal polarisations upon reflection on a surface.

The reversal of the s-type polarisation is highlighted by the minus sign in the Fresnel coefficients for s-type polarisation[5]:

$$\rho_s = -\frac{\sin(\theta_i - \theta_t)}{\sin(\theta_i + \theta_t)}, \qquad \text{and} \qquad \rho_p = \frac{\tan(\theta_i - \theta_t)}{\tan(\theta_i + \theta_t)}. \tag{3.30}$$

The Fresnel coefficients are derived from the Fresnel equations. These equations describe the behaviour (reflection and transmission) of electromagnetic radiation at incidence on an interface between different media. The coefficient provides the ratio of the reflected and transmitted electric and magnetic fields to the incident ones.

This concept can be implemented following two setups.

3.3.1.1 Roof-mirrors setup

The principle of operation of the roof-mirrors setup is schematically presented in Fig. 3.4. Two set of orthogonal mirrors are disposed orthogonally on both sides of a beam splitter (see

[3]The Signal-to-Noise Ratio (SNR) is a figure of merit of a system. It is given by the ratio of the intensity of the signal of interest divided by the noise. Any signal system designer aims for the largest SNR possible, by enlarging the signal intensity or decreasing the noise.

[4]The incidence angle is uniform for a flat mirror, but not for a focusing surface.

[5]The phase shift is given by the fact that the minus sign corresponds to $(-1) \times [...]$, which can be rewritten $e^{i\pi}$. In the $e^{i\pi}$ resides the π phase shift.

Fig. 3.4b). Each incoming beam called A and B are split by a beam splitter at the entrance. The transmitted part (denoted with subscript t) is phase-shifted before recombination with the reflected part (denoted with subscript r) of the other beam.

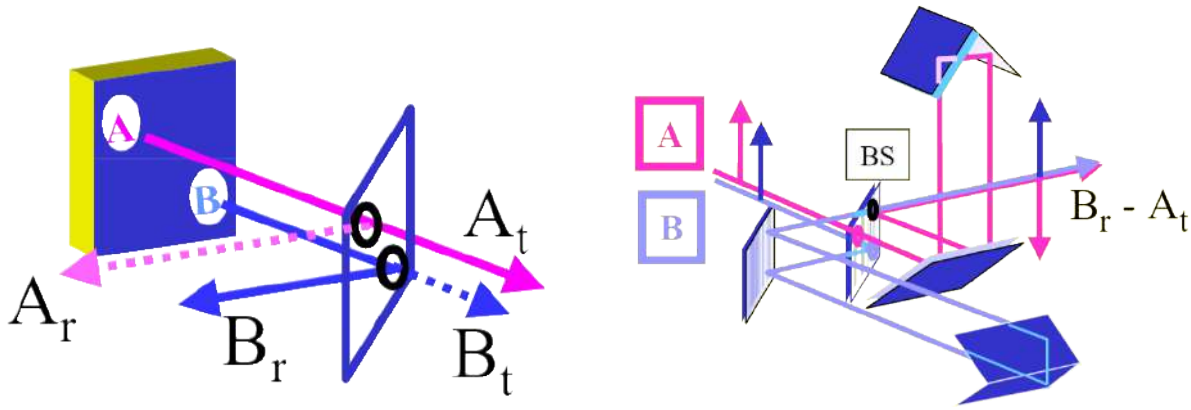

(a) Input geometry and beam splitter operation for arms A and B.

(b) Total setup.

Figure 3.4: Schematic representation of the APS concept based on roof-mirrors. Blue and pink arrows represent one linear state of polarisation, which is reversed according to relative orientation with mirror surface. The resulting polarisations are opposed at output of the APS (extreme right). [27]

This configuration is complicated and delicate and would likely induce path length instability. Furthermore, it implies having to deal with the vertical dimension of the setup. A fully symmetric setup has been developed to counter such drawbacks. [28] It has rather quickly been preferred over the previous one.

3.3.1.2 Fully symmetric nulling beam combiner

The idea here is to use two right-angle periscopes to permute the differential phase shift across each polarisation according to the interferometer arm as shown in Fig. 3.5.

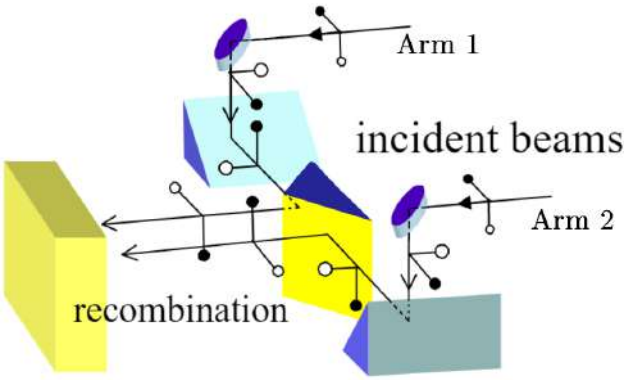

Figure 3.5: Periscope-like arrangement performing the π phase shift. The phase shift comes from successive polarisation reversal (see evolution of light dots (s polarisation) and dark dots (p polarisation) such that at recombination, each polarisation is opposite with the other arm. Extracted and modified from [29].

Afterwards, a conventional constructive interferometer can be used to perform recombination (Mach-Zehnder, Sagnac, Michelson). For better beam symmetry (symmetrical system) and propagation loss (minimum reflections), a modified Mach-Zehnder has been preferred by the ESA team in charge of the APS choice. An advantage is the use of identical beam splitters at separation and recombination, allowing to use of non-symmetric beam splitters without degrading the nulling. The nulling of nonsymmetric designs is impacted by unequal reflections as they depend on whether the light firstly meets the coating or the substrate. Moreover, the light in each beam propagates through the different thicknesses of material. In each path, either the light experiences a different process at the coating-substrate interface. For example, if the substrate is first met, the corresponding beam will experience reflection at the interface and propagate twice through the substrate (forward and backward). The other beam experiencing transmission will propagate only through the substrate then through the coating. Figure 3.6b shows the modified Mach-Zehnder setup with an external Optical Path Difference compensation incorporated to mix properly the beams at recombination. [27]

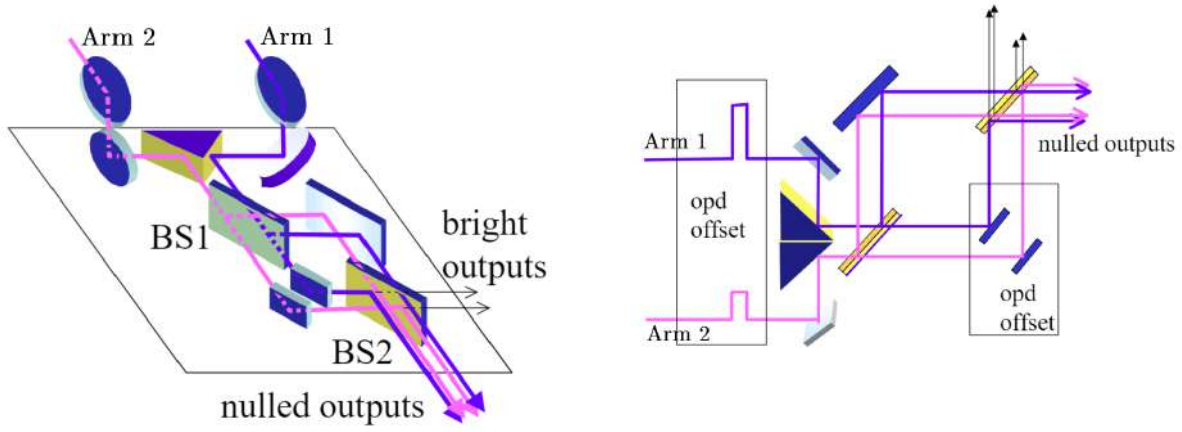

(a) Global 3D view of the setup.

(b) Top view with highlight of OPD compensation.

Figure 3.6: Fully symmetric phase shift by field reversal incorporated in modified Mach Zehnder beam combiner. [27]

3.3.2 Focus crossing

The FC-APS also relies on an only-mirrors setup providing an intrinsically achromatic behaviour. It departs from the electric field reversal concept shown earlier by the phase shifting process. While the FR-APS used the s-type polarisation reversal by mirror reflection, this concept takes advantage of the Gouy phase shift. The Gouy effect states that a converging light wave experiences a $\pi/2$ phase shift in each perpendicular direction when crossing its focus. Hence, this concept allows producing π (spherical focus) and $\pi/2$ (cylindrical focus) phase shifts[6].

The $\pi/2$ case can be described as a limiting case of an astigmatic lens. Astigmatic lens will induce two separate foci, each inducing the half π phase shift and the cylindrical lens is the case of extreme astigmatism.

[6] A cylindrical lens can be described as a spherical lens with an infinite radius of curvature in one direction. The focus in this direction (and the correlated $\pi/2$ phase shift) is then operated at infinity.

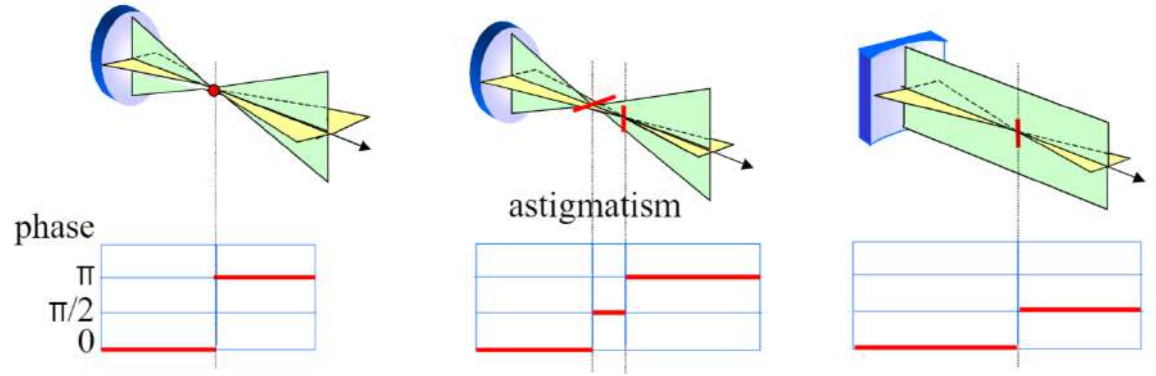

(a) Common focus: π shift at once.

(b) Astigmatic lens: two successive $\pi/2$ shifts.

(c) Cylindrical lens: single $\pi/2$ shift.

Figure 3.7: Gouy phase shift at focus crossing according to lens curvature. [27]

Two designs can provide the desired focus crossing. They all rely on each arm with respectively converging and planar reflections. The beams can be considered as emerging from two telescope apertures or generated by a beam splitter. Two different setups exist the cat's eye system (see Fig. 3.8a) and the confocal system[7] (see Fig. 3.8b).

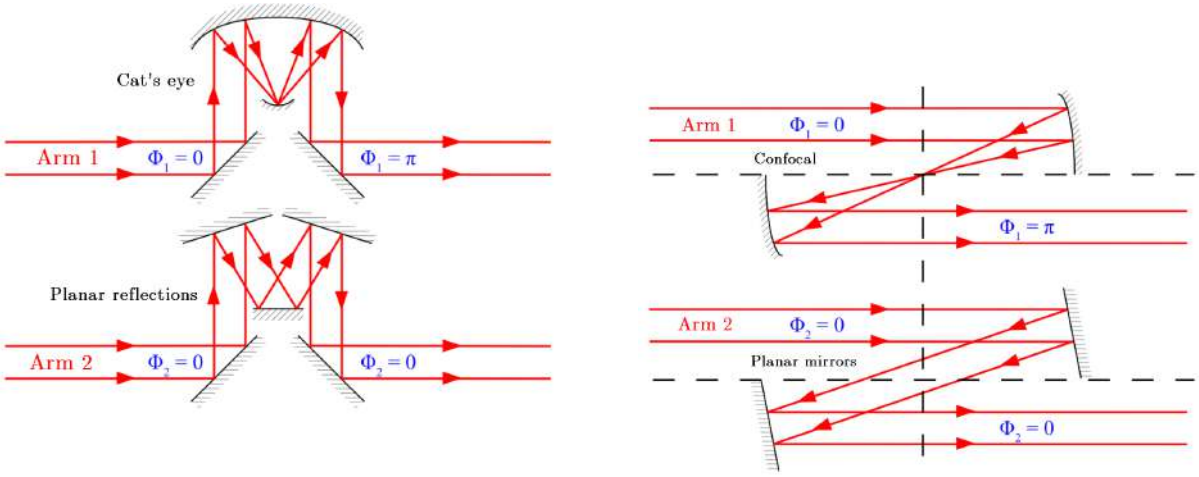

(a) Cat's eye and triple planar.

(b) Confocal and double planar.

Figure 3.8: FR-APS designs. [24]

3.3.3 Past studies

For the Field Reversal Achromatic Phase Shifter the main provider was E. Serabyn [30, 31]. Concerning the Focus Crossing Achromatic Phase Shifter Y. Rabbia was the main investigator, and the Achromatic Interfero Coronagraph (AIC) used such concept [32, 33, 34].

[7] The confocal system can be seen as a deployed cat's eye.

3.4 Rhombs

The rhombs present an advantage over the previously discussed dispersive prisms concept: their implementation is straightforward. They also do not provide any pupil flip such as the mirror approaches presented. They provide the phase shift by reflection at interfaces of isosceles prisms.

3.4.1 Fresnel rhombs

The rhombs rely on the Total Internal Reflection (TIR) phenomenon. This phenomenon is explained by looking carefully at the law of reflection and refraction. When a wave encounters an interface of two media with different refractive indices, its energy is split into a refracted and reflected wave. In the case of an incident refractive index n_1 greater than the emergent refractive index n_2, beyond a critical incident angle θ_c the energy will be fully concentrated in the reflected wave. The angle of incidence on the interface (θ_1), and the angle of refraction (θ_2) are linked through the Snell-Descartes law:

$$n_1 \sin(\theta_1) = n_2 \sin(\theta_2). \tag{3.31}$$

The critical incident angle is physically defined as the angle θ_1 for which the refracted angle $\theta_2 = \pi/2$. This implies that the refracted wave is parallel to the interface: this is the limiting case between refraction and TIR. For incident angles greater than θ_c, the Snell-Descartes law will result in a $\sin(\theta_2)$ greater than unity: this has no solution! The threshold for Total Internal Reflection is therefore given by the mathematical limit of Snell-Descartes law:

$$\frac{n_1}{n_2} \sin(\theta_c) = 1 \longrightarrow \theta_c = \arcsin\left(n_2/n_1\right). \tag{3.32}$$

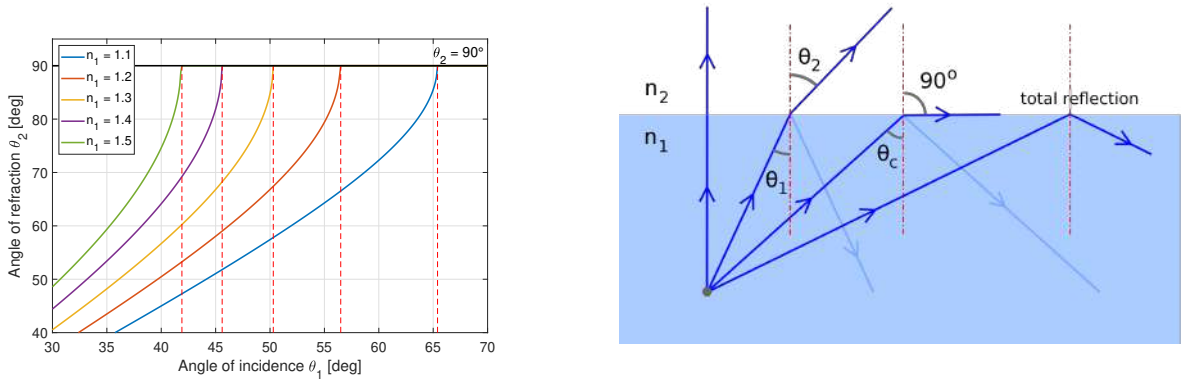

(a) Evolution for different incident refractive indices n_1 of the refraction angle for an emergent refractive index $n_2 = 1$.

(b) Schematic representation of the phenomenon. en.wikipedia.org

Figure 3.9: Snell-Descartes law behaviour and the Total Internal Reflection (TIR) phenomenon.

Therefore for $\theta_1 > \theta_c$ there is no refracted wave, the whole energy is reflected: this is the Total Internal Reflection. During such process, a phase shift is operated between vectorial s and p components of the field. Defining n_i, n_t as the refractive indices of incident, emergent media and $n_{ti} = n_t/n_i$, the vectorial phase shift is given by :

$$\Delta\phi_{s-p} = 2\arctan\left(\frac{\sqrt{\sin^2\theta_i - n_{ti}^2}}{n_{ti}^2\cos\theta_i}\right) - 2\arctan\left(\frac{\sqrt{\sin^2\theta_i - n_{ti}^2}}{\cos\theta_i}\right), \tag{3.33}$$

where θ is the angle of incidence.

The variation of the phase shift according to the incidence angle $\partial\phi/\partial\theta$ shows a maximum at an angle θ_{max} given by the system parameters. The design of the refractive index and incidence angle allows to smooth the gradient, but nevertheless, its magnitude increases when θ_i departs from θ_{max}, consequently the tolerance on pointing reduces as well.

The phase shift obtained is $\pi/2$ between the input and output polarisations. For example, an input linear polarisation becomes circularly polarised (see Fig. 3.10b). The π phase shift can be achieved by cascading two regular Fresnel rhombs as illustrated in Fig. 3.10c. This setup would be inserted in one arm of the interferometer causing a modification of the optical path. Another material has to be placed in the second arm to compensate for this, but only one direction of polarisation would be usable. However, the specific arrangement shown in Fig. 3.10d imagined by J. Gay might provide the desired phase shift in dual polarisation mode. In this setup, the incident wave is split into two orthogonal polarisations. Both components experience the phase shift by cascading through two Fresnel rhombs placed orthogonally. After recombination of the light, the incident wave is retrieved, phase shifted by π.

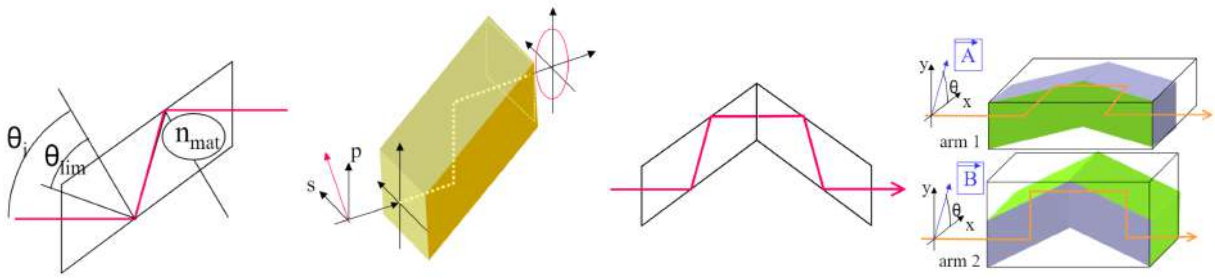

(a) Generic use. (b) Frequent use. (c) Rhombs in cascade. (d) Orthogonal disposition.

Figure 3.10: Schematic presentation of Fresnel rhombs utilisation. [29]

3.4.2 Composite rhombs

Also called twisted rhombs, these elements depart a bit from the Fresnel rhombs presented above. In this setup, the prisms have unequal refractive indices and are assembled in such a way that the wave encounters successively perpendicular planes of incidence (see Fig. 3.12). The

chromatic phase shift experienced during prism propagation[8] is added to the achromatic phase shift induced by total reflection[9].

If we denote the successive prisms by the indices 1 and 2 then ϕ_{p1}, ϕ_{p2} and $\phi_{s1}, \phi s2$ would be the achromatic phase shifts at total reflection according to their respectively p-type, s-type polarisation in prism 1 or 2. For the first arm (called A here for the sake of clarity), considering a p-polarisation, the incident wave experiences the following phase shifts:

i Chromatic between input and interface in prism 1 ($\phi_{\text{i}} = \dfrac{2\pi}{\lambda} n_1 d_{\text{in},1\rightarrow\text{refl},1}$);

ii Achromatic from total reflection with p-polarisation ($\phi_{\text{ii}} = \phi_{p1}$);

iii Chromatic between interface and output in prism 1 ($\phi_{\text{iii}} = \dfrac{2\pi}{\lambda} n_1 d_{\text{refl},1\rightarrow\text{out},1}$);

iv Chromatic between input and interface in prism 2 ($\phi_{\text{iv}} = \dfrac{2\pi}{\lambda} n_2 d_{\text{in},2\rightarrow\text{refl},2}$);

v Achromatic from total reflection with s-polarisation ($\phi_{\text{v}} = \phi_{s2}$);

vi Chromatic between interface and output in prism 2 ($\phi_{\text{vi}} = \dfrac{2\pi}{\lambda} n_2 d_{\text{refl},2\rightarrow\text{out},2}$).

The whole setup is presented in Fig. 3.11, with Fig. 3.11a showing the arm A with the successive phase shifts i to vi and Fig. 3.11b showing the arm B.

[8] This phase shift is considered polarisation-independent by assuming non-birefringent material.

[9] Which is, as explained earlier, polarisation dependent (see equation 3.33).

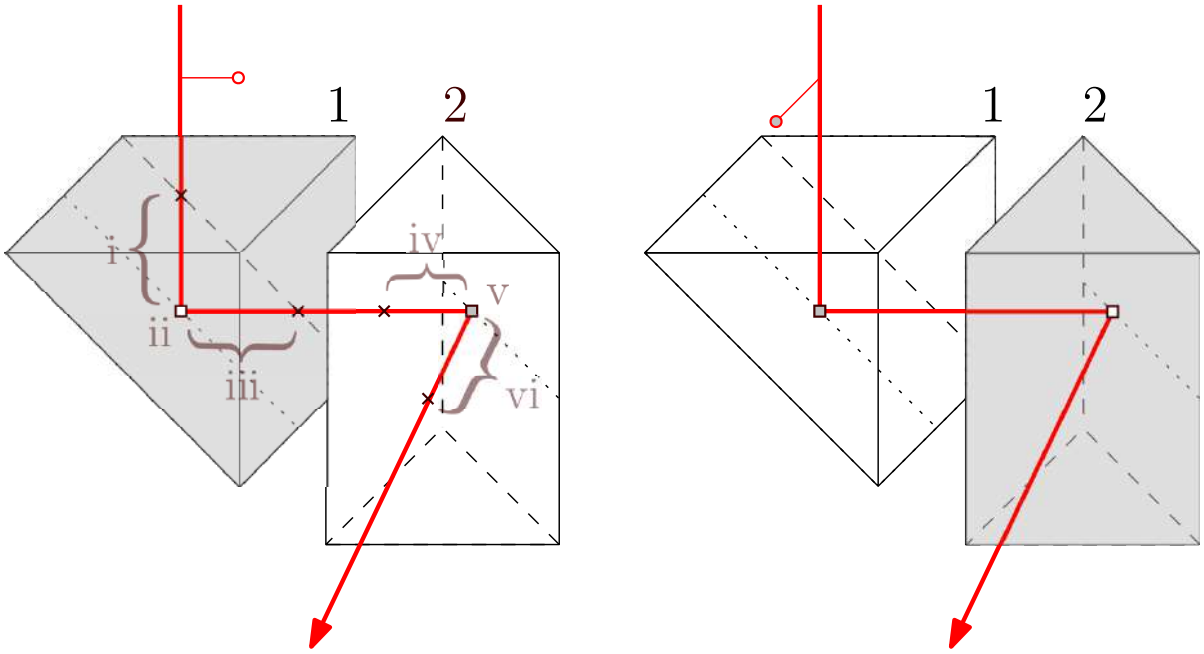

(a) Successive phase shifts encountered by the wave in arm A.

(b) Setup in arm B. Rhombs have same symmetry but materials are inverted.

Figure 3.11: Representation of an APS setup made of composite rhombs. The boxes stand for achromatic phase shift at reflection. White, grey coloured marker stand for p,s polarisation respectively.

The chromatic phase shifts i + iii and iv + vi can be regrouped in one term as the refractive indices are considered polarisation independent. Defining d_1, d_2 as the propagation lengths in prism $1, 2$ respectively, we obtain:

$$\phi_{\text{i}} + \phi_{\text{iii}} = \frac{2\pi}{\lambda} n_1 d_1 \qquad \text{and} \qquad \phi_{\text{iv}} + \phi_{\text{vi}} = \frac{2\pi}{\lambda} n_2 d_2. \tag{3.34}$$

The total phase shift can finally be written:

$$\Delta\phi_A = \underbrace{\frac{2\pi}{\lambda} n_1 d_1}_{\text{i+iii}} + \underbrace{\phi_{p1}}_{\text{ii}} + \underbrace{\frac{2\pi}{\lambda} n_2 d_2}_{\text{iv+vi}} + \underbrace{\phi_{s2}}_{\text{v}}. \tag{3.35}$$

Similarly, for the second arm denoted B we obtain directly by permuting the refractive indices between prisms and taking a s-type incident polarisation:

$$\Delta\phi_B = \frac{2\pi}{\lambda} n_2 d_1 + \phi_{s1} + \frac{2\pi}{\lambda} n_1 d_2 + \phi_{p2}. \tag{3.36}$$

The phase difference between the interferometric arms is given by the subtraction of Eq. 3.35 and Eq. 3.36:

$$\Delta\phi = \Delta\phi_A - \Delta\phi_B = \frac{2\pi}{\lambda}\Big[(n_1 - n_2)\,(d_1 - d_2)\Big] + (\phi_{p1} + \phi_{s2} - \phi_{s1} - \phi_{p2})\,. \tag{3.37}$$

The first term is the only chromatic one. Provided that the rhombs have the same geometry (that is mathematically $d1 = d_2$) this term cancels out. In this case, the phase shift is governed by achromatic terms. Those terms can be designed through the refractive index and angles of incidence as shown in Eq. 3.33 to reach the desired phase shift value. A representation of the 3d layout of the setup is shown in Fig. 3.12.

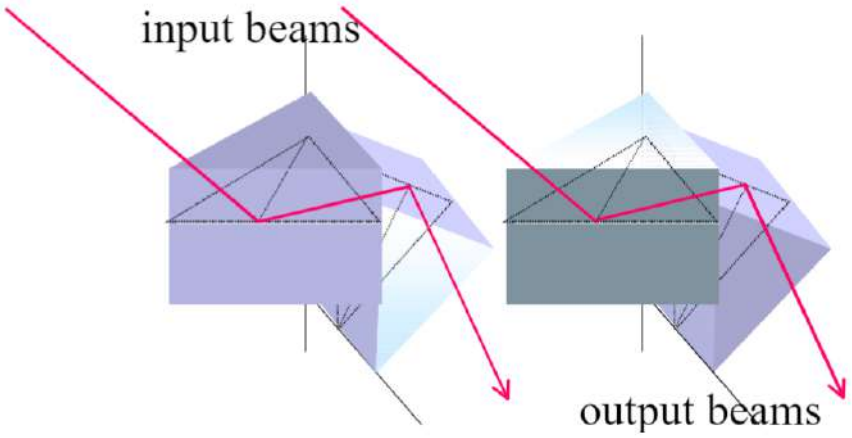

Figure 3.12: 3D layout with permutation of materials between prisms and both arms. [29]

Both concepts (Fresnel and composite rhombs) suffer from high sensitivity to refractive index inhomogeneity which can be problematic when one considers the bulk volume needed for the prisms. Peculiar attention must be brought to the coatings at interfaces to avoid too high Fresnel losses.

3.4.3 Past studies

Mawet *et al.* from the ULiège proposed the use of subwavelength gratings for the interfaces and provided experimental results on the performance [35, 36]. The subwavelength grating showing a groove step smaller than the field wavelength, only the zeroth order mode is transmitted, reflected, and refracted.

3.5 Integrated optics

Integrated optics is the last breakthrough and genuine revolution in the optics domain. Its advent made scientific develop new approaches and new possibilities that were not achievable before. As in the most cases, for the development of an APS in integrated optics do not come

with an out-of-the-box solution, but rather represents the final step in miniaturisation and stability. Not all previously explained concepts are feasible in integrated optics, and this domain is still young. Its youth provides challenges but also hopes new solutions thanks to technological evolution.

3.5.1 Overview

Integrated optics is a recent technology aiming at constructing photonic integrated circuits or integrated optical devices. Such elements are combined to fulfil simple or complex functions. Some examples are optical fibres, modulators, amplifiers, lasers, etc.

The technology is inspired by the rise of integrated electronics. Electronics for the last decades has shown very rapid development, leading to amazing achievements such as microprocessors or computer memory chips. However, integrated optics involve technological complications that are still too great to match the electronic development curve:

- Waveguides are limited in size by parameters such as the wavelength of operation, while electronic devices can contain extremely small components.
- Optical connections, couplers and waveguides are extremely more critical (bend loss, matching, etc..);
- Optical amplifiers compensate the losses presented above but are larger and more complex than electronic amplifiers;
- The miniaturisation process in itself for optical components involves more complicated technological challenges.

For wavelengths negligible compared to the system characteristic dimension, geometrical optics are sufficient to predict light behaviour. However, when the system size becomes comparable to the wavelength, one has to turn towards an electromagnetic description. As many physical quantities, light propagation is described by differential equations: the Maxwell equations.

Combined with continuity and boundary conditions, those equations provide a set of discrete solutions. Several solutions may coexist with different parameters, depending on the values that satisfy the Maxwell equations. Those separated solutions are called modes of propagation.

Those modes show a spatial and temporal evolution that is quasi-deterministic: for an integrated system source-waveguide with fixed parameters, we can determine the propagating modes. By careful design, a single-mode waveguide will only allow one mode propagating through. The propagation of this mode does not depend on the aberration of the light prior to the confinement in the waveguide. This means that the waveguide exerts spatial filtering on the field. The propagated mode at the output will show a defined profile given by the conditions of propagation of the waveguide, independently of the aberrations prior to the integrated component.

3.5.2 Mirror approach

The first concepts subject to miniaturisation are the mirror approaches such as metallic reflection and focus crossing.

3.5.2.1 Metallic reflection

The metallic reflection can be achieved in two ways. First by depositing a metallic thin film on the planar area at the end of the substrate. To avoid energy losses at the interface, tapers are inserted before the reflection region. The second possibility is to directly create a metallic part as a waveguide in itself, leading to a less sensitive component but with more manufacturing steps.

To maintain optical path equivalent, the other arm will have an unfolded version with the tapers facing each other to reach the same optical paths in both arms.

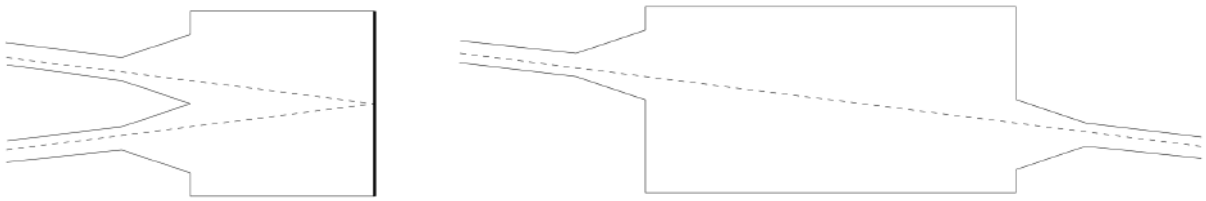

(a) Metallic reflection.

(b) Symmetric path in other arm.

Figure 3.13: Quasi-normal reflection at metallic interface in integrated optics. [37]

3.5.2.2 Focus crossing

In this case, the focus is achieved by designing the border between the guiding part and the substrate with a precise curved shape. Tapers again enlarge the beam resulting in an almost collimated one and after being phase shifted through the focus crossing the beam is coupled again to the output waveguide. The other arm will present the same design but with planar surfaces with the same interfaces and number of reflections to mimic the path without having focused the beam.

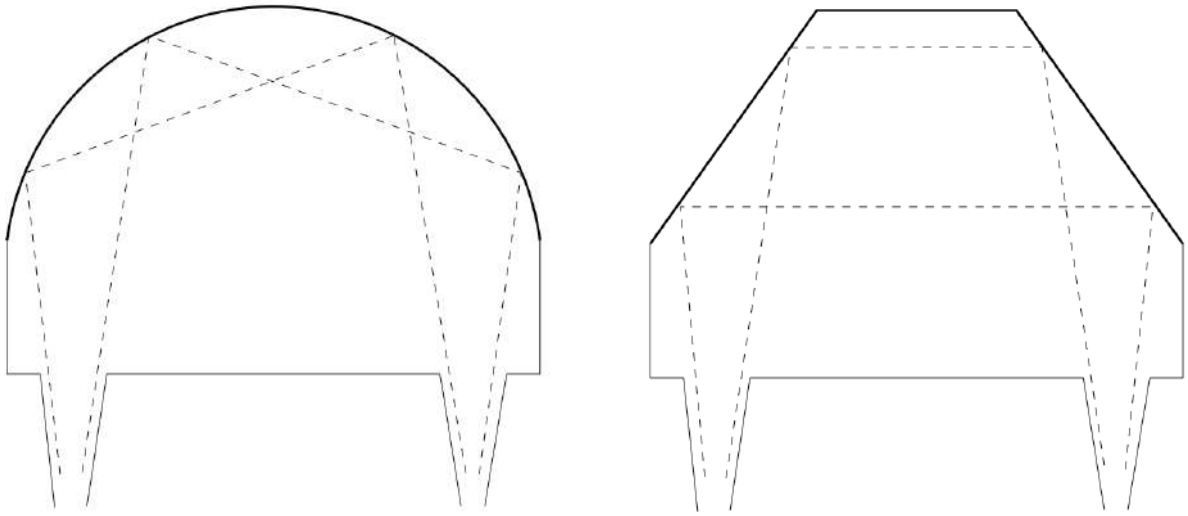

(a) Focus crossing.

(b) Planar reflection.

Figure 3.14: Focus crossing APS using integrated optics. [37]

3.5.3 Dispersive waveguides

While the mirror approach was completely about miniaturising the previous APS bulk setup, this one consists in using the same idea but applied to integrated optics. The phase shift will be obtained through the same principle as in Sec. 3.2. With bulky optics, only the refractive index, thickness, and possible coatings were determining the phase shift. For integrated optics, the design parameters are different.

As a matter of fact, the propagation in waveguides is directed by the Maxwell equations applied to the symmetry of the system. It produces discrete values of propagated solutions corresponding to modes. Such conditions for propagation depend on the geometry of the waveguide and provides the theoretical corresponding medium that the light experiences[10]. In this case, the geometry of the waveguide plays a role as important as its refractive index. One of the key parameters in integrated optics is the refractive index difference Δn between the core and the cladding.

Modifying the waveguide parameters between both arms will lead to a phase shift between both arms due to the difference of effective refractive indices experienced by the field during propagation. However, as the refractive index is wavelength dependent, using only one section of varying waveguide parameters would lead to a chromatic phase shift. The solution resides in the use of several segments of varying parameters to compensate for the chromatism of the previous sections.

[10]The refractive index that the field undergoes during propagation depends on the medium refractive index but on the geometry as well. Thus, the light is modified as if it had been propagating through a medium with a refractive index $n \neq n_{\text{mat}}$: the effective index.

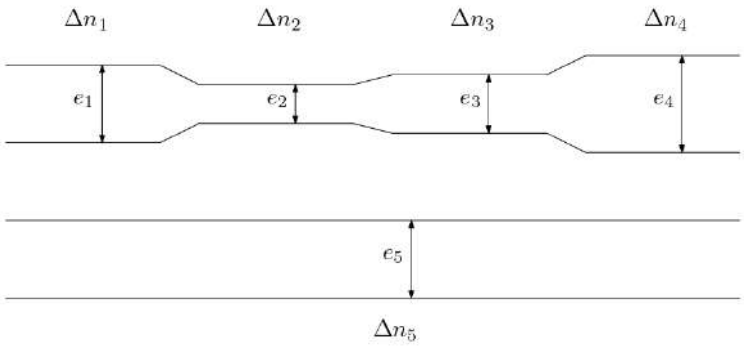

Figure 3.15: Dispersive waveguides with modified sections parameter to compensate for chromatic phase shift [37].

The design of the section parameters (geometry, refractive indices of the core and cladding, refractive index difference, etc) requires simulation tools prior to manufacturing for experimental tests.

Several waveguides exist and can be compared, the main ones being optical fibres (cylindrical geometry), and rectangular waveguides split between dielectric ones (as optical fibres but with rectangular geometry) and the Hollow Metallic Waveguides (HMW) showing a hollow core with a metallic film deposited on the inside of the core-cladding interface confining light by reflection.

This concept will be further investigated in Chap. 5.

3.5.4 Past studies

Optical fibres have been used in astronomy for spatial filtering thanks to the modal physical selection of the conditions of propagation but not as phase shifters yet. P. Labeye used a dielectric rectangular APS for its thesis about an integrated chip for 4-telescopes interferometry in the H band [38]. L. Labadie investigated HMW in its thesis [39] and in several articles [40, 41].

3.6 Other concepts

Different approaches have been investigated but none of those reached an interest higher than the previously presented ones. They are nonetheless described here for the sake of completeness.

Multi-layer coatings The principle is to deposit a different coating on the mirrors to achieve the phase shift at the reflection. Designing the number of layers, their thickness, refractive index, and interface coefficients would allow reaching achromaticity while keeping high reflection efficiency. Due to the absorptivity features, temperature sensitivity, and manufacturing difficulties, this concept has been discarded [37].

Birefringent plates Light propagating through a cascade of usual birefringent plates (such as quarter-wave or half-wave plates) experiences a chromatic phase shift. Through careful design again, the competing dispersion effects could cancel out mutually to achieve an achromatic phase shift. The Jones matrices provide an algebra for the process, and the Poincaré sphere a graphical representation. However, the spectral bandwidth asks for a large number of plates which result in energy losses and bulky setup, and on that account, this concept is not selected [29, 37].

Four quadrants Four quadrants mask separates the focal plane into four symmetrical sectors amongst which two of them present a phase shift due to multilayer treatment of the mask, while the two others leave the phase unchanged. Thanks to the coronagraphic axial effect, a perfectly centred source see its light rejected thanks to the Lyot stop, while an off-centre source will be detectable thanks to the fast off-axis attenuation of the effect [24, 42].

Holographic gratings The light travels through the transmission gratings but the phase shift results from a diffraction process. The light propagates through the three gratings and its phase shift comes from a chromatic part (optical path) and an achromatic part induced by a perpendicular translation of the central grating. Differential use allows cancelling mutually chromatic terms at recombination. But this concept has been deemed not adapted for dual polarisation, and as each polarisation is treated differently through the gratings, the concept is not interesting [37, 29].

3.7 Discussion

This final section aims at summarising the main advantages and drawbacks of each concept, before selecting a few candidate concepts for further investigation to determine the concept finally best suitable.

3.7.1 Dispersive plates

Advantages A careful design of the number, thickness and refractive index of plates can lead to any phase shift value. Residual chromatism from other elements of the system can be incorporated in the design to be compensated as well. It does not perform pupil inversion nor is expensive. The versatility of this setup allows to opt for several solutions between optimisation with respect to spectral band division, the number of plates, or material selection where the number of plates can be as low as three or four. Straylight is avoided through the use of wedged prisms.

Drawbacks The main problem in this concept is the optical transmission which relies on antireflection coatings for the wavelength of interest as well as high throughput during in-prism propagation. Moreover, low refractive index materials interesting for their high transmission

are also the most complex to manufacture and less reliable. On the other side, it asks for high mechanical stability and results in a bulky element.

3.7.2 Rhombs

Advantages As the dispersive prisms, the rhombs allow tuning the phase shift. The special orthogonal disposition makes a dual-polarisation mode functional and the achromaticity is intrinsic.

Drawbacks The setup requires a high alignment accuracy, and transmission has to be enhanced. Sub-wavelength gratings are one challenging proposed solution to this setback.

Peculiarly to composite rhombs, they present a residual chromatism, high temperature sensitivity, unusual bending of the beams and do not provide dual-polarisation.

3.7.3 Mirror approach

Advantages Both are setups with mirrors only, leading to very easy material selection for the wavelength of interest regarding availability, price, and manufacturing while providing intrinsic achromaticity over whole bandwidth and hope for a great throughput thanks to high reflection efficiencies and no Fresnel loss by mirrors. The symmetric beam splitter crossing proposed by the setup allows to relax the constraints about the chromaticity of the reflection and transmission coefficients.

Drawbacks The high throughput happens only for the simultaneous use of both polarisations, which measurement seems to prove complicated because of the ellipticity generated by metal reflection. Moreover, this setup is very stringent regarding optical path instabilities as it implies separate elements[11]. Also, it only allows a precise π or $\pi/2$ phase shift. The control of the OPD has to be made carefully even when considering the external delay line. Very high care must be brought during alignment and the elements fixation to ensure their immobility.

Specifically for the focus crossing concept, the cat's eye setup asks for a focus on an optical surface which requires very high surface quality and very good operation conditions.

3.7.4 Integrated optics

Advantages The main and paramount advantages are the possibility to combine several elements of the interferometer in one and the compactness and stability. The modal propagation allows for spatial filtering and avoids wavefront distortion and erases wavefront errors from previous elements while the setup remains very small. Recent technological advances allow aiming for complex components to the nanometric scale. The alignment constraint is relaxed as the

[11] This could be tackled by compacting the architecture using molecular contact assembling.

design of the component mask takes charge of it. The use of a single substrate also reduces drastically the sensitivity to external conditions such as temperature, pressure, or even show a good resilience to vibrations because of their small size and one-component design.

Drawbacks The technology is currently mastered for telecommunications but needs to grow and is yet to be proven for space applications even though expectations are high.

3.7.5 Selected concepts

An APS based on Fresnel rhombs, enhanced by a subwavelength grating, could provide good performance. The advantage of an intrinsic polarisation reversal during Total Internal Reflection leads to a stable and achromatic phase shift. However, their material dispersion and throughput must be studied with care taking into account the bandwidths considered. Wedged prisms are interesting because of their simplicity, but a design relying on propagation through prisms could also suffer from throughput considerations because of the bandwidths of this work. Nonetheless, realising an integrated APS seems to be the best solution. Providing function combination (spatial filtering and phase shifting), compactness, great mechanical stability and ability to tune the phase shift, this concept is the most promising one.

Chapter 4

Discarded concepts

This chapter focuses on two concepts that have been investigated but lately discarded: wedged prisms and Fresnel rhombs. Both concepts rely on bulk optics, subject to delicate mechanical stability and vibrations management. Moreover, the two first spectral bands correspond to mission size of CubeSat 6U and 12U. These concepts could result in a final design of size too great for such small satellite constraints. Thus, they are primarily oriented towards the two larger missions, PROBA and FKSI with larger spectral bands.

4.1 Wedged prisms

First will be studied an APS based on dispersive plates to provide a compensated phase shift. This concept relying on dispersion is presented in Section 3.2. Its operation consists of free space propagation through dielectric prisms. A collimator generates a collimated beam from the optical fibres.

It has been used in several configurations across different projects. One can use very weakly prismatic plates slightly inclined to deflect spurious reflections. [43] Another solution is to combine translation and rotation of dispersive plates with parallel interfaces. [44] Based on an idea from [45], Dr. F. Brachet designed a system with two head-to-tail prisms one after the other in each arm. [24] One of them is mounted on a translation stage along its wedged facet to provide the differential medium thickness in one arm.

The rejection ratio can be enhanced by introducing more materials (with different dispersion behaviour) leading to other pairs of prisms in the interferometer, but the overall throughput suffers from it. To reduce as much as possible the losses, the materials have to be carefully chosen.

4.1.1 Equations

As mentioned in Section 3.2, the target phase shift is obtained through compensated dispersion by designing the thickness of medium propagation and OPD by refractive index choice. The translation stage combined with the wedged angle allows to finely tune the desired thickness to reach the best operating point.

The OPD is given by the supplementary free space propagation in the arm with the sliding prism[1]. The phase shift between both arms directly depends on the thickness variation imposed in the sliding arm, modifying the free space propagation and the optical path through the material. the system is represented schematically in Figure 4.1. Defining n_{FS} as the refractive index to be considered in the free space propagation[2] and t the thickness of the sliding prism, the phase shift is given by:

$$\Delta\phi(\lambda) = \frac{2\pi}{\lambda}\left[n_{FS}\left(OPD + t\right) - OPD * n_{mat}(\lambda)\right], \tag{4.1}$$

which can be rewritten by grouping terms depending on thickness t and Optical Path Difference (OPD) terms as:

$$\Delta\phi(\lambda) = \frac{2\pi}{\lambda}\left[OPD * n_{FS} + t\left(n_{FS} - n_{mat}(\lambda)\right)\right]. \tag{4.2}$$

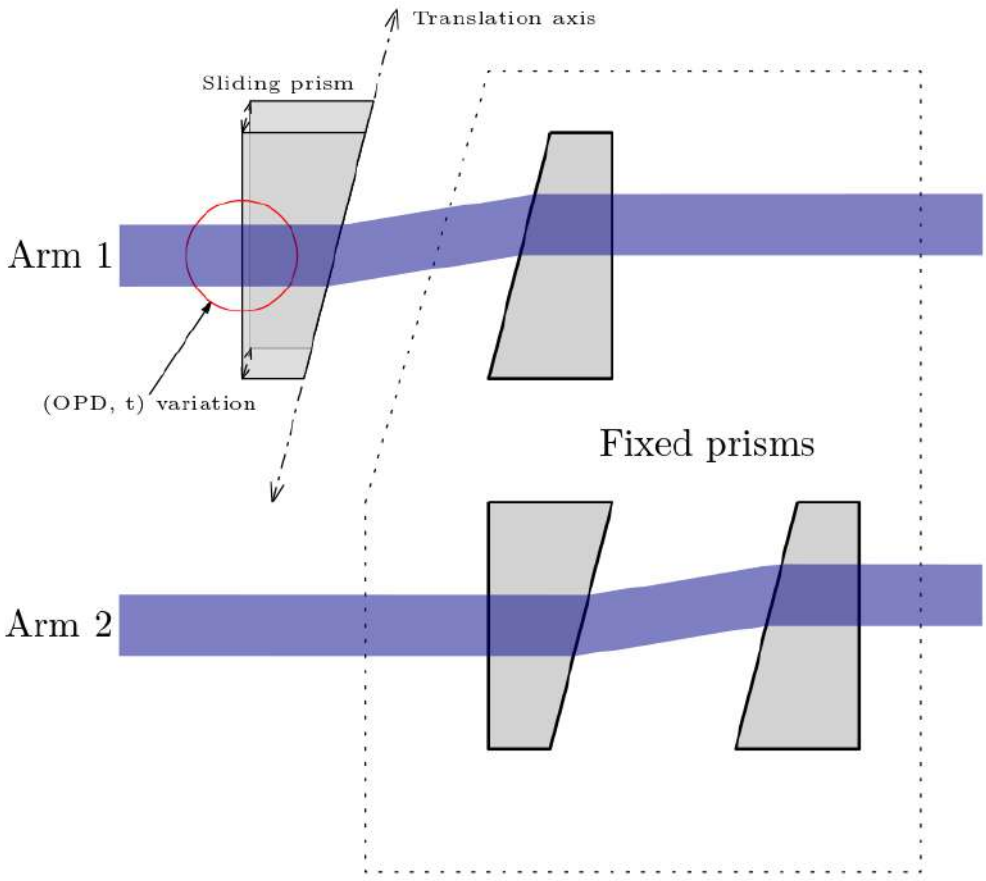

Figure 4.1: Sliding prism phase shifter

[1]This arm will now be called the sliding arm.

[2]Valid assumption is to take the case of the vacuum $n_{FS} = n_{vac}1$ or even of the air $n_{FS} = n_{air} \approx n_{vac}$.

The thickness is directly given by trigonometry, introducing θ_{wdg}[3] as the wedge angle of the prism and x as its translation along the wedge axis, yielding the phase shift:

$$\Delta\phi(\lambda) = \frac{2\pi}{\lambda}\left[OPD * n_{FS} + x\,\sin(\theta_{wdg})\,(n_{FS} - n_{mat})\right]. \tag{4.3}$$

This equation nonetheless relies on a perfect geometry (alignment, parallelism) of the system.

4.1.2 Material selection

The selection of the prisms material is crucial. It affects the design point and rejection ratio through its refractive index. It delineates the acceptable spectral band and defines the total throughput. Furthermore, as the optical path impacts the rejection ratio, the thermooptic and thermal expansion coefficients must be precisely known. Both will ensure a good simulation of the behaviour of the setup when cooled down from room temperature to spatial conditions. Finally, the achievable accuracy over the surface roughness must be taken into account as well.

The methodology followed is in line with the work done regarding the Darwin mission. [25] Usual infrared glasses are compared and their properties regarding the spectral band of interest in this work are analysed. The refractiveindex.info database is used for the most common properties of the materials (refractive index, Sellmeier equation, transmittance, etc). The materials under scope here are zinc selenide, germanium, fluoride, thallium bromo-iodide, and chalcogenide. Other materials commonly used have been discarded because of several properties such as water moisture (CsBr, CsI, KBr, KCl), toxicity (CdTe), or anisotropy (Al_2O_3). All these particular properties made the materials more complicated to manufacture or to handle.

4.1.2.1 Zinc selenide (ZnSe)

Zinc selenide (ZnSe) is a light-yellow intrinsic semiconductor. Providing an interestingly wide transmission range (0.45 to 20 μm), it is a commonly used infrared material. It shows a low refractive index with a value of around 2.4.

The database provides the following Sellmeier equation from measurements by Amotchkina *et al.* in 2020:

$$n^2 - 1 = -0.689818 + \frac{4.855169\,\lambda^2}{\lambda^2 - 0.056359} + \frac{0.673922\,\lambda^2}{\lambda^2 - 0.056336} + \frac{2.481890\,\lambda^2}{\lambda^2 - 2222.114}. \tag{4.4}$$

4.1.2.2 Germanium (Ge)

The germanium is a chemical element with atomic number 32. It belongs to the carbon group and shows similarities with silicon and tin. Most of the first generation of semiconductor electronics were made of germanium, and presently it appears mainly in fibre optics, infrared

[3] See Fig. 4.4 for the definition of θ_{wdg}

optics, solar cells and Light-Emitting Diodes. The germanium is a high-index material (around 4).

Its Sellmeier equation reads from 1976 measurements by Icenogle *et al.*:

$$n^2 - 1 = 8.28156 + \frac{6.7288\,\lambda^2}{\lambda^2 - 0.44105} + \frac{0.21307\,\lambda^2}{\lambda^2 - 3870.1}. \tag{4.5}$$

4.1.2.3 Thallium bromo-iodide (KRS5)

The KRS5 is a thallium mixed halide. Its properties are close to the zinc selenide, with an elongated transmission range (up to 40 μm). Its refractive index stands between 2.45 for 1 μm and 2.37 for 10 μm.

The database gives a Sellmeier equation based on measurements from Rodney and Malitson in 1956:

$$n^2 - 1 = \frac{1.8293958\,\lambda^2}{\lambda^2 - 0.0225} + \frac{1.6675593\,\lambda^2}{\lambda^2 - 0.0625} + \frac{1.1210424\,\lambda^2}{\lambda^2 - 0.1225} + \frac{0.05413366\,\lambda^2}{\lambda^2 - 0.2025} + \frac{12.380234\,\lambda^2}{\lambda^2 - 27089.737}. \tag{4.6}$$

4.1.2.4 Chalcogenides

Chalcogenides are glass composed of several elements, specifically engineered for infrared use. Several companies offer different compositions under different trade name[4]. They show good thermo-optic stability and versatility in terms of machining and finishing. They are more expensive because they are specially engineered for this particular use. Their data are presented in Tab. 4.1.

[4] AMTIR comes from Amorphous Materials Inc., GASIR from Umicore Electro-Optic Materials, IG from VITRON Spezialwerkstoffe GmbH, IRG from Schott Advanced Materials. Other makers offer such materials but are not compared here (OPTIR from Rochester Precision Optics and BD from LightPath).

	Units	AMTIR-1 GASIR-1 IG2 IRG22	IG3 IRG23	IG4 IRG24	IG5 IRG2	IG6 IRG26
Refractive index n @ 4 μm	[-]	2.5129	2.8034	2.6210	2.6226	2.7945
Thermo-optic $\partial n/\partial T$	[10^{-6}/°K]	71	130	30	76	35
Density ρ	[g/cm^3]	4.41	4.84	4.47	4.66	4.63
Thermal expansion $\partial L/\partial T$	[10^{-6}/°K]	12.1	13.4	20.4	14	20.8
Hardness	[kg/mm^2]	143	138	114	115	106
Rupture modulus	[psi]	2755	2610	2610	2610	2465

Table 4.1: Comparison of several properties of chalcogenides. The price and availability are of the same order for all materials. The properties are comparable for all, but IRG22 has been selected for its thermal behaviour. Also, its provider (Schott) gives the most complete description of the material. [46]

The Sellmeier equation for the IRG22 in the database is given by:

$$n^2 - 1 = 2.4834 + \frac{2.8203\,\lambda^2}{\lambda^2 - 0.1352} + \frac{0.9773\,\lambda^2}{\lambda^2 - 1420.7}. \tag{4.7}$$

4.1.2.5 Fluorides

Fluoride materials include a composition with several elements such as calcium (CaF_2), magnesium (MgF_2), lithium (LiF), barium (BaF_2). A first quick comparison allows selecting of the best fluoride for this application. The magnesium fluoride MgF_2 is directly discarded because of its birefringence. The data comparison is summarised in Tab. 4.2

	Units	CaF_2	BaF_2	LiF
Price	-	●	●	●
Availability	-	●	●	/
Refractive index n	-	1.42	1.46	1.38
Thermo-optic coefficient $\partial n/\partial T$	10^{-6}/°K	-11	-15.2	-12.7
Density ρ	g/cm^3	3.18	4.89	2.64
Thermal expansion coefficient $\partial L/\partial T$	10^{-6}/°K	18.85	18.1	37
Hardness	kg/mm^2	158	82	102
Rupture modulus	psi	5295	3800	1566

Table 4.2: Comparison of several properties of fluorides. The calcium fluoride CaF_2 is selected for temperature stability, price and availability. [46]

The Sellmeier curve for the calcium fluoride is described by:

$$n^2 - 1 = \frac{0.5675888\,\lambda^2}{\lambda^2 - 0.002526429987596} + \frac{0.4710914\,\lambda^2}{\lambda^2 - 0.010078332802810} + \frac{3.8484723\,\lambda^2}{\lambda^2 - 1200.555972921600}. \quad (4.8)$$

4.1.2.6 Summary of material properties

The Sellmeier equations have been plotted across the spectral band of interest for this work for each material. The result is given in Fig. 4.2.

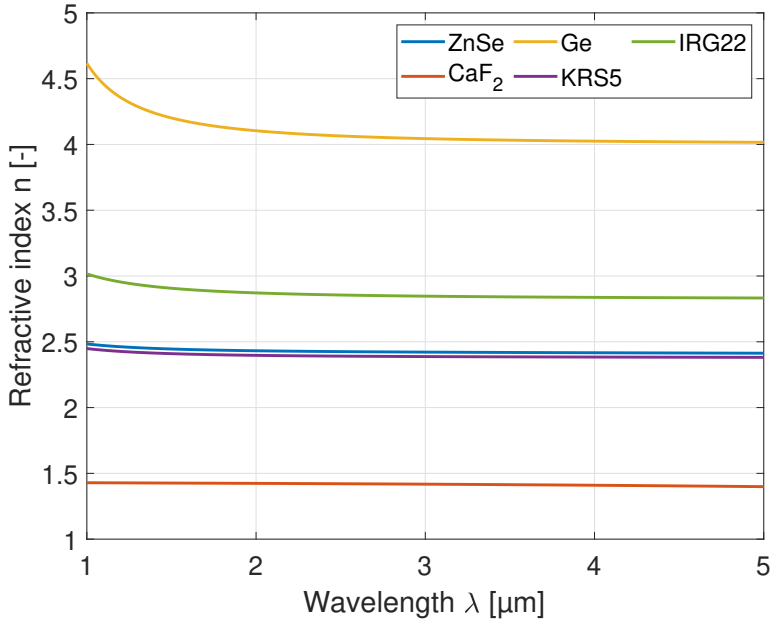

Figure 4.2: Sellmeier curves for each material described earlier.

Germanium departs from other materials by presenting a large spectral variation for the smaller wavelengths and a very high index. Calcium fluoride is the most constant and lowest index material.

	Units	ZnSe	Ge	IRG22	CaF_2	KRS5
Absorption coefficient	cm^{-1}	0.0005	0.027	0.65	0.00078	/
Average transmittance	%	70	50	95	95	72
Thermo-optic	$10^{-6}/°K$	61	396	71	-10.6	-235
Thermal expansion	$10^{-6}/°K$	7.1	6.1	12.1	18.85	58
Hardness	kg/mm^2	120	780	143	158.3	40.2

Table 4.3: Main optical properties of the different infrared materials. Data come from CRYSTRAN and [46].

4.1.3 Prisms geometry

The shape and geometrical parameters of the prisms play a preponderant role. The wedge angle and refractive index define the refraction conditions linked to the primary spurious reflections. The wedge angle defines the translation accuracy needed to tune the material thickness linked to the phase shift. The prism thickness is defined together with the refractive index to achieve the phase shift, but also determines the throughput of the setup.

4.1.3.1 Primary spurious reflection management

On a general note, the throughput is enhanced and the accuracy needed decreases if the wedge angle is small, but this angle and the air blade between the prisms need to deflect far enough the primary spurious reflection. An example of well-designed and ill-designed system according to spurious reflection is given in Figure 4.3.

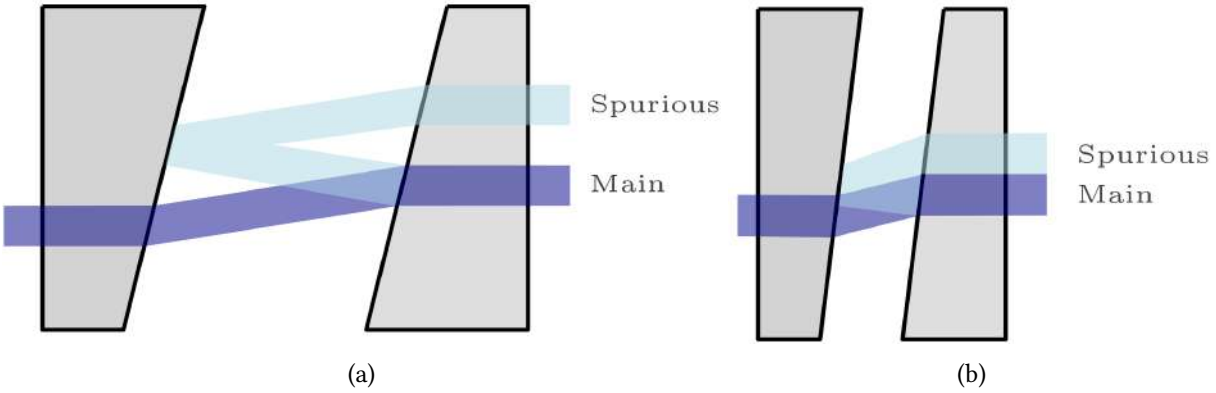

Figure 4.3: Comparison of well (a) and ill (b) designed systems according to primary spurious reflection considerations.

The considerations for the sizing of the prisms are given by several equations. First, the vertical separation between the primary spurious reflection and the main beam is given depending on the refraction angle θ_1, the wedge angle θ_{wdg} and the prism perpendicular distance w. The variables are given in the diagram of Figure 4.4. We first obtain that:

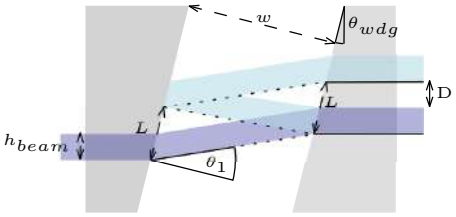

Figure 4.4: Geometry and variables for the vertical spacing determination.

$$D = L\,\cos(\theta_{wdg}) - h_{beam}, \tag{4.9}$$

where h_{beam} is the height of the beam[5]. Thanks to the Descartes law of reflection, we can rewrite:

[5]This definition applies to the current one dimension situation. For a 3D setup, h_{beam} corresponds to the diameter of the collimated beam.

$$L = w\ \tan(\theta_1) \longrightarrow D = w \tan(\theta_1)\ \cos(\theta_{wdg}) - h_{beam}. \tag{4.10}$$

The height of the beam h_{beam} corresponds in 3D to the waist of the collimated beam at the entry of the system.

The last variable to expand is the refraction angle θ_1. From the Snell-Descartes refraction law, we have that:

$$n_1\ \sin(\theta_1) = n_2\ \sin(\theta_2). \tag{4.11}$$

The situation is represented in figure 4.5. We have in this case $n_2 = n_{mat}$, $n_1 = n_{air}$, $\theta_2 = \theta_{wdg}$ and θ_1 the sought angle given by:

$$\begin{aligned} \theta_1 &= \arcsin\left(\frac{n_2}{n_1}\sin(\theta_2)\right), \\ &\approx \arcsin\left(n_{mat}\sin(\theta_{wdg})\right). \end{aligned} \tag{4.12}$$

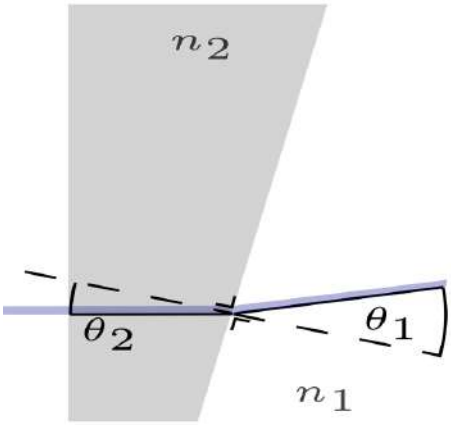

Figure 4.5: Geometry of the refraction at the prism/air interface.

Using trigonometry relations, we obtain the vertical spacing between the main beam and the primary spurious reflection:

$$\boxed{D = \frac{w}{2}\frac{n_{mat}\sin(2\,\theta_{wdg})}{\sqrt{1-\left(n_{mat}\sin(\theta_{wdg})\right)^2}} - h_{beam}}. \tag{4.13}$$

Analysing the equations above, one can conclude that the most stringent requirement concerns low refractive index materials at large wavelength.

Figures 4.6 and 4.7 show computations of the vertical spacing D when considering respectively a calcium fluoride and zinc selenide prism with refractive indices set at $n_{\mathrm{CaF_2}} = 1.42$ and $n_{\mathrm{ZnSe}} = 2.4$ and a beam height $h_{beam} = 4$ mm.

The contour maps (Fig. 4.6a and 4.7a) show the evolution of the spacing according to the wedge angle of the prism θ_{wdg} and the air blade thickness w. The lower refractive index of calcium fluoride induces a smaller region of $D > 0$ mm (the limit is represented by the red dashed line). The use of a lower refractive index material induces to define a larger wedge angle and/or air blade thickness to ensure the vertical spacing. If a vertical spacing of 10 mm is chosen, two operating lines can be defined for each material (they are drawn in green dashes on the plots). An operating point on these lines has been determined for each material:

$$\begin{aligned} &\mathrm{ZnSe} : D = 10\ \mathrm{mm} \quad &&@\ (\theta_{wdg}, w) = (12^\circ, 25\ \mathrm{mm}) \\ &\mathrm{CaF_2} : D = 10\ \mathrm{mm} \quad &&@\ (\theta_{wdg}, w) = (18^\circ, 30\ \mathrm{mm}) \end{aligned} \tag{4.14}$$

Using the Sellmeier equations (Eq. 4.8 for CAF_2 and 4.4 for ZnSe), the spectral dependence of the vertical spacing can be computed. The results are plotted in Fig. 4.6b and Fig. 4.7a respectively.

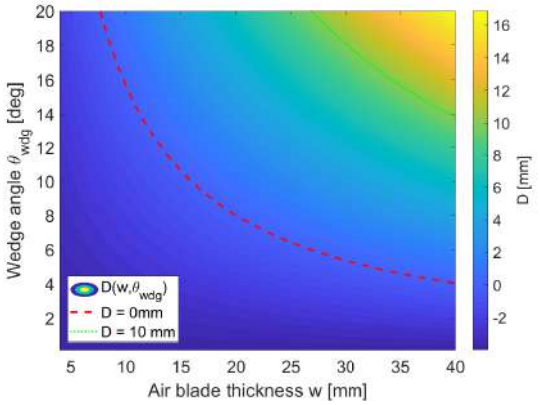

(a) Evolution according to wedge angle and air blade thickness. Red dashed line indicates exact vertical matching, green dotted line corresponds to a 1 cm spacing.

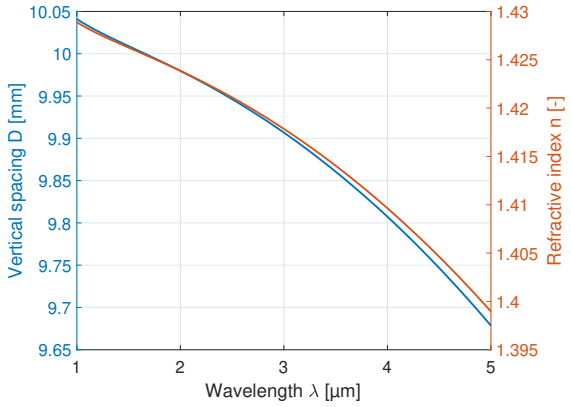

(b) Spectral dependence when operating point fixed at $(18°, 30\text{ mm})$ together with Sellmeier equation.

Figure 4.6: Computations of the vertical spacing for a CaF_2 prism.

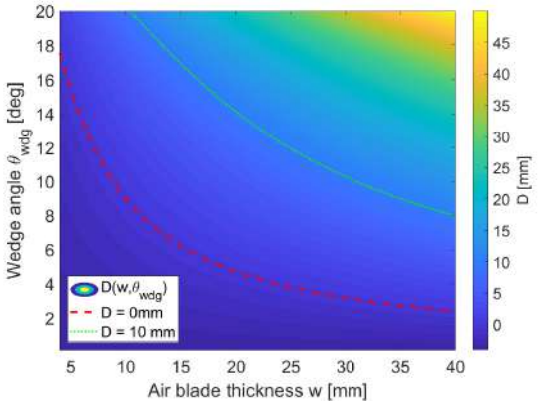

(a) Evolution according to wedge angle and air blade thickness. Red dashed line indicates exact vertical matching, green dotted line corresponds to a 1 cm spacing.

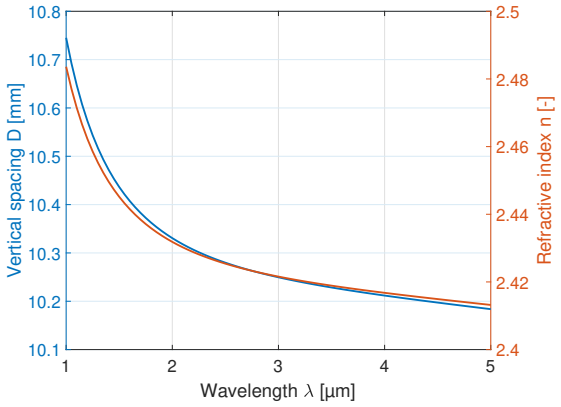

(b) Spectral dependence when operating point fixed at $(12°, 25\text{ mm})$ together with Sellmeier equation.

Figure 4.7: Computations of the vertical spacing for a ZnSe prism.

The vertical spacing spectral dependence follows the Sellmeier behaviour.

The vertical spacing computation allows concluding that the primary spurious reflection is well managed with wedge prisms. The wedge angle and perpendicular spacing between prisms depend on the refractive index, and the values are greater for a lower refractive index. This conclusion is logical as the refractive index at the prism/air interface is smaller for a smaller material index due to the Snell-Descartes law. Concerning only spurious reflection management, high refractive index materials such as germanium would be more suitable. Nonetheless, this computation only takes into account one type of material and only two prisms. Further simulations

could tackle setup with different materials and several prisms, as well as the cross-talk between arms and further order of spurious reflections. Residual cross-talk between interferometer arms could be managed by inserting absorbing media.

4.1.3.2 Throughput

The losses come from material absorption and losses at interface.

Material absorption is directly described by the absorption coefficient and transmittance.

The interface losses are given through the Fresnel coefficients[6]. They depend on the incident angle and refractive indices:

$$t_{TE} = \frac{2\, n_1\, \cos(\theta_1)}{n_1 \cos(\theta_1) + n_2 \cos(\theta_2)} \qquad \text{and} \qquad r_{TE} = \frac{n_1\, \cos(\theta_1) - n_2 \cos(\theta_2)}{n_1\, \cos(\theta_1) + n_2 \cos(\theta_2)} \tag{4.15}$$

The refractive indices refer to the material or air, depending on the situation. If the beam propagates freely and encounters a prism facet, $n_1 = n_{\text{air}}$ and $n_2 = n_{\text{mat}}$. The other way around inverts the refractive indices.

4.2 Fresnel rhombs

The second concept further investigated and finally discarded uses the Fresnel rhombs as described in Section 3.4. Such a system combines Fresnel reflection at the interface with prismatic dispersion. A common setup in double face to face configuration allows to relax the input angle tolerances and through a fine design of the interface (through a film deposit or a sub-wavelength grating) the performance can be enhanced.

4.2.1 Material considerations

As stated in Sec. 3.4, the phenomenon of total internal reflection comes with a vectorial phase shift between polarisations given by:

$$\Delta\phi_{s-p} = 2\arctan\left(\frac{\sqrt{\sin^2\theta_i - n_{ti}^2}}{n_{ti}^2 \cos\theta_i}\right) - 2\arctan\left(\frac{\sqrt{\sin^2\theta_i} - n_{ti}^2}{\cos\theta_i}\right), \tag{4.16}$$

where $n_{ti} = n_t/n_i$ and $\theta_i > \theta_{ic} = \arcsin(n_t i)$.

[6]For the sake of simplicity, TE fields have been considered here, and the discussion has not been extended according to s and p polarisations.

4.2.1.1 Linear dependence

Because of drawbacks such as sensitivity to the incident angle, Fresnel rhombs are commonly used in a double configuration. Figure 4.8 shows this configuration where two rhombs are placed symmetrically facing each other. In this setup, a variation of the angle of incidence ($-\partial\theta$) at the input of the first Fresnel rhomb is worsened at the second reflection but is inverted ($+\partial\theta$) for the two reflections in the second Fresnel rhombs. By selecting a zone of linear phase-shift dependence in the angle of incidence, the double rhombs configuration automatically compensates the phase shift variation, enlarging greatly the incidence angle tolerance of the whole setup. [35]

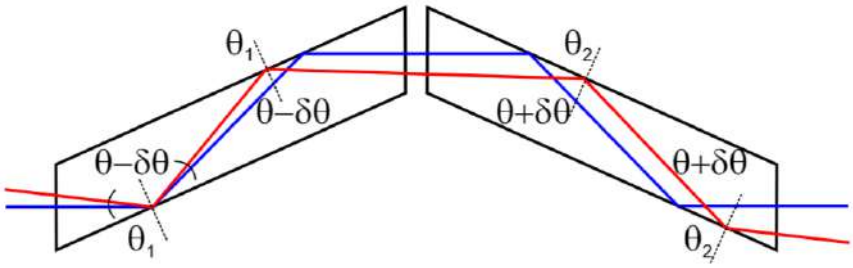

Figure 4.8: Symmetric compensation of incidence angle deviation in the double Fresnel rhombs configuration. [35]

A double reflection occurs in a single Fresnel rhomb. Therefore, in a double configuration, the light experiences four reflections and phase shifts. Each reflection induces a phase shift given by Eq. 4.16. The total phase shift from the TIR at the output is given by:

$$\Delta\phi_{\text{tot}} = 4\,\Delta\phi_{s-p}. \tag{4.17}$$

To generate a total phase shift $\Delta\phi_{\text{tot}} = 180^\circ$ we are looking for materials with a refractive index allowing a phase shift per reflection $\Delta\phi_{s-p} = \Delta\phi_{\text{tot}}/4 = 45^\circ$.

The phase shift for a material refractive index between 1 and 5 is plotted according to the angle of incidence in Fig. 4.9.

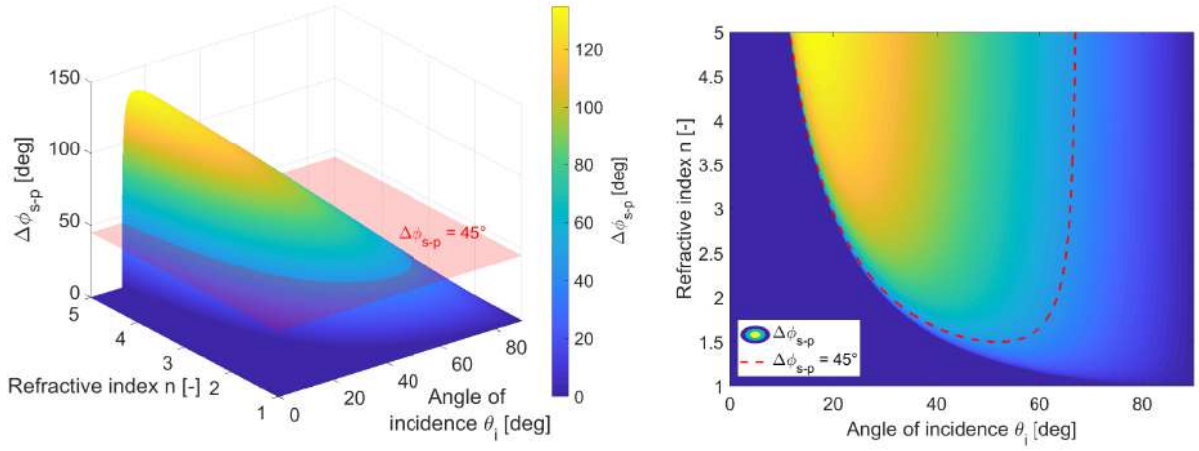

(a) (b)

Figure 4.9: Phase shift between polarisations experienced during a total internal reflection according to the angle of incidence and several material refractive indices.

The range of acceptable incidence angles is between $12°$ and $67°$ for $n = 5$. The selected material must show a refractive index above 1.47 in order to provide the $45°$ phase shift. However, one is interested in a linear dependence of the phase shift in the incident angle, as this is the key to achieve auto-compensation regarding the incidence angle tolerance. The selected material shall provide a linear $\partial(\Delta\phi)/\partial_{\theta_i}$ around $\Delta\phi = 45°$. [35]

4.2.1.2 Absorption and dispersion

This discussion is similar to the material selection performed during the previous chapter on wedged prisms. Optical properties of the main materials of interest are given in Tab. 4.3. The two selected materials are zinc selenide and chalcogenide glass. The first material, ZnSe, shows a great transmission through the whole spectral band and is widely used in infrared optics. It is thus available in large quantity, at a reasonable price, and comes with great manufacturing precision. Chalcogenide glass is a recent type of infrared glass, with a higher refractive index and almost perfect transmission properties. As a reminder, their Sellmeier equations are recalled (see Fig. 4.2, Eqs. 4.4 and 4.7 page 49):

$$\begin{aligned} n^2_{\text{ZnSe}}(\lambda) - 1 &= -0.689818 + \frac{4.855169\,\lambda^2}{\lambda^2 - 0.056359} + \frac{0.673922\,\lambda^2}{\lambda^2 - 0.056336} + \frac{2.481890\,\lambda^2}{\lambda^2 - 2222.114}, \\ n^2_{\text{IRG22}}(\lambda) - 1 &= 2.4834 + \frac{2.8203\,\lambda^2}{\lambda^2 - 0.1352} + \frac{0.9773\,\lambda^2}{\lambda^2 - 1420.7}. \end{aligned} \tag{4.18}$$

The mean values of the refractive index in the whole $1-5$ µm spectral band correspond to $\overline{n_{\text{ZnSe}}} = 2.43$ and $\overline{n_{\text{IRG22}}} = 2.86$.

The cuts in the plots of Fig. 4.9 for refractive index of ZnSe and IRG22 are shown in Fig. 4.10.

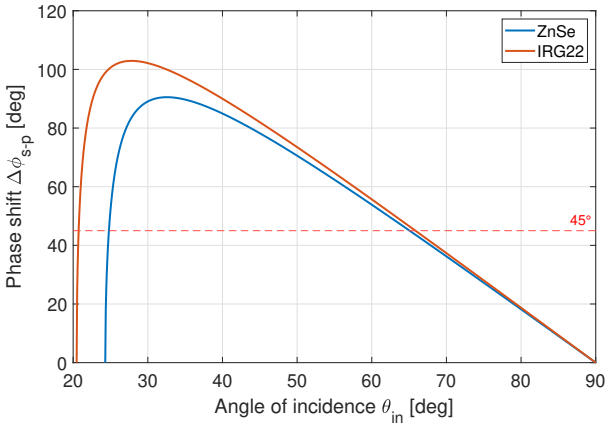

Figure 4.10: Vectorial phase shift experienced during one TIR for a prism made of ZnSe and IRG22.

The angles of incidence for which the phase shift reaches $45°$ are:

$$\theta_{\text{ZnSe}} = 65.1°; \quad \theta_{\text{IRG22}} = 65.9°.$$

As one can clearly see in Fig. 4.10, the phase shift behaviour is completely linear for those materials, consequently, the principle of auto-compensation in double configuration is satisfied.

The maximum of the extinction coefficient k from the database on the whole band is:

$$k_{\text{ZnSe}} = 5\,10^{-7} \qquad \text{and} \qquad k_{\text{IRG22}} = 10^{-6} \tag{4.19}$$

Both are directly linked to the intensity transmission of the material as for a propagation of length L at a wavelength λ we have:

$$\frac{I(L)}{I_0} = e^{-\frac{4\pi\, k\, L}{\lambda}}. \tag{4.20}$$

Defining the geometry of the rhomb would allow computing the propagation length across the material and the absorption. The worst transmission is given for the smallest wavelengths. Setting λ as the minimal length of each spectral band allows estimating the evolution of the throughput as a function of the length L.

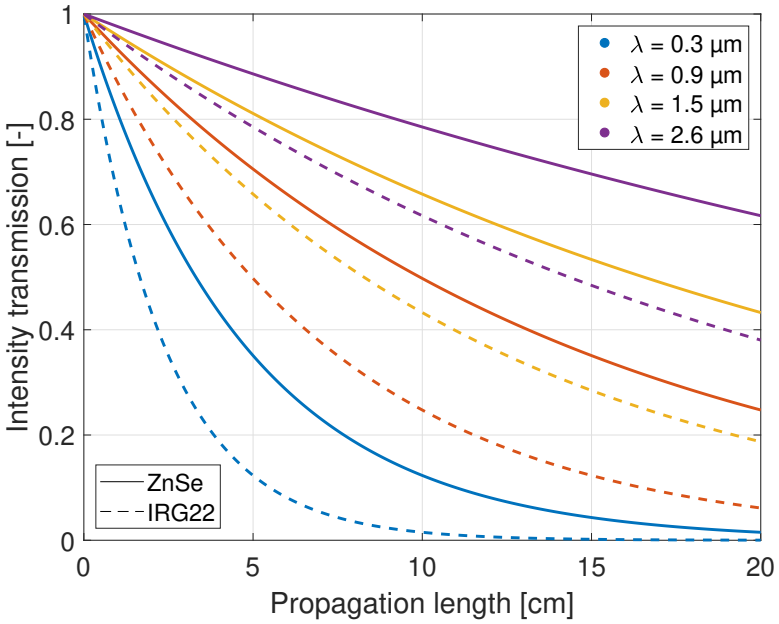

Figure 4.11: Evolution of the intensity transmission of a Fresnel rhomb in ZnSe (full) or IRG22 (dashed) according to the propagation length, for the lowest wavelength of each spectral band.

As Fig. 4.11 shows, the most stringent band considering the throughput is the lowest one. It implies a considerable limit on the total propagation length inside the prism.

To this transmission must be added the Fresnel coefficients of the four reflections (see Eq. 4.15), and the transmittance at input and output interfaces.

As those coefficients depend on the geometry, they have not been computed.

However, the throughput consideration seems to discard this concept, at least for the lower bands.

4.3 Conclusion

For the smaller missions (CubeSat 6U, [0.3 - 0.7] microns and 12U, [0.9 - 2.1] microns), both concepts, wedged prisms and Fresnel rhombs, seems unsuitable. First, they consist of a bulk optics setup. This implies collimating light from the fibre to perform the phase shift in free space propagation setup, inducing further errors and losses. Free space propagation elements also are more sensible to mechanical stability and vibrations. Moreover, the room requirement on such small platforms could directly discard both concepts, as they would be too bulky.

For larger missions, the size constraint is relaxed. Although, the greater bandwidth seems to be make the required achromaticity incompatible with light propagation through large-size elements (as the phase shift depends on the length). The achievement of achromaticity would be at the cost of either many materials and losses for the wedged prisms or complex subwavelength grating design for the Fresnel rhombs.

Chapter 5

Promising concept : integrated optics

The third and most promising concept to be more deeply investigated in this chapter relies on the integrated optics. The concept was introduced in Section 3.5. The only system prone to miniaturisation to be investigated is the compensated dispersive waveguide based on carefully designed geometry variations. The mirror approach has not been deemed mature enough yet when investigating scientific papers. Additionally, the mirror approach relies more on technological implementation rather than the design itself.

As this technology is quite recent, a description of the theoretical background is firstly needed. The derivation of the conditions of propagation, based on the Maxwell equations combined with continuity equations and boundary conditions, defines the fields propagation and system parameters.

Next, the first type of integrated optics is discussed: Hollow Metallic Waveguides (HMW). HMW confine light by metallic reflection, the waveguide consists of a tunnel with walls covered with a metallic film. Such type of integrated optics is rapidly discarded because of the stringent single mode condition.

Then, dielectric waveguides are discussed. Their equations depart partly from HMW as they rely on the refractive index difference to confine light by reflection at the interface. The solution being analytically very complicated, a graphical representation allows better understanding.

Finally, the algorithm computing the geometries of the APS will be presented. It relies on the computation of the effective refractive index. This parameter is not analytically computable, thus an external mode solver is needed. Two external mode solvers are implemented and compared.

5.1 Theoretical approach

Radiation such as light is described in the wave approach as a combination of an electric and a magnetic field. Both fields are pulsating waves depending on the three spatial coordinates and time. Such physical quantities are conveniently described by phasors which introduce complex numbers. The instantaneous electric and magnetic fields E and H described in phasors take the following form:

$$E(x,y,z,t) = \underline{\hat{E}}(x,y,z,t)\, e^{j\omega t} \qquad \text{and} \qquad H(x,y,z,t) = \underline{\hat{H}}(x,y,z,t)\, e^{j\omega t}. \tag{5.1}$$

ω represents the pulsation of the field, linked to the frequency ν by:

$$\omega = 2\pi\nu. \tag{5.2}$$

The $\hat{}$ notation in Eq. 5.1 stands to highlight time-independent quantities. The real electromagnetic field is obtained by taking the real part of the phasor. Assuming harmonic propagation in the z-direction[1], we can rewrite the electric field phasor:

$$E(x,y,z,t) = \mathbb{R}\left\{\underline{\hat{E}}(x,y,z)\, e^{j\omega t}\right\} = \mathbb{R}\left\{\underline{\hat{E}}^{0}(x,y)\, e^{j\omega t - \gamma z}\right\}. \tag{5.3}$$

The notation ^{0} now implies that the corresponding quantity is z-independent. γ is the propagation constant given by:

$$\gamma = \alpha + j\beta, \tag{5.4}$$

where α represents the loss and β the propagating part. This is highlighted by developing the z exponential:

$$A\, e^{-\gamma z}\, e^{j\omega t} = A\, e^{-(\alpha+j\beta)z}\, e^{j\omega t} = A\, \underbrace{e^{-\alpha z}}_{i}\, \underbrace{e^{j(\beta z - \omega t)}}_{ii}. \tag{5.5}$$

As one can see, α directly implies an exponential decrease of the wave amplitude (*i*), while β corresponds to the propagation of the wave in the imaginary exponential together with the time behaviour (*ii*).

Assuming harmonic propagation, using phasors allows substituting the partial derivatives by:

$$\begin{array}{rcl} \partial_t & \longrightarrow & j\omega, \\ \partial_z & \longrightarrow & -\gamma. \end{array} \tag{5.6}$$

Thanks to the separation of variables, we can obtain from the wave equation a time-independent form, known as the Helmholtz equation. Introducing the electric and magnetic phasors, we obtain:

$$\begin{cases} \nabla^2 \underline{\hat{E}} + k^2 \underline{\hat{E}} = 0 \\ \nabla^2 \underline{\hat{H}} + k^2 \underline{\hat{H}} = 0 \end{cases}, \tag{5.7}$$

where k is the wavenumber of the medium, given by the wave pulsation ω, the material permittivity ε and permeability μ by:

[1] This implies that the cross-section of the waveguide is constant along the propagation.

$$k = \frac{2\pi}{\lambda} = \omega\sqrt{\mu\,\varepsilon}. \tag{5.8}$$

As in this case, the waves propagate in the z-direction, we can separate the z-part of the Laplacian operator from the transverse part. For example in Cartesian coordinates[2]:

$$\nabla^2\underline{\hat{E}} = \left(\nabla_\perp^2 + \nabla_z^2\right)\underline{\hat{E}} = \left(\nabla_{xy}^2 + \nabla_z^2\right)\underline{\hat{E}} = \left(\nabla_\perp^2 + \gamma^2\right)\underline{\hat{E}}, \tag{5.9}$$

where the last equality comes from the formal substitution thanks to phasors properties (Eq. 5.6). Substituted in Eq. 5.7 we obtain for the electric field:

$$\nabla_{xy}^2\underline{\hat{E}} + (\gamma^2 + k^2)\underline{\hat{E}} = 0. \tag{5.10}$$

As we assumed harmonic propagation in z, rewriting the phasor as in Eq. 5.3 before multiplying by $e^{\gamma z}$ gives:

$$\nabla_{xy}^2\underline{\hat{E}}^0 + h^2\underline{\hat{E}}^0 = 0, \tag{5.11}$$

where we introduce the eigenvalue $h^2 = k^2 + \gamma^2$. The derivations are held similarly for the magnetic field, resulting in:

$$\nabla_{xy}^2\underline{\hat{H}}^0 + h^2\underline{\hat{H}}^0 = 0. \tag{5.12}$$

The electromagnetic field is therefore described by two vector equations 5.11 and 5.12 in terms of phasors. Those two equations correspond to six second-order differential equations. Transverse geometry and boundary conditions are needed to solve these unknown variables. Hopefully, the six vector components are inter-dependent through Maxwell equations. The curl equations in the source-free case allow expressing the four transverse field components as functions of the z components. By taking advantage of:

$$\nabla \wedge \hat{E} = -j\omega\mu\hat{H} \qquad \text{and} \qquad \nabla \wedge \hat{H} = j\omega\varepsilon\hat{H}, \tag{5.13}$$

we can finally rewrite:

$$\boxed{\begin{array}{ll} \hat{H}_x^0 = -h^{-2}\left(\gamma\,\partial_x\hat{H}_z^0 - j\omega\varepsilon\,\partial_y\hat{E}_z^0\right) & \hat{E}_x^0 = -h^{-2}\left(\gamma\,\partial_x\hat{E}_z^0 + j\omega\mu\,\partial_y\hat{H}_z^0\right) \\ \hat{H}_y^0 = -h^{-2}\left(\gamma\,\partial_y\hat{H}_z^0 + j\omega\varepsilon\,\partial_x\hat{E}_z^0\right) & \hat{E}_y^0 = -h^{-2}\left(\gamma\,\partial_y\hat{E}_z^0 - j\omega\mu\,\partial_x\hat{H}_z^0\right) \end{array}}. \tag{5.14}$$

The waves can be divided into three groups according to the z components of the electric and magnetic fields:

[2]This substitution $\nabla_\perp^2 = \nabla_{xy}^2$ is arbitrary and only relies on the rectangular geometry presented here. One could choose cylindrical coordinates and obtain $\nabla_\perp^2 = \frac{1}{r}\partial_r\left(r\partial_r\right) + \frac{1}{r^2}\partial_{\phi\phi}^2$ before pursuing the derivations.

1. **Transverse ElectroMagnetic (TEM) waves**: $E_z = H_z = 0$. There is no field component in the z direction. A plane electromagnetic wave belongs to this group, with only transverse field components;
2. **Transverse Electric (TE) waves**: $E_z = 0$. Only the magnetic field shows a z component;
3. **Transverse Magnetic (TM) waves**: $H_z = 0$. Only the electric field shows a z component.

5.2 Hollow Metallic Waveguides

The first one to be presented is inspired by radio communications. This concept relies on metallic reflections to confine the light. They provide a closed volume filled with air or vacuum and delimited by walls made of metal or coated with a metal film. Light is then confined inside the volume by reflection upon the boundaries of the volume. These waveguides are called Hollow Metallic Waveguides (HMW). Figure 5.1 represents such a waveguide with a rectangular section.

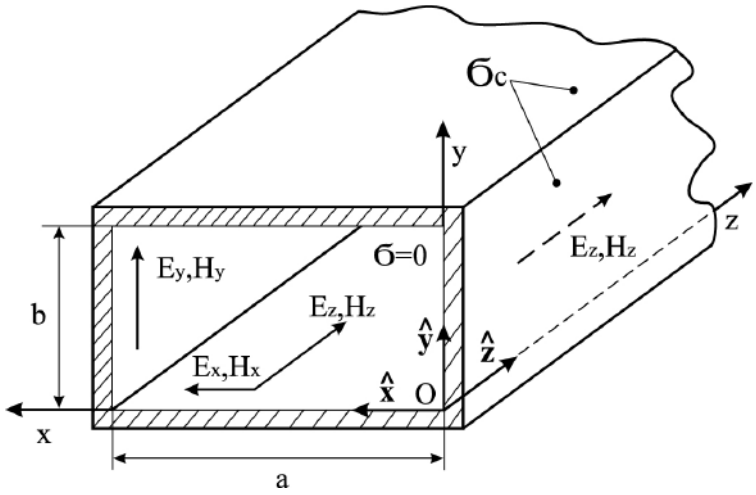

Figure 5.1: Schematic representation of HMW. A metal (usually gold) on the boundaries of the waveguide confines by reflection the light inside the central volume filled with air. [47]

HMW have been thoroughly studied, for example, by Pr. Labadie during his PhD thesis and afterwards [48, 40, 39, 41].

5.2.1 Modal behaviour

5.2.1.1 Transverse Magnetic

TM waves imply $H_z = 0$. E_z is found by setting the boundary condition $E_z = 0$ on the wall. By the method of separation of variables, we can define two functions $\Phi(x)\Psi(y)$ such that

$E_z(x,y) = \Phi(x)\Psi(y)$. Introducing this in Eq. 5.11 yields the following solution[3]:

$$E_z(x,y) = C \sin\left(\frac{m\pi x}{a}\right) \sin\left(\frac{n\pi y}{b}\right) = C \sin(Ax) \sin(By)\,, \tag{5.15}$$

where $A = m\pi/a$, $B = n\pi/b$ and $h^2 = A^2 + B^2$. m and n are integers for which the equation is satisfied. The (m,n) values will define several modes able to propagate in the waveguide. This solution is obtained by assuming a perfect medium: $\gamma = j\beta$.

Inserting the H_z and E_z fields in the transverse expression of the fields (see Eq. 5.14) reads:

$$\begin{cases} E_x &= \dfrac{-j\beta}{h^2} C\ A \cos(Ax)\ \sin(By)\,, \\ E_y &= \dfrac{-j\beta}{h^2} C\ B \sin(Ax)\ \cos(By)\,, \\ H_x &= \dfrac{j\omega\varepsilon}{h^2} C\ B \sin(Ax)\ \cos(By)\,, \\ H_y &= \dfrac{-j\omega\varepsilon}{h^2} C\ A \cos(Ax)\ \sin(By)\,. \end{cases} . \tag{5.16}$$

From Eq. 5.15, if either m or n equals 0, the product of sinus results in $E_z = 0$, which is contradictory with the initial hypothesis of TM waves for which only $H_z = 0$. Therefore, the TM propagating mode of the lowest order is for $(m,n) = (1,1)$, which is noted as TM_{11}.

5.2.1.2 Transverse Electric

TE waves indicate that $E_z = 0$. The same mathematical development holds and gives the following z magnetic field:

$$H_z = C\ \cos(Ax)\ \cos(Ay)\,. \tag{5.17}$$

Introduced in the transverse fields expression, we obtain:

$$\begin{cases} E_x &= \dfrac{j\omega\mu}{h^2} C\ B \cos(Ax)\ \sin(By)\,, \\ E_y &= \dfrac{-j\omega\mu}{h^2} C\ A \sin(Ax)\ \cos(By)\,, \\ H_x &= \dfrac{j\beta}{h^2} C\ A \sin(Ax)\ \cos(By)\,, \\ H_y &= \dfrac{j\beta}{h^2} C\ B \cos(Ax)\ \sin(By)\,. \end{cases} . \tag{5.18}$$

[3]The notations are from now on simplified for the sake of clarity, but as the expressions indicate, these quantities are time-independent and show harmonic propagation in z.

On the other hand, Eq. 5.17 gives a product of cosines. This implies that it is possible to have either m or n equal to 0[4]. The TE propagating mode of lowest order is then with $(m, n) = (1, 0)$ and is written TE_{01}[5].

5.2.2 Cut-off wavelength

The Helmholtz equations combined with the boundary conditions and the waveguide geometry give rise to a condition on the light parameters to obtain propagation.

We had previously shown that the eigenvalue h of the Helmholtz equation was given by (see Eq. 5.7 to 5.11):

$$h^2 = k^2 + \gamma^2, \tag{5.19}$$

where $k = \omega\sqrt{\mu\varepsilon}$ is the wavenumber of the medium and $\gamma = \alpha + j\beta$ the propagation constant. From the modal behaviour of the solutions, we obtained when resolving the differential equation that $h^2 = A^2 + B^2$ (see Eq. 5.15). Isolating the propagation constant and developing the terms leads to:

$$\gamma = \sqrt{h^2 - k^2} = \sqrt{A^2 + B^2 - k^2} = \sqrt{\left(\frac{m\pi}{a}\right)^2 + \left(\frac{n\pi}{b}\right)^2 - \omega^2\mu_0\varepsilon_0}. \tag{5.20}$$

A mode is excited as soon as this propagation constant is purely imaginary[6]. This provides a direct condition of propagation of the pulsation, called the cut-off pulsation:

$$\omega_c = \frac{1}{\sqrt{\mu_0\varepsilon_0}}\sqrt{\left(\frac{m\pi}{a}\right)^2 + \left(\frac{n\pi}{b}\right)^2}. \tag{5.21}$$

Propagation will occur only when $\omega > \omega_c$. It is more practical to define the cut-off wavelength to compare with waveguide dimensions:

$$\lambda_c = \frac{2}{\sqrt{\left(\frac{m}{a}\right)^2 + \left(\frac{n}{b}\right)^2}}. \tag{5.22}$$

In this case, due to the inverse relation between wavelength and pulsation, propagation occurs for $\lambda < \lambda_c$.

[4]But not both at the same time, as this results in all three field components cancelling out: there is simply no propagating wave in the waveguide.

[5]This is in the case of $a > b$ as shown in the schematic representation of Fig. 5.1. If $b > a$, then the lowest order mode is TE_{01}.

[6]If not, the real part induces an exponential decrease of the amplitude, leading to the extinction of the wave.

5.2.3 Single mode behaviour

As stated in Sec. 3.5, one of the main advantages of the integrated optics is the single mode propagation exerting spatial filtering on the collected field.

Starting from (too) great wavelengths and decreasing, one will go from no propagation to single mode propagation, when the highest cut-off wavelength will be reached. For any geometry, the mode with the highest cut-off wavelength is TE_{10}, called the fundamental mode. Its cut-off wavelength is given by replacing $(m, n) = (1, 0)$ in Eq. 5.22:

$$\lambda_c^{01} = 2a. \tag{5.23}$$

However, the second largest cut-off wavelength is not the same for any geometry. If $b < a/2$, the second excited mode is TE_{20}. For other geometries, it is the TE_{20}. These information are summarised in Tab. 5.1.

$b \leqslant a/2$	$b > a/2$
$a < \lambda < 2a$	$2b < \lambda < 2a$

Table 5.1: Single mode range for a rectangular HMW. These conditions are obtained with the initial definition that $b < a$. [39]

5.2.4 Limitations of the Hollow Metallic Waveguides

This single mode condition is the first and foremost constraint that the integrated APS must fulfil. Reporting conditions of Tab. 5.1 with the wavelengths considered in this work allow defining the constraints on the geometry of the waveguide. The resulting restricting geometry of the waveguide is reported in Tab. 5.2.

Spectral band [µm]	Central wavelength [µm]	$b \leqslant a/2$ b_{max} [µm]	$b > a/2$ a_{max} [µm]
$[0.3 - 0.7]$	0.5	0.15	0.3
$[0.9 - 2.1]$	1.5	0.45	0.9
$[1.5 - 3.5]$	2.5	0.75	1.5
$[2.6 - 6.4]$	4.5	1.3	2.6

Table 5.2: Constraints on the geometry for single mode propagation in a HMW with $a > b$ according to the different spectral bands of interest of this work.

The restriction on the dimensions of the waveguide shown in Tab. 5.2 is way too stringent. Even if today technology is theoretically able to produce waveguides with such dimensions, the complexity is too high.

5.3 Dielectric waveguide

In contrast to the HMW, the dielectric waveguide do not confine light by reflection. It relies on the refractive index profile of the waveguide. Several profiles exist, from step-index to graded-index profile. The graded-index profiles can be quite different, with a peculiar application to each sort of profile.

5.3.1 Geometrical approach

The first approach to tackle dielectric waveguides is to assume that the wavelength of the radiation is negligible compared to the dimensions of the waveguide. This allows describing the propagation of light in terms of rays.

A two-dimensional step-index waveguide is represented in Fig. 5.2. The geometric description is based on the following assumptions:

- λ is negligible compared to (a, b);
- The core and cladding are homogeneous dielectrics;
- We have a translation symmetry along the z-axis;
- The medium is lossless.

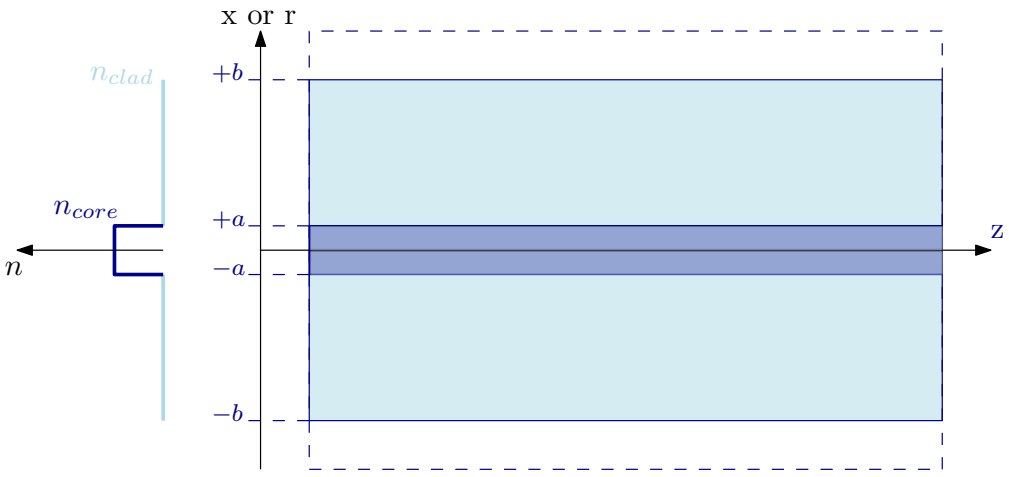

Figure 5.2: Geometric description of a two-dimensional slab step-index waveguide. The cladding has a width of $2b$ and is in light blue, while the core is $2a$ high and represented in dark blue. The refractive indices follow $n_{\text{core}} > n_{\text{clad}}$.

The geometrical approach relies on the same development as done earlier concerning the Total Internal Reflection phenomenon in Sec. 3.4. Figure 5.3 gives a reminder of the situation.

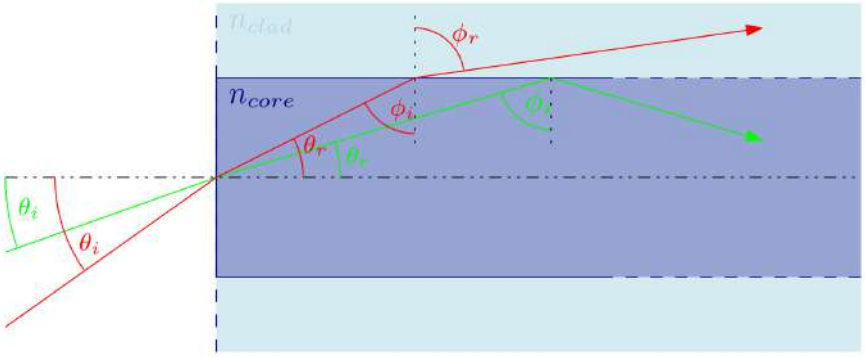

Figure 5.3: Representation of the light confinement condition in the geometrical approach. Red ray is guided while green ray is unguided.

Considering external medium to be air or vacuum, with refractive index $n_0 = 1$, we have the refracted angle inside the waveguide given by Snell-Descartes law[7]:

$$n_0 \sin(\theta_i) = n_{co} \sin(\theta_r). \tag{5.24}$$

The ray is guided only if its angle of refraction at its first encounter with the core cladding interface is higher than $\pi/2$, trespassing the mathematical limit of the sine and leading to total reflection. The ray is guided only if the incidence angle ϕ_i on the core cladding interface is greater than the critical incidence angle ϕ_c. For example in the scheme of Fig. 5.3, the red ray does not fulfil this condition, a refractive angle exists and the ray is unguided.

Therefore the propagation condition can be written:

$$\phi_i > \phi_{ic}. \tag{5.25}$$

As ϕ_i and θ_r are angles of a rectangular triangle, they are linked by $\phi_i = \pi/2 - \theta_r$. Therefore, using this relation and the Snell law, one can define the maximum incident angle of the ray such that the ray is guided:

$$\left.\begin{aligned} \theta_{rc} &= \pi/2 - \phi_{ic} \\ n_0 \sin(\theta_{ic}) &= n_{co} \sin(\theta_{rc}) \end{aligned}\right\} \qquad \theta_{ic} = n_1 \cos(\phi_{ic}). \tag{5.26}$$

And the Snell law for the core cladding interface, with $\phi_{rc} = \pi/2$ by definition, gives:

$$n_{co} \sin(\phi_{ic}) = n_{cl} \sin(\phi_{rc}) = n_{cl} \longrightarrow \sin(\phi_{ic}) = n_{cl}/n_{co} \tag{5.27}$$

This concludes that the ray is guided only for $\phi > \phi_{ic}$ and this corresponds to a condition on the incident angle that defines the Numerical Aperture (NA) of the waveguide:

[7]From now one, the core and cladding refractive indices will be defined by respectively n_{co} and n_{cl}.

$$\boxed{\theta \leqslant \theta_{ic} = \sqrt{n_{co}^2 - n_{cl}^2}}. \tag{5.28}$$

The NA is linked with the half angle of the acceptance cone of the waveguide. It is a dimensionless quantity that describes the angular tolerance of a waveguide for propagation. However, when the core dimensions approach the wavelength, the geometrical approach is not accurate anymore. Moreover, it only takes into account (x, z) planar rays, and not skew rays, for example.

5.3.2 Electromagnetic description

The electromagnetic description of dielectric waveguides relies on the same equations and development as previously presented for the HMW. However, as the HMW presented metallic walls and confined light by reflection, now the light is confined by the refractive index difference, and the light is completely able to propagate in the cladding.

Equation 5.11 still holds, and reads in one dimension[8]:

$$\frac{d^2 E_y}{dx^2} + h^2 E_y = 0, \tag{5.29}$$

where $h^2 = k_0^2 n_i^2 - \beta^2$. Because of continuity conditions, the solution is for the symmetric case:

$$E_y(x) = \begin{cases} A\,\cos(\sigma x) & \text{for } |x| \leqslant a \\ A\,\cos(\sigma x)\, e^{-\xi(|x|-a)} & \text{for } |x| > a \end{cases}, \tag{5.30}$$

where $\sigma = k_0 n_{co}^2 - \beta^2$ and $\xi^2 = \beta^2 - k_0^2 n_{cl}^2$. To satisfy the continuity conditions, we need $\sigma > 0$ and to have a guided mode, the part in the cladding must decay ($\xi^2 > 0$), leading to the condition $\beta > n_{cl} k_0$. Therefore, a guided mode satisfies[9]:

$$n_{co} k_0 > \beta > n_{cl} k_0. \tag{5.31}$$

The solutions for which ξ imaginary correspond to leaky modes. The magnetic field is given by:

$$H_z(x) = \frac{j}{\omega\mu_0}\frac{dE_y}{dx} \longrightarrow \begin{cases} -\dfrac{j\sigma}{\omega\mu_0} A \sin(\sigma x) & \text{for } |x| \leqslant a \\ \mp\dfrac{j\xi}{\omega\mu_0} A \cos(\sigma x)\, e^{-\xi(|x|-a)} & \text{for } \begin{matrix} x > a \\ x < -a \end{matrix} \end{cases}. \tag{5.32}$$

And the continuity condition at $|x| = a$ gives:

$$\frac{j\sigma}{\omega\mu_0} A\,\sin(\sigma a) = \frac{j\xi}{\omega\mu_0} A\,\cos(\sigma a) \Longleftrightarrow \tan(\sigma a) = \frac{\xi a}{\sigma a}. \tag{5.33}$$

[8] This discussion concerns TE waves.

[9] This is as well the mathematical that to have light confinement and propagation, we need $n_{co} > n_{cl}$.

Introducing normalised quantities defined as:

$$u := \sigma a = a\sqrt{k_0 n_1^2 - \beta^2} \qquad \text{and} \qquad V^2 := a^2(\xi^2 + \sigma^2) = a^2 k_0 2(n_1^2 - n_2^2), \tag{5.34}$$

we can rewrite the continuity condition as:

$$\boxed{\tan(u) = \frac{\sqrt{V^2 - u^2}}{u}}. \tag{5.35}$$

The parameter V is called the normalised frequency of the waveguide. This eigenvalue equation gives a set of discrete solutions. Given the parameters of the system (wavelength, dimensions, index profile), there is only a limited number of σ values satisfying this equation. Therefore, there are only limited values of β as well, each corresponding to a guided mode. The discussion so far holds for symmetric TE modes only. However, for the other modes, even if it uses different expressions and conditions, the conclusion is similar. For example, the anti-symmetric TE mode is given by $E_y = A\,\sin(\sigma x)$, leading to the eigenvalue equation $\tan(u) = -u/\sqrt{V^2 - u^2}$. The resolution of the eigenvalue equation is represented graphically in Fig. 5.4 for several values of normalised frequency.

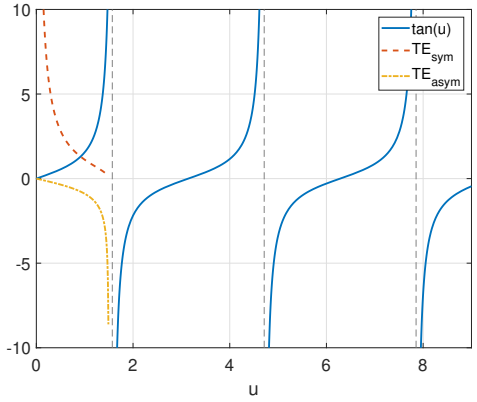

(a) V = 1.5: 1 TE_{sym}, 0 TE_{asym}.

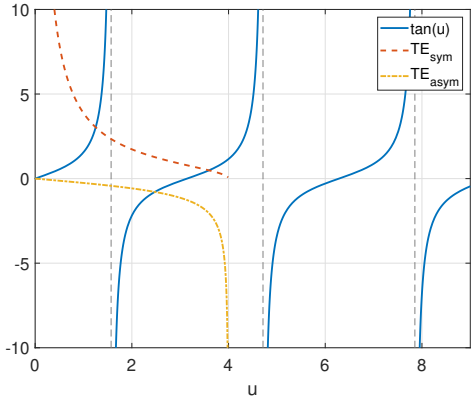

(b) V = 4: 2 TE_{sym}, 1 TE_{asym}.

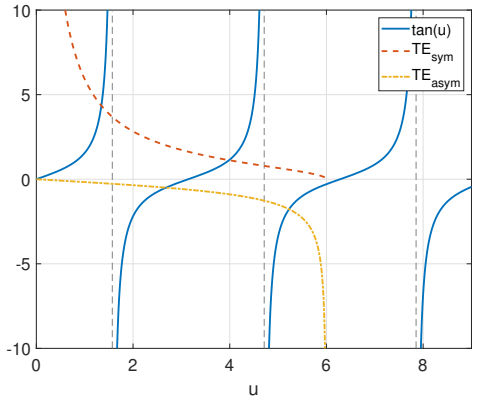

(c) V = 6: 2 TE_{sym}, 2 TE_{asym}.

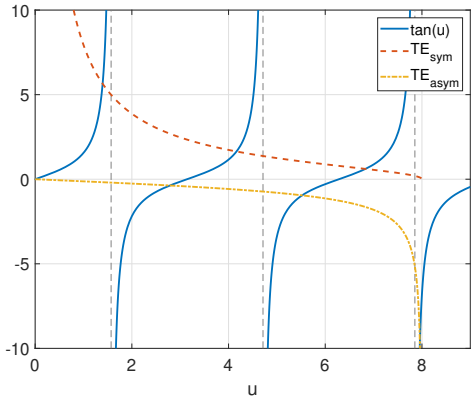

(d) V = 8: 3 TE_{sym}, 3 TE_{asym}.

Figure 5.4: Graphical representation of the eigenmode equation for guided modes in a dielectric waveguide for several normalised frequencies.

The modes arise when two curves cross each other. As one can see, as soon as $V < \pi/2$, the waveguide exhibits single mode propagation (case of Fig. 5.4a).

This discussion holds for a simple one dimensional waveguide (slab waveguide). For rectangular waveguides, as soon as two dimensions are involved, numerical computation is needed to solve the modes.

5.3.3 Effective refractive index

The interest of dielectric waveguides as phase shifters resides in the concept of effective refractive index. The effective index is the refractive index that the mode actually experiences during propagation. It depends on the parameters of the system (waveguide and source of light). For example, if the mode has a large overlapping with the cladding, the effective index will be close to n_{clad}. The inverse is true as well: a tightly confined mode will have n_{eff} close to n_{core}. Therefore, a careful design of the waveguide materials and geometry allows tuning of the refractive index.

Moreover, the main advantage is that as the effective index relies on the geometry as well, we can achieve a waveguide with varying effective index build in the same material.

5.3.4 Rectangular waveguide

The rectangular waveguide consists in the extension to two dimensions of the slab waveguide used earlier to determine the propagation equations. It can be implemented in different ways. Some of them are shown in Fig. 5.2.

(a) Buried. (b) Ridge. (c) Rib.

Figure 5.5: Representation of the cross-section of different step index homogeneous rectangular dielectric waveguides.

The Maxwell equations are not analytically solvable for the rectangular waveguide because of the transverse confinement in both directions. Therefore, one has to rely on a numerical solution.

5.3.5 Algorithm

The phase shift experienced by the field during propagation in a dielectric medium of refractive index n and length L is given by the well-known formula:

$$\Delta\phi(\lambda) = \frac{2\pi}{\lambda} nL. \tag{5.36}$$

In the case of rectangular waveguide, the refractive index is given by the effective index of the system. However, this effective index yields the same chromatism as usual material indexes. One has to rely on a waveguide divided into segments with different geometries to achieve refractive indexes that counteract each other. For N segments, the phase shift becomes for arm j:

$$\Delta\phi_j(\lambda) = \frac{2\pi}{\lambda} \sum_{i}^{N} n_{\text{eff},i,j} L_{ij}. \tag{5.37}$$

The objective in the case of an integrated APS made of rectangular waveguides is to realise a differential achromatic phase shift of π. This implies that both arms will experience a phase shift, the π phase shift resulting from the phase difference between both arms for each wavelength. Defining for the sake of simplicity that each arm has the same number of segments N, and that each segment has the same length $L_{ij} = L_i$, the phase shift is directly given by the difference in effective index between each segment:

$$\Delta\phi_{\text{tot}}(\lambda) = \Delta\phi_A - \Delta\phi_B = \frac{2\pi}{\lambda}\sum_i^N \Delta n_{\text{eff},i} L_i. \tag{5.38}$$

The idea to compute the best waveguide geometry for each segment resides in the expansion of the effective index of both arms A and B into a polynomial fit:

$$\begin{cases} n_{\text{eff},Ai} = A_{Ai} + B_{Ai}\lambda + C_{Ai}\lambda^2 & i = 1,..,N \\ n_{\text{eff},Bi} = A_{Bi} + B_{Bi}\lambda + C_{Bi}\lambda^2 & i = 1,..,N \end{cases}. \tag{5.39}$$

This allows rewriting the effective index difference used in Eq. 5.38 as:

$$\begin{aligned} \Delta n_{\text{eff},i} &= (A_{Ai} - A_{Bi}) + (B_{Ai} - B_{Bi})\,\lambda + (C_{Ai} - C_{Bi})\,\lambda^2, \\ &= \overline{A_i} + \overline{B_i}\lambda + \overline{C_i}\lambda^2. \end{aligned} \tag{5.40}$$

Inserting this polynomial fit of the effective index difference in the differential phase shift yields:

$$\Delta\phi_{\text{tot}}(\lambda) = \frac{2\pi}{\lambda}\sum_i^N \left(\overline{A_i} + \overline{B_i}\lambda + \overline{C_i}\lambda^2\right) L_i. \tag{5.41}$$

The spectral dependence of the phase shift is given by its derivative with respect to λ:

$$\frac{\partial}{\partial\lambda}(\Delta\phi_{\text{tot}}) = -\frac{2\pi}{\lambda}\sum_i^N \left(\frac{\overline{A_i}}{\lambda} - \overline{C_i}\lambda\right) L_i. \tag{5.42}$$

Equations 5.41 and 5.42 combined form a system of equations describing the phase shift and its spectral dependence:

$$\forall\lambda \quad : \quad \begin{cases} \Delta\phi &= \Delta\phi_0 \\ \dfrac{\partial\Delta\phi}{\partial\lambda} &= 0 \end{cases} \iff \begin{cases} \displaystyle\sum_i^N \overline{A_i} L_i &= 0, \\ \displaystyle\sum_i^N \overline{B_i} L_i &= \dfrac{\Delta\phi_0}{2\pi}, \\ \displaystyle\sum_i^N \overline{C_i} L_i &= 0. \end{cases} \tag{5.43}$$

As soon as we consider three segments, the system becomes a three-equation system linking polynomial coefficients and segments length. The system, written with matrices, reads:

$$\underbrace{\begin{bmatrix} \overline{A_1} & \overline{A_2} & \overline{A_3} \\ \overline{B_1} & \overline{B_2} & \overline{B_3} \\ \overline{C_1} & \overline{C_2} & \overline{C_3} \end{bmatrix}}_{\mathcal{M}} \cdot \underbrace{\begin{bmatrix} L_1 \\ L_2 \\ L_3 \end{bmatrix}}_{\mathcal{L}} = \underbrace{\begin{bmatrix} 0 \\ \Delta\phi_0/2\pi \\ 0 \end{bmatrix}}_{\mathcal{T}}. \tag{5.44}$$

By defining M and L matrices as the left-hand-side terms of the equation, the solution providing the lengths of the segments is given by:

$$\mathcal{L} = \mathcal{M}^{-1} \cdot \mathcal{T}. \tag{5.45}$$

The algorithm therefore consists in the following steps:

1. Input: Spectral range $[\lambda_{\text{min}}, \lambda_{\text{max}}]$, widths range $[a_{\text{min}}, a_{\text{max}}]$ and height b;
2. Compute n_{eff} for each width a;
3. Compute Δn_{eff} for all couples $[a_1, a_2]$;
4. Interpolate the polynomial fit $\Delta n_{\text{eff}} = \overline{A} + \overline{B}\lambda + \overline{C}\lambda^2$;
5. Solve the matrix system from Eq. 5.45;
6.
   - If $L_{tot}^{new} = \sum_i^N \mathcal{L}(i) < L_{tot}^{prev}$: save the parameters and evaluate performances.
   - If not, iterate with other widths.

The phase shift is then computed for all wavelengths in the spectral band. Several performance parameter can be extracted, such as the maximum error ε_{max}, or the total length L_{tot}.

Many APS have been computed. Taking a range of widths between 3 µm and 15µm with a step of 1µm, for wavelengths in each spectral band separated by 0.01 µm, the effective index difference has been computed for each possibility of segments. However, to perform such an optimisation algorithm, the effective index of the rectangular waveguide has to be numerically computed.

5.3.6 Mode solver for dielectric rectangular waveguide

Writing a numerical solver for three dimensional propagation in a rectangular waveguide is a task of its own. Therefore, already implemented solvers will be computing the effective index. Two main solvers have been successfully implemented in the algorithm presented earlier. The first is based on an extended Marcatili's approach, while the second relies on full- and semi-vectorial eigenmode computation and scalar method. [49, 50] Let us remind that the main goal here is to compute the effective index. In this case, one is not interested in the mode intensity profiles and phase variation.

The modal behaviour could have been analytically described by following [51], however, this reference was not freely accessible. No other reference was found describing an analytical approach to the two dimensional dielectric rectangular waveguide. Consequently, the modal behaviour will be let for further simulations once the phase shift has been simulated.

5.3.6.1 Extended Marcatili's approach

This approach aims at providing an approximate analytical solution to the analytically unsolvable equations for a dielectric rectangular waveguide. The Marcatili's approach is based on an *ansatz*: the resolution of the modal fields is based on a separation of variable in the waveguide core. Moreover, the waveguide is divided into nine subsections. The corner regions are considered negligible in terms of electromagnetic intensity compared to the others: four out of the five regions are ignored, as are the matching conditions of the fields along their boundaries. The regions of interest are shown in Fig. 5.6, where the ignored regions are hatched.

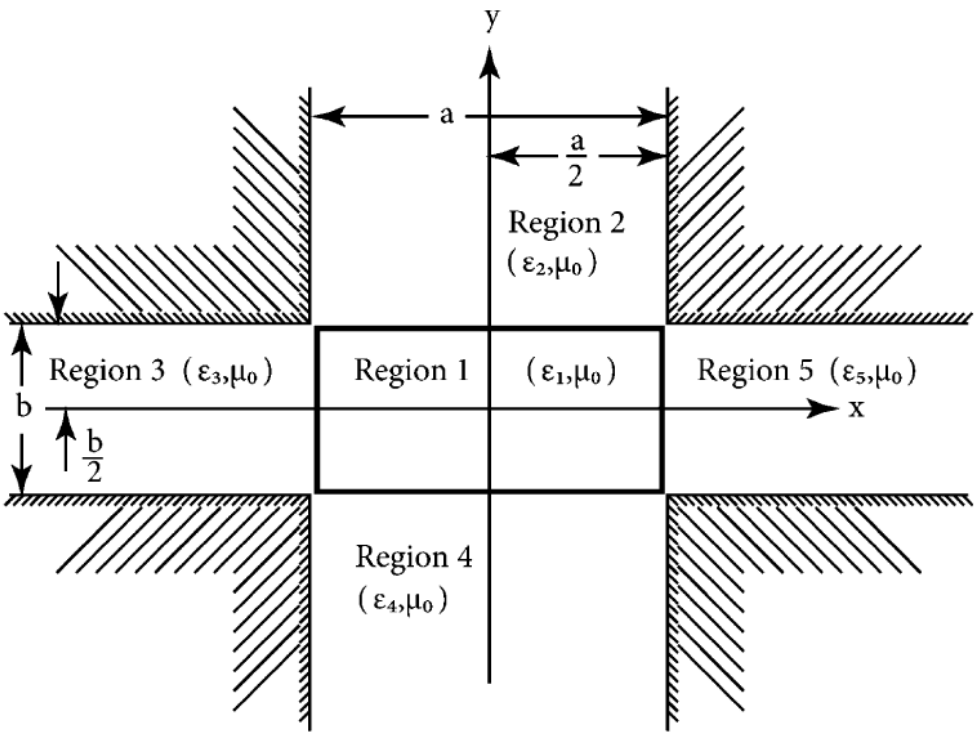

Figure 5.6: Cross-sectional rectangular geometry for Marcatili's approximate approach. [52]

Marcatili's approach is based on the assumption that:

$$\frac{n_1}{n_i} - 1 \ll 1 \qquad \forall\, i = 2, 3, 4, 5. \tag{5.46}$$

This implies that $k_x, y \ll k_z$. Therefore, $E_x \sim O(k_x k_y)$, $(E_z, H_z) \sim O(k_z)$ and $(E_y, H_x) \sim O(1)$. The electric field is calculated in each region, and continuity equations are applied between each region interface[10].

[10]For further developments and complete equations, please see Section 7.1 of the book "The Essence of dielectric waveguide" by C. Yeh and F. Shimabukuro. [52]. The solver directly implemented in the algorithm comes from waveguide.sourceforge.net. [49]

The solver found was created by W. Westerveld from the TU Delft, and corresponds directly to a buried channel waveguide as will be discussed here (Fig. 5.5a). This solver will now be called Extended Marcatili's Approach Waveguide Mode Solver (EMA WMS).

5.3.6.2 Full-vector finite difference mode solver

On the other hand, this solver is based on a full vectorial method applied to a finite difference approach. A classical mesh[11] of the region is represented in Fig.5.7. The solver first compute the longitudinal component H_z via the divergence equation $\boldsymbol{\nabla} \cdot \boldsymbol{H} = 0$ with the transverse components H_x, H_y. Afterwards, the polarisation field is computed as $\boldsymbol{\nabla} \times \boldsymbol{H} = j\omega \boldsymbol{D}$. Eventually, the electric field comes by $\boldsymbol{E} = \boldsymbol{\epsilon}^{-1} \boldsymbol{D}$.

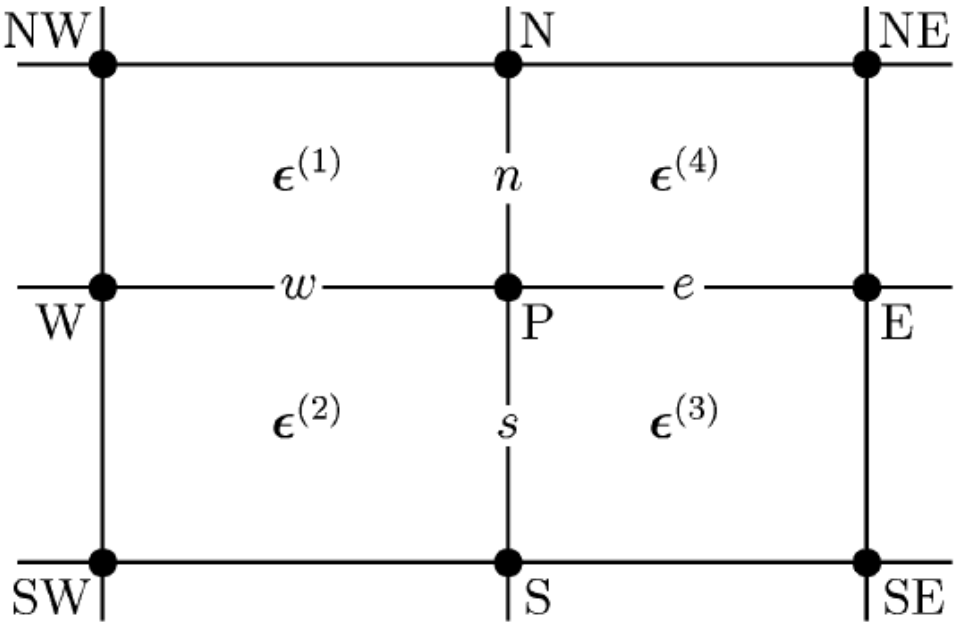

Figure 5.7: Diagram representing the mesh points used in finite difference equations. n, e, s, w denote distance between point of consideration and nearest mesh points. Superscripts label the surrounding mesh points as the usual compass directions. $\epsilon(i)$ indicate the dielectric permittivity tensors, assumed homogeneous within each rectangular region. [50]

Transverse magnetic field components are computed at point P by differential operators linked to the eight neighbour mesh points.[12]. It has been written by T.E. Murphy, but the solver is more oriented towards rib waveguides (Fig. 5.5c). This solver will now be called Full Vectorial Waveguide Mode Solver (FV WMS). The idea with the FV WMS is to adapt its input to describe as accurately as possible the buried channel waveguide structure to compare the outputs with the EMA WMS.

[11]The mesh represented here is rectangular uniform, but the mesh is not fixed and the solver can use other variations of mesh.

[12]For further developments and complete equations, please refer to [50]. The solver directly implemented in the algorithm comes from nl.mathworks.com.

5.3.6.3 Comparison

Both solvers have been used to compute the effective index difference and final phase shift of the following APS:

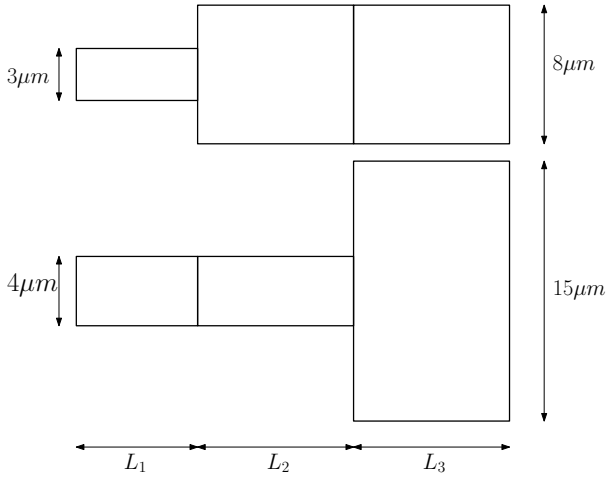

Figure 5.8: Schematic representation of the waveguide parameters used to compare the mode solvers. Not at scale horizontally.

$$\begin{aligned} a_1 &= [\,3,\ 8,\ 8]\ \mu\text{m}, \\ a_2 &= [\,4,\ 4,\ 15]\ \mu\text{m}, \\ b &= 5\ \mu\text{m}, \\ n &= 1.44. \end{aligned} \tag{5.47}$$

With these parameters, the effective indices are computed. The matrix system Eq. 5.45 is then solved to compute the length of each segment. The phase shift is finally obtained from Eq. 5.38.

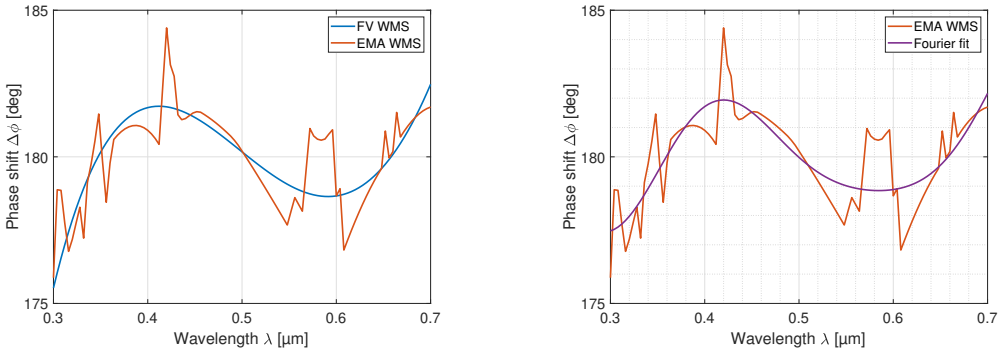

(a) $\lambda \in [0.3 - 0.7]$ μm.

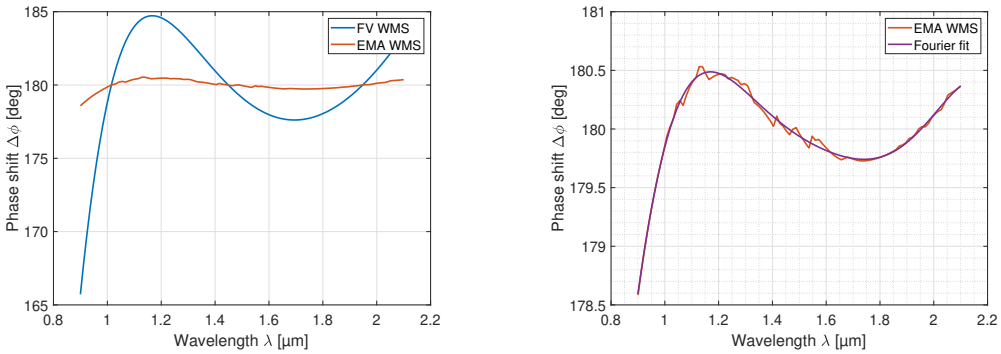

(b) $\lambda \in [0.9 - 2.1]$ μm.

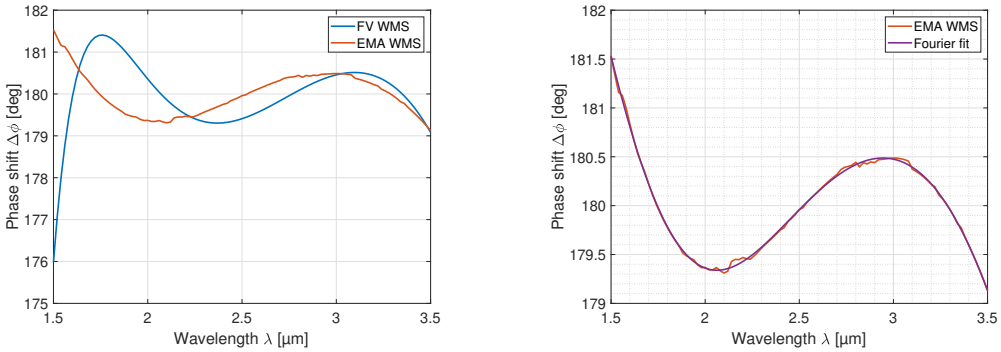

(c) $\lambda \in [1.5 - 3.5]$ μm.

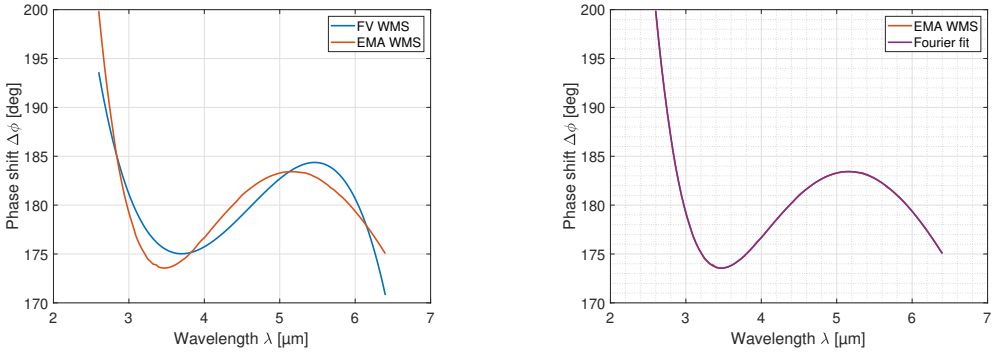

(d) $\lambda \in [2.6 - 6.4]$ μm.

Figure 5.9: Left: Comparison of the phase shifts computed with effective index differences from two different solvers. Right: Fourier interpolation on the erratic values computed by the EMA WMS.

As shown in the left graphs of Fig. 5.9, both solvers show the same behaviour. However, EMA WMS shows erratic behaviour. This has not been explained, nor tackled. Therefore, a fit according to a Fourier expansion is automatically computed to smooth the curve and provide more realistic variations. The resulting fits are given in the left graphs of Fig. 5.9. Therefore, the behaviour of the approximate buried channel solver (EMA WMS) has been confirmed by comparing to a more precise rib channel solver (FV WMS), and by a Fourier interpolation, the solver exhibits realistic results.

Consequently, the EMA WMS will be used for the MatLab simulations as it is faster and more adapted to the situation.

Chapter 6

Results

This chapter presents the results obtained with the optimisation algorithm implemented on MatLab. The lengths were firstly computed according to the wavelength, taking the spectral band as a whole or in subbands. The dielectric material considered is silica with a refractive index of around 1.44. Then, the impact of the height, spectral band discretisation, core cladding index difference and material index and dispersion has been evaluated.

6.1 Performance computation for silica with height fixed

The performances were computed for a waveguide of height $b = 5$ µm, for 20 wavelength steps across the spectral band. The widths were taken between 1 and 15 µm with a step of 0.5 µm[1]. The refractive index is defined at $n = 1.44$ across the whole spectral band, and the refractive index difference is fixed to $\Delta n = 0.01$. The objective here is to minimise the length and the results are summarised in Tab. 6.1.

Spectral band [µm]	Length [µm]	Widths [µm]	Mean error $\overline{\varepsilon}$ [deg]	Max error $\varepsilon_{\max}$ [deg]
$[0.3 - 0.7]$	31 880	1.5 1.5 15 1 3.5 3.5	0.456	0.756
$[0.9 - 2.1]$	31 008	2 2 15 1 5.5 5.5	0.5	1.75
$[1.5 - 3.5]$	71 846	2.5 2.5 15 1 7 7	1.49	5.82
$[2.6 - 6.4]$	309 106	3.5 3.5 15 1 9 9	4	2.16

Table 6.1: Shortest silica rectangular APS waveguide obtained for each spectral band when considering widths between 1 and 15 µm by step of 0.5 µm. Height is defined as $b = 5$ µm, refractive index $n = 1.44$ and core cladding difference $\Delta n = 0.01$ across whole spectral band. The overall behaviour of increasing length with growing wavelength is expected as the phase shift produced is smaller, therefore the length enlarges.

[1] This represents the computation of the whole algorithm (effective index difference, polynomial fit, matrix system resolution, phase shift and errors) for each of the 20 wavelength steps 74 908 times.

The APS of the first spectral band shows interesting performance. Its maximum phase defect is below the specification (1.15°), and the length is around 3 cm. The second and third APS are interesting as well as they show a length of around 3 and 7 centimetres respectively. However, their phase defect overshoots the requirement set at the beginning of the work. The last spectral band is discarded because of the length needed and the phase defect produced. The spectral bandwidth seems to be responsible for the increased length.

For the two middle spectral bands, the computation has been optimised towards finding the shortest APS respecting phase defect requirement of $\varepsilon_{\text{max}} < 1.15°$. This induces a second condition at the 6$^{\text{th}}$ and last step of the algorithm given page 75. The results are given in Tab. 6.2.

Spectral band [µm]	Length [µm]	Widths [µm]	Mean error $\overline{\varepsilon}$ [deg]	Max error ε_{max} [deg]
$[0.9 - 2.1]$	34 518	2.5 2.5 15 1 6.5 6.5	0.329	1.1
$[1.5 - 3.5]$	576 967	9 9 15 1 13 13	0.374	1.14

Table 6.2: Shortest rectangular dielectric APS waveguide satisfying the phase defect requirement obtained for the middle spectral bands when considering widths between 1 and 15 µm by step of 0.5 µm. Height defined at $b = 5$ µm, refractive index $n = 1.44$ and core cladding difference $\Delta n = 0.01$ across whole spectral band.

For the second spectral band [0.9 - 2.1] µm, the length only extends to around 3.4 centimetres, which is completely acceptable. However, for the larger spectral band, the length increases to almost 60 centimetres. This becomes quite complicated to implement in an integrated chip, and this spectral band is discarded as well. Conducting a study of the performance yield of a subdivision of the third and fourth spectral bands ([1.5 - 3.5] and [2.6 - 6.4] µm) would be interesting.

6.1.1 Impact of the spectral band discretisation

The level of discretisation of the spectral band may impact as well the performance. So far, each spectral band was divided in $N_\lambda = 20$ steps. The performances of the APS found for the two first spectral bands (shown in Tab. 6.1 are evaluated according to a growing level of spectral band discretisation. The results are given in Tab. 6.3.

N_λ	$\partial\lambda$ [nm]	L_{tot} [µm]	$\overline{\varepsilon}$ [deg]	ε_{max} [deg]
10	40.0	32 150	0.51	0.83
20	20.0	31 880	0.46	0.76
30	13.3	31 756	0.43	0.70
40	10.0	31 760	0.42	0.71
50	8.0	31 695	0.42	0.68
60	6.67	31 678	0.41	0.69
70	5.7	31 641	0.41	0.67
80	5.0	31 666	0.41	0.68
90	4.4	31 651	0.41	0.67
100	4.0	31 636	0.40	0.68

First spectral band [0.3 - 0.7] µm.

N_λ	$\partial\lambda$ [nm]	L_{tot} [µm]	$\overline{\varepsilon}$ [deg]	ε_{max} [deg]
10	120.0	34 557	0.37	0.94
20	60.0	34 518	0.33	1.10
30	40.0	34 497	0.32	1.16
40	30.0	34 493	0.31	1.19
50	24.0	34 479	0.31	1.20
60	20.0	34 479	0.31	1.21
70	17.14	34 480	0.30	1.22
80	15.0	34 478	0.30	1.23
90	13.33	34 475	0.30	1.23
100	12.0	34 471	0.30	1.24

Second spectral band [0.9 - 2.1] µm.

Table 6.3: Performance evolution with N from 10 to 100 by step of 10. Computation for the first spectral band with the widths given in Tab. 6.1. Refractive index is defined at $n = 1.44$ and height $b = 5$ µm.

The conclusion of the spectral band discretisation shows that the results with $N = 20$ are very close to the results with finer discretisation. Moreover, the finer the discretisation, the better the results, therefore the case $N = 20$ is well chosen as it provides faster calculations and lower performance. This allows concluding that the APS found with $N = 20$ will yield even better operation in actual conditions.

6.1.2 Impact of the height

The APS waveguide configuration providing the best results for the two selected spectral bands ([0.3 - 0.7] and [0.9 - 2.1] µm) have been evaluated with a height varying between 2 and 15 µm. The impact on the performance was negligible. Consequently, the computations performed here are defined independently of the height[2].

6.1.3 Impact of the core cladding index difference

On the contrary, increasing the core cladding difference leads to a clear worsening of the performance. The core cladding index difference was varying between 0.01 and 0.1 by step of 0.1 µm. The computation of higher than 0.1 values would violate one of the assumptions of the mode

[2]One shall note that, however, the height plays a role in the modal behaviour of the waveguide. This will have to be validated through numerical simulations.

solver, therefore the results would not be reliable. The performances for each value of Δn are shown in Tab. 6.4.

Δn	L_{tot} [µm]	$\overline{\varepsilon}$ [deg]	ε_{max} [deg]
0.01	31 879	0.46	0.76
0.02	49 902	0.70	1.09
0.03	72 458	0.85	1.37
0.04	96 824	0.97	1.61
0.05	123 413	0.99	1.64
0.06	153 012	1.01	1.66
0.07	187 039	1.09	1.88
0.08	219 622	1.07	1.87
0.09	259 182	1.10	1.97
0.10	301 528	1.15	2.23

Table 6.4: Performance evolution with Δn from 0.01 to 0.10 by step of 0.1.

Consequently, the two first spectral bands are appropriate for an integrated optics APS made of rectangular dielectric waveguides of varying widths. The geometries providing the shortest total silica APS and satisfying the phase defect requirement are the following:

$\lambda \in [0.3 - 0.7]$ µm			
Length [µm]	8 408	7 044	16 427
Width [µm]	1.5	1.5	15
	1	3.5	3.5

Table 6.5: First spectral band rectangular dielectric APS geometry.

$\lambda \in [0.9 - 2.1]$ µm			
Length [µm]	3 055	3 010	28 452
Width [µm]	2.5	2.5	15
	1	6.5	6.5

Table 6.6: Second spectral band rectangular dielectric APS geometry.

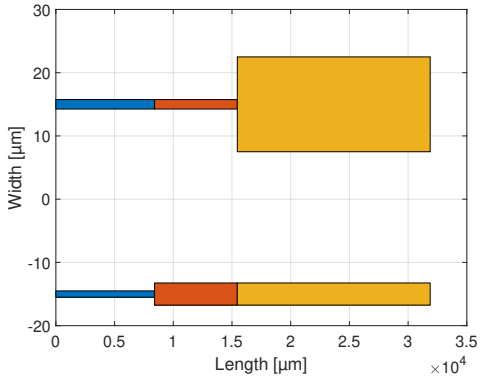

Figure 6.1: Representation of the APS. Transverse axis not on scale.

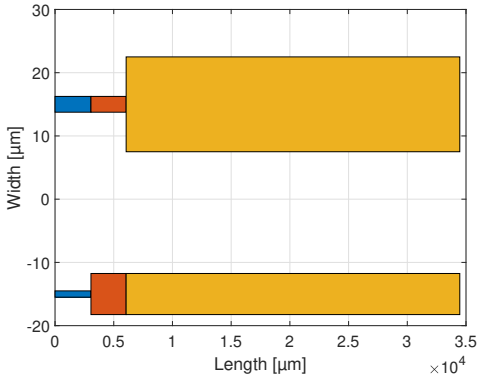

Figure 6.2: Representation of the APS. Transverse axis not on scale.

The spectral phase shift and rejection ratio (from Eq. 5.38 and 3.7 respectively) have been plotted for the middle spectral bands in Fig. 6.3.

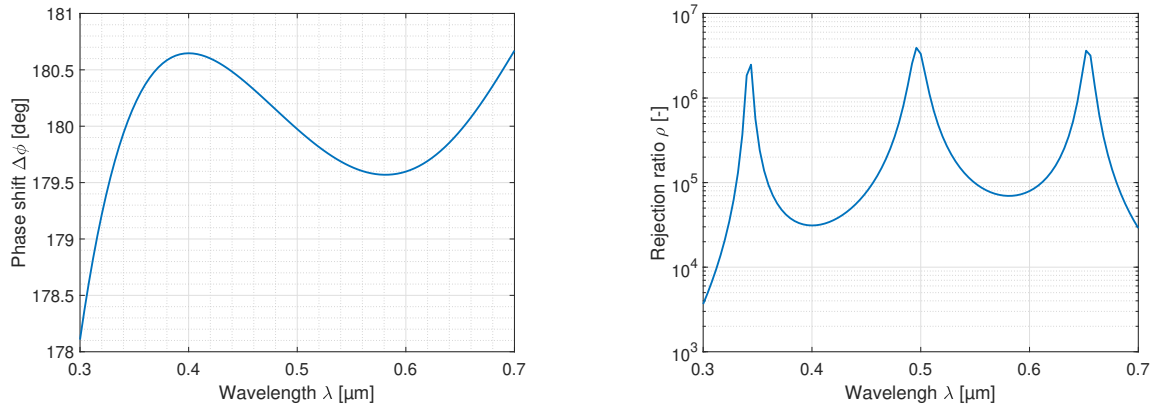

(a) $\lambda \in [0.3 - 0.7]$ µm.

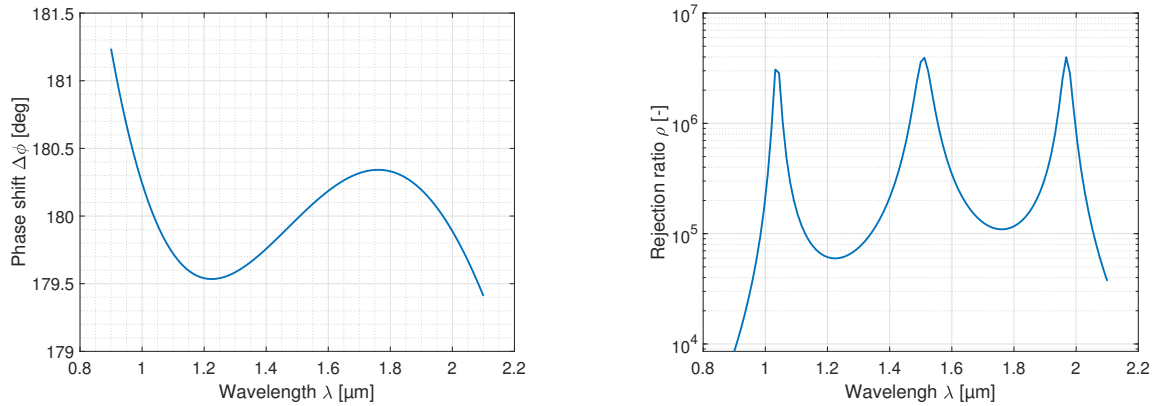

(b) $\lambda \in [0.9 - 2.1]$ µm.

Figure 6.3: Phase shift and rejection ratio achieved with dielectric rectangular waveguides made of silica. The geometric parameters are given in Tab. 6.1.

The rejection ratio exhibited by those waveguides is above 10^4 apart from a small region between 0.3 and 0.33 µm. Consequently, those two APS made of rectangular dielectric waveguides can be considered effective for the spectral bands [0.3 - 0.7] µm and [0.9 - 2.1] µm.

6.2 Division of discarded spectral bands

The third and fourth spectral bands were discarded because of their length and phase defect performance. An APS satisfying the phase defect requirement with an acceptable length was found for the third spectral band, however for the fourth one, no APS with acceptable wavelength was found[3]. Their parameters were:

[3]As a matter of fact, the only APS satisfying the phase defect requirement for the last spectral band had a total length of 33 meters..

Spectral band [µm]	Length [µm]	Widths [µm]	Mean error $\overline{\varepsilon}$ [deg]	Max error $\varepsilon_{\max}$ [deg]
$[1.5-3.5]$	576 967	9 9 15 1 13 13	0.374	1.14
$[2.6-6.4]$	309 106	3.5 3.5 15 1 9 9	4	2.16

Table 6.7: Performance of a silica rectangular integrated optics APS with $b = 5$ µm, $n = 1.44$ and $\Delta n = 0.01$ across the whole spectral band.

The division of those discarded spectral bands into narrower bands would allow relaxing the complexity of the system and yields smaller APS. However, this would imply using a wavelength splitter introducing other losses and errors that have been not taken into account here.

6.2.1 Third spectral band

The third band is divided in two to four subbands, providing a spectral sub-band of around 0.95 µm ($N = 2$), 0.60 µm ($N = 3$), and 0.40 µm ($N = 4$) wide[4]. The results are given in Tab. 6.8.

Sub-bands [µm]		L_{tot} [µm]	Widths [µm]	$\overline{\varepsilon}$ [deg]	$\varepsilon_{\max}$ [deg]
2	[1.50 - 2.40]	46 158	2 2 15 1 6 6	0.229	0.473
	[2.50 - 3.40]	106 253	3 3 15 1 8 8	0.104	0.189
3	[1.50 - 2.10]	40 248	2 2 15 1 6 6	0.074	0.104
	[2.20 - 2.80]	75 276	3 3 15 1 7 7	0.053	0.078
	[2.90 - 3.50]	129 941	3 3 15 1 8 8	0.033	0.041
4	[1.50 - 1.90]	36 939	2 2 15 1 6 6	0.022	0.033
	[2.00 - 2.40]	58 799	2 2 15 1 7 7	0.020	0.025
	[2.50 - 2.90]	91 346	3 3 15 1 7 7	0.014	0.025
	[3.00 - 3.50]	128 234	3 3 15 1 8 8	0.016	0.021

Table 6.8: Performance of APS of the spectral band $[1.5-3.5]$ µm when divided in sub-bands. Computation with height $b = 5$ µm, refractive index $n = 1.44$ and core cladding index difference of 0.01 across whole spectral band.

[4]For both spectral band divisions $\Delta\lambda$ into N sub-bands, the resulting smaller spectral bands $\partial\lambda$ are not exactly equal to the total spectral width divided by the number of sub-bands: $\partial\lambda \neq \Delta\lambda/N$. This is explained by the discretisation of the spectral region into a finite number of values, defined as 20 in this study.

6.2.2 Fourth spectral band

The same study were conducted over the fourth spectral band, [2.6 - 6.4] µm. This band is also divided in two to four subbands, providing a spectral sub-band of around 1.9 µm ($N = 2$), 1.20 µm ($N = 3$), and 0.90 µm ($N = 4$) wide[4]. The results are given in Tab. 6.9.

Sub-bands [µm]		L_{tot} [µm]	Widths [µm]	$\overline{\varepsilon}$ [deg]	ε_{max} [deg]
2	[2.60 - 4.50]	168 735	4 4 15 1 9.5 9.5	0.518	1.12
	[4.69 - 6.40]	623 159	4.5 4.5 15 1 10 10	0.449	0.983
3	[2.60 - 3.74]	125 669	3 3 15 1 8 8	0.237	0.338
	[3.93 - 5.07]	335 815	4 4 15 1 9 9	0.139	0.159
	[5.26 - 6.40]	834 594	5 5 15 1 10 10	0.078	0.093
4	[2.60 - 3.36]	108 756	3 3 15 1 8 8	0.063	0.095
	[3.55 - 4.31]	230 015	4 4 15 1 9 9	0.044	0.062
	[4.50 - 5.26]	436 596	4 4 15 1 10 10	0.034	0.063
	[5.45 - 6.40]	792 074	5 5 15 1 11 11	0.037	0.053

Table 6.9: Performance of APS of the spectral band $[2.6 - 6.4]$ µm when divided in sub-bands. Computation with height $b = 5$ µm, refractive index $n = 1.44$ and core cladding index difference of 0.01 across whole spectral band.

The conclusion of the study of the division of too wide and too high spectral bands is that the less effective sub-band is the lowest one, and the longest is the highest one. Therefore, for the study of a spectral band of width $\Delta\lambda = \lambda_{\text{max}} - \lambda_{\text{min}}$ division in more than 4 sub-bands ($N > 4$), one has to define the sub-band spectral width $\delta\lambda = \Delta\lambda/N$. Then, only the phase defect compliance of the first sub-band $[\lambda_{\text{min}} - (\lambda_{\text{min}}+\delta\lambda)]$ and the length of the last sub-band $[(\lambda_{\text{max}}-\delta\lambda) - \lambda_{\text{max}}]$ have to be verified.

6.3 Performance computation with varying refractive index

Integrated optics are mainly realised in silica or well-known materials. However, the evolution of the APS performance according to the material used can be very interesting, as technological achievements would surely soon make possible such waveguides. Consequently, the computation of the evolution of the length of the APS according to the refractive index could yield interesting results. The total lengths have thus been computed according to a core refractive index varying from 1.1 to 5 µm by step of 0.1 µm. The widths have been fixed to the

configuration generating the shortest APS for the middle spectral bands. The result is given in Fig. 6.4.

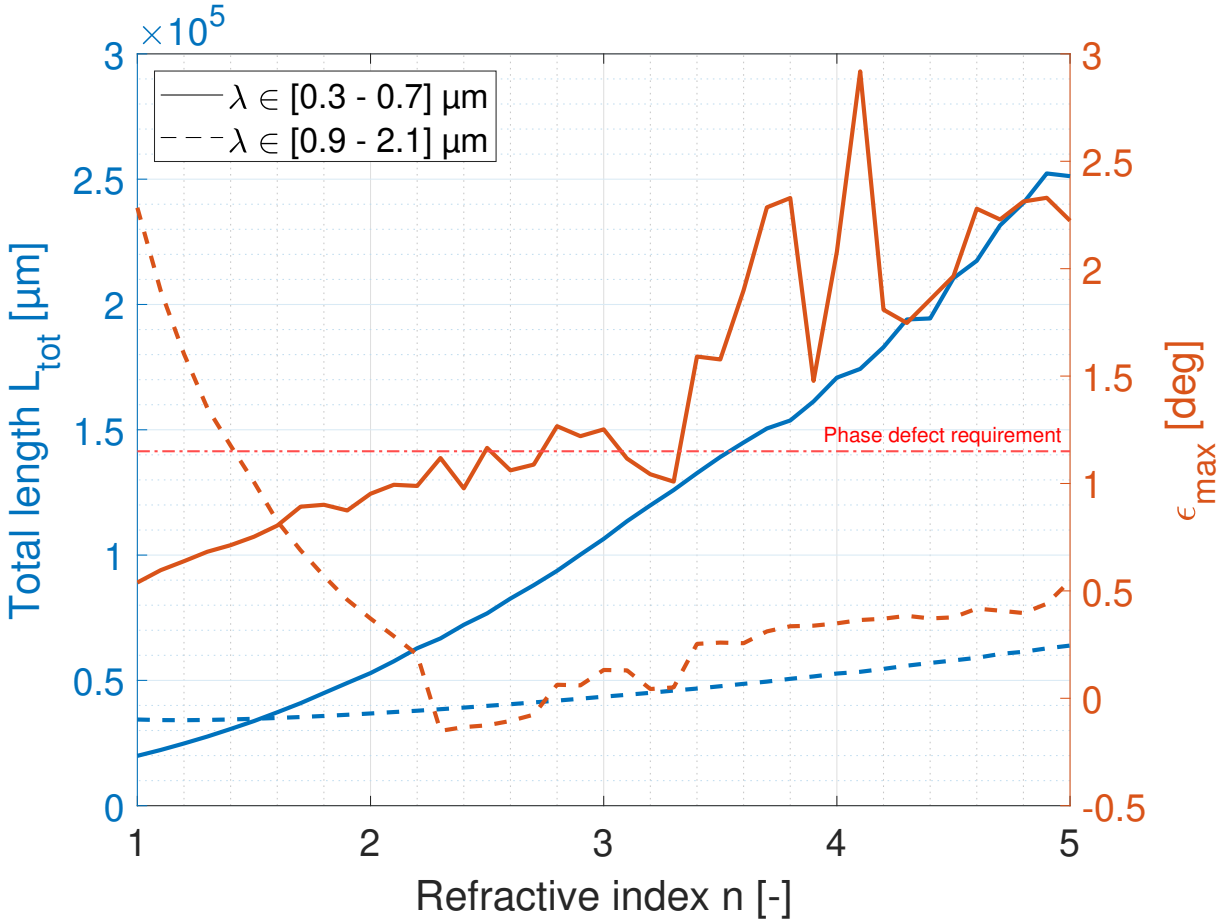

Figure 6.4: Evolution of the length of an APS with fixed widths when its core refractive index is modified for the two first spectral bands. Full line corresponds to first spectral band, and dashed line for second spectral band. Blue curves indicate the total length variation, and orange curves show the maximal error evolution. A dashed-dotted red curve indicates the pahse defect requirement. The widths for the two spectral bands are stated in Tab.6.1. The core cladding index difference is $\Delta n = 0.01$, and the height is fixed to $b = 5$ µm.

On the one hand, a higher refractive index seems to increase the length of the APS. This effect is stronger for the first spectral band, showing an increase by a factor of 12 from $L(n = 1) = 19.9$ mm to $L(n = 5) = 250$ mm. The second spectral band only increases by around 85% from $L(n = 1) = 34.3$ mm to $L(n = 5) = 63.9$ mm.

For the second spectral band illustrated by dashed curves, the values stay in an acceptable range. The material selection is therefore only based on the material dispersion (a stable refractive index across the band), its throughput, and its technical feasibility for integrated optics. However, for the first spectral band in full curves, a refractive index higher than 2.5 leads to a length above 10

centimetres, which starts to be technically complicated. For this band, the material must satisfy the previous conditions with a refractive index must be lower than 2.5.

On the other hand, the maximal error varies differently according to the spectral band.

6.4 Consideration of the material dispersion

The refractive index was fixed to 1.44 for all spectral bands and all wavelengths. However, silica is subject to dispersion: its refractive index varies with wavelength. This variation is described by its Sellmeier equation:

$$n^2 - 1 = \frac{0.663044\,\lambda^2}{\lambda^2 - 0.036} + \frac{0.517852\,\lambda^2}{\lambda^2 - 0.011236} + \frac{0.175912\,\lambda^2}{\lambda^2 - 0.014161} + \frac{0.565380\,\lambda^2}{\lambda^2 - 78.216336} + \frac{1.675299\,\lambda^2}{\lambda^2 - 430.230564}. \tag{6.1}$$

The refractive index varies thus between $n(0.3\ \mu\text{m}) = 1.578$ and $n(0.7\ \mu\text{m} = 1.541$ for the first spectral band and $n(0.9\ \mu\text{m}) = 1.537$ and $n(2.1\ \mu\text{m}) = 1.519$ for the second one. The modifications on the algorithm results for the two selected spectral bands are compared in 6.10.

Band [µm]	L_{tot} [µm]	Widths [µm]	$\overline{\varepsilon}$ [deg]	ε_{max} [deg]	L_{tot} [µm]	Widths [µm]	$\overline{\varepsilon}$ [deg]	ε_{max}[deg]
$[0.3-0.7]$	31 880	1.5 1.5 15 1 3.5 3.5	0.456	0.756	37 076	1.5 1.5 15 1 3 3	0.528	0.88
$[0.9-2.1]$	34 518	2.5 2.5 15 1 6.5 6.5	0.329	1.1	32 813	2 2 15 1 6.5 6.5	0.34	1.13
	$n = 1.44\ \forall\lambda$				$n = n(\lambda)$ (see Eq. 6.1)			

Table 6.10: Comparison of the algorithm outputs and performances when material dispersion is taken into account. Height is $b = 5$ µm and core cladding index difference fixed to $\Delta n = 0.01$.

The performances are slightly worsened by the material dispersion. This is mainly because the computation was done with a refractive index $n = 1.44$ far from the values at those wavelengths (around 1.54).

6.5 Conclusions on the MatLab simulations

The MatLab simulations are based on the optimisation of the length according to a second-order polynomial fit of the effective index difference between waveguides of different widths. The effective index is computed with the EMA WMS solver. The refractive index and core cladding index difference are considered constant across the whole spectral band. The algorithm outputs showed that for the two first spectral bands, an APS respecting the phase requirement would be feasible in silica with a core cladding index difference of 0.01. Both presented a total length of around 3.5 centimetres and a rejection ratio above 10^4. The two discarded spectral bands were

divided into sub-bands. With 4 sub-bands, the third spectral band [1.5 - 3.5] can be considered, as the longest APS reaches 12 centimetres. However, the fourth spectral [2.6 - 6.4] band would require more than 4 subdivisions to be technically feasible.

Studies on the impact of the refractive index, core cladding index difference, height, spectral discretisation and material dispersion were conducted. The impact of height, spectral discretisation and material dispersion were negligible. However, a growing core cladding index difference provided an important worsening of the performance. Similarly, increasing the refractive index lead to a modification of the length and maximal error. This modification was worse for smaller wavelengths (the first spectral band was the most impacted).

6.6 Further steps

This section concerns the further steps identified to get further knowledge and simulation about integrated optics phase shifters.

6.6.1 FDTD simulation

The next step after the simulation of the phase shift based on an approximate approach using a self-implemented MatLab solver is to confirm the results with an exact finite difference resolution

The task will be to compare the phase shift computed by the MatLab algorithm, and the modal behaviour.

A software, OptiFDTD, was accessed but only for a 30-days evaluation which ran off before the advent of the most recent and promising designs.

6.6.2 Tapers

The instantaneous variation of width as shown in the previous sections is directly responsible for energy loss. To enhance the throughput, tapers are usually inserted to provide a smooth variation of the geometry.

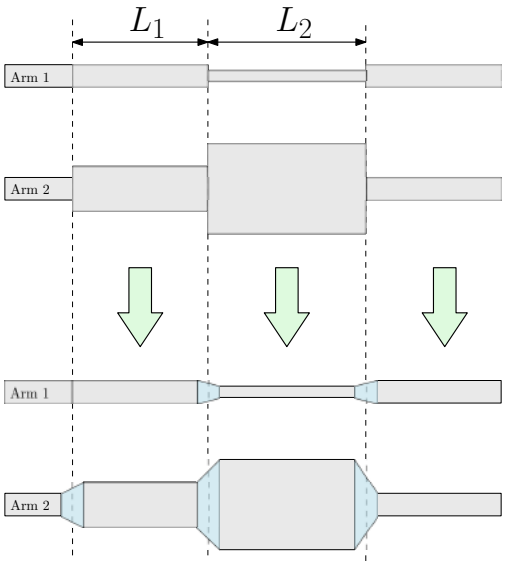

Figure 6.5: Insertion of tapers at elements interfaces to enhance total throughput.

Their slope, linked to the initial, finite width and length, is linked to an adiabatic condition that ensures negligible losses: [38]

$$\theta(z) < \frac{\rho(z)}{2\pi}(\beta - k\, n_{co}). \tag{6.2}$$

However, they imply a modification of the phase shift. According to the tapers inserted in each arm, the phase shifts across each arm vary differently. The tapers' impact on the phase difference between each arm can be cancelled by incorporating the tapers of each arm in the other arm, at the end of the APS. However, the total phase shift is modified, and therefore the widths of the elements must be redefined as well.

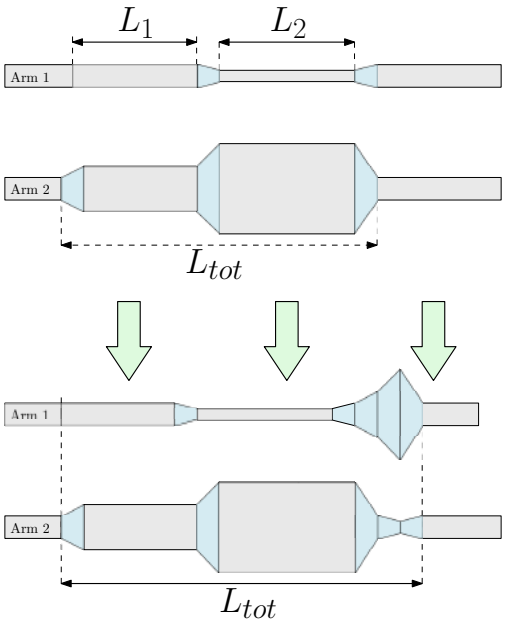

Figure 6.6: Completion of each arm with the tapers from the other arm to reach a symmetric system and cancel the relative phase shift defect linked to the tapers. However, total length is greater, therefore the total phase shift is modified, and the widths needs to be recomputed.

6.6.3 Optical fibre

Optical fibre consists of a dielectric waveguide of circular section. The geometrical approach is also relevant, and the electromagnetic description holds just by switching to cylindrical coordinates. However, optical fibres have not been simulated in the frame of this work. The principle is the same: a variation of the geometry of the waveguide to modify the effective index to tune the phase shift. The technological realisation of optical fibres with varying core dimensions seems more complex than for rectangular waveguides but nonetheless could exhibit very interesting properties. It could lead to the combination of two roles: guide light from the telescope, and perform the phase shift in the same component.

Chapter 7

Conclusion

Space-based interferometry is one of the most challenging endeavours of modern astrophysics, and its implementation could revolutionise exoplanet science.

Exoplanet monitoring, detection or characterisation is very complicated because of the proximity to their host stars (from Earth point of view). However, a remarkable technique allows to cancel the starlight and measure only the flux coming from the exoplanet: nulling interferometry. Nulling interferometry relies on introducing a phase shift between the arms of two telescopes. Thanks to this phase shift, the recombination of both images produces an interferometric pattern on the observed area. If carefully designed, the transmission pattern shows a perfect null on the star location, leading to extinction of its flux.

The potential of enhanced exoplanet detection drove it at the top of the agenda of major space agencies and ground observatories around early 2000 (TPF, Darwin, FKSI, etc.). Achieved in ground-based observatories, this technique could provide significant breakthroughs in exoplanet science if it was implemented in space. However, the complexity of the task and the technical difficulties encountered brought all space-based interferometry projects to stop around 2010. Recently, ESA has shown a new interest in this technology by initiating in 2017 the LIFE project. Breakthroughs in exoplanet understanding and significant technical progress motivated this renewal, reevaluating the feasibility of the project.

This work builds on that momentum. The objective was to evaluate different concepts able to achieve the phase shift during the nulling process. Several criteria were evaluated such as performance, technological feasibility, affordability, stability, thermo-optic behaviour, etc. A trade-off between existing concepts has been performed, leading to the selection of three candidates: wedge prisms, Fresnel rhombs and integrated optics. Amongst them, integrated optics has been peculiarly investigated.

Wedge prisms and Fresnel rhombs showed great behaviour, but the implementation of bulk optics and mechanical stability needed are serious drawbacks for a space-based mission. The advantage of integrated optics resides in the combination of a spatial filtering function and the achromatic phase shift. Buried channel waveguides were studied here.

However, the higher and wider the bandwidth, the longer the APS, and only the two first spectral bands ([0.3 - 0.7] µm and [0.9 - 2.1] µm) showed feasible lengths. The rejection ratio requirement

of 10^4 was achieved on the whole band with waveguides in silica of width varying between 1 and 15 µm and for a total length less than 4 centimetres. This result is very encouraging as those spectral bands correspond to the CubeSat 6U and 12U, the smallest intended satellites. The implementation of an integrated APS together with the spatial filtering property could be very interesting for small satellites.

The impacts of several parameters such as height, material refractive index, core cladding index difference, material dispersion, and spectral discretisation have been evaluated. Increasing the core cladding index difference could enhance the throughput by stronger light confinement, but leads to worsening of the performance (phase defect and total length). Higher the material refractive index, longer is the APS, and shortest wavelengths are more impacted by this modification. A maximum refractive index of around 2.5 has been found for the first spectral band. Otherwise, the selected material must be implementable in integrated optics, show good throughput and low dispersion across the spectral band.

The two discarded spectral bands, [1.5 - 3.5] and [2.6 - 6.4] were further investigated by dividing each of them into sub-bands. A number of up to 4 sub-bands have been simulated, however the maximum length was around 13 and 80 centimetres respectively, which is not convenient in integrated optics. However, a tendency allowing to study way faster the sub-band division was highlighted: the first sub-band shows the worst phase defect, and the last sub-band is the longest. This allows studying only two sub-bands for each subdivision into $N > 4$ sub-bands.

For those two larger spectral bands, their too great bandwidth makes the use of compensated or dispersive phase shift complicated. For those bands, a mirror approach based on the intrinsic achromaticity of metallic reflection would be more suitable.

Further prospects of this work regarding integrated optics would incorporate a FDTD simulation of the APS designed here. An evaluation of the throughput of those bare designs would determine if tapers are needed or not. The study of the technical feasibility of optical fibres based on the same principle would also provide more information about a comparison between rectangular and circular waveguides. A testing in the laboratory of several Fresnel rhombs and dispersive prisms could provide relevant information about throughput and feasibility of the concepts. Finally, the mirror approach should be studied for the two larger spectral bands.

Bibliography

[1] Colin Dandumont et al. “Exoplanet detection yield of a space-based Bracewell interferometer from small to medium satellites”. In: *Journal of Astronomical Telescopes, Instruments, and Systems* 6.03 (Sept. 2020). https://doi.org/10.1117/1.jatis.6.3.035004 (cit. on pp. 1, 16).

[2] Natalie M. Batalha. “Exploring exoplanet populations with NASA’s Kepler Mission”. In: *Proceedings of the National Academy of Sciences* 111.35 (2014), pp. 12647–12654. ISSN: 0027-8424. DOI: 10.1073/pnas.1304196111. eprint: https://www.pnas.org/content/111/35/12647.full.pdf. https://www.pnas.org/content/111/35/12647 (cit. on p. 3).

[3] Anna V (https://physics.stackexchange.com/users/1492/anna v). *How is a blackbody spectrum formed in the Sun?* Physics Stack Exchange. URL:https://physics.stackexchange.com/q/167795 (version: 2020-06-04). eprint: https://physics.stackexchange.com/q/167795. https://physics.stackexchange.com/q/167795 (cit. on p. 4).

[4] Eugene A. Magnier et al. “Pan-STARRS Pixel Analysis: Source Detection and Characterization”. In: *The Astrophysical Journal Supplement Series* 251.1 (Oct. 2020), p. 5. DOI: 10.3847/1538-4365/abb82c. https://doi.org/10.3847/1538-4365/abb82c (cit. on p. 6).

[5] Michel Mayor and Didier Queloz. “A Jupiter-mass companion to a solar-type star”. In: *Nature* 378.6555 (Nov. 1995), pp. 355–359. DOI: 10.1038/378355a0. https://doi.org/10.1038/378355a0 (cit. on pp. 8, 10).

[6] NASA. *Exoplanet exploration*. Accessed 19^{th} of April 2021. https://exoplanets.nasa.gov/ (cit. on p. 8).

[7] William Borucki. “Kepler: Updated Exoplanet Statistics and an Estimate of the Frequency of Planetary Candidates in the Habitable Zone”. In: (May 2012) (cit. on p. 8).

[8] Gijs D. Mulders. “Planet Populations as a Function of Stellar Properties”. In: *Handbook of Exoplanets*. Springer International Publishing, 2018, pp. 2009–2034. DOI: 10.1007/978-3-319-55333-7_153 (cit. on p. 8).

[9] Ari Silburt, Eric Gaidos, and Yanqin Wu. “A statistical reconstruction of the planet population around Kepler solar-type stars”. In: *The Astrophysical Journal* 799.2 (Jan. 2015), p. 180. DOI: 10.1088/0004-637x/799/2/180. https://doi.org/10.1088/0004-637x/799/2/180 (cit. on p. 8).

[10] O. Struve. “Proposal for a project of high-precision stellar radial velocity work”. In: *The Observatory* 72 (Oct. 1952), pp. 199–200 (cit. on pp. 8, 10).

[11] American Public University System. *Exoplanet Transit Photometry*. Website last accessed the 30^{th} of April. https://www.apus.edu/academic-community/space-studies/exoplanet-transit-photometry (cit. on p. 9).

[12] Valerio Bozza. *Methods of detecting exoplanets*. 1st Advanced School on Exoplanetary Science. Switzerland: Springer, 2016. ISBN: 978-3-319-27458-4 (cit. on pp. 9, 11, 12).

[13] ESO European SOuth Observatory. *ESPRESSO News and Press Releases*. Online wbesite. LAst accessed 26^{th} of May. https://www.eso.org/sci/facilities/paranal/instruments/espresso/news.html (cit. on p. 11).

[14] Robert Nemiroff, Jerry Bonnell, and Phillip Newman. *A Horseshoe Einstein Ring from Hubble - Astronomy Picture of the Day*. https://apod.nasa.gov/apod/ap111221.html (cit. on p. 12).

[15] *Exploring Exoplanets with Microlensing*. Sagan Exoplanet Summer Workshop, California Institute of Technology. 2011. https://nexsci.caltech.edu/workshop/2011/ (cit. on p. 13).

[16] J. Schneider et al. "Defining and cataloging exoplanets: the exoplanet.eu database". In: *Astronomy & Astrophysics* 532 (July 2011). Online database selected : exoplanet.eu/catalog), A79. DOI: 10.1051/0004-6361/201116713. https://doi.org/10.1051/0004-6361/201116713 (cit. on p. 14).

[17] R. N. Bracewell. "Detecting nonsolar planets by spinning infrared interferometer". In: *Nature* 274.5673 (Aug. 1978), pp. 780–781. DOI: 10.1038/274780a0. https://doi.org/10.1038/274780a0 (cit. on pp. 15, 16).

[18] Bertrand Mennesson, Alain Léger, and Marc Ollivier. "Direct detection and characterization of extrasolar planets: The Mariotti space interferometer". In: *Icarus* 178.2 (Nov. 2005), pp. 570–588. DOI: 10.1016/j.icarus.2005.05.012. https://doi.org/10.1016/j.icarus.2005.05.012 (cit. on p. 16).

[19] Olivier Absil. *Astrophysical studies of extrasolar planetary systems using infrared interferometric techniques*. PhD thesis. Université de Liège - Département d'Astrophysique, Géophysique et Océanographie. 2006 (cit. on p. 16).

[20] Laurent Escarrat. *Contribution au mode coronographique de la mission Darwin.* Astrophysique [stro-ph]. université Nice Sophia Antipolis. Français. tel-00011592. 2003 (cit. on pp. 17, 30).

[21] NSO National Schools Observatory. *Very Large Telescope (VLT).* https://www.schoolsobservatory.org/learn/eng/tels/groundtel/vlt (cit. on p. 19).

[22] *Very Large telescope : The world's most advanaced visible-light astronomical observatory.* European Southern Observatory. https://www.eso.org/public/unitedkingdom/teles-instr/paranal-observatory/vlt/?lang (cit. on p. 19).

[23] Scott Johnson. *Building the world's highest-resolution telescope*. ARS technica. https://arstechnica.com/science/2018/07/meet-the-telescope-that-may-soon-show-you-an-exo-eclipse/ (cit. on p. 20).

[24] Frank Brachet. *Etude et développement d'un déphaseur achromatique pour l'interférométrie en frange noire"*. Français. Astrophysique [astro-ph]. Université Paris-Sud - Paris XI. <tel-00011990>. 2005. https://tel.archives-ouvertes.fr/tel-00011990 (cit. on pp. 27, 29, 34, 44, 47).

[25] Bruno Chazelas et al. *Achromatic Phase SHifters for Nulling Interferometers*. ESTEC Contrat No. 17 005/02/NL/JA-. May 2009 (cit. on pp. 28, 29, 49).

[26] Francois Hénault. "Computing extinction maps of star nulling interferometers". In: *Optics Express* 16.7 (Mar. 2008), p. 4537. DOI: 10.1364/oe.16.004537. https://doi.org/10.1364/oe.16.004537 (cit. on p. 30).

[27] Yves Rabbia et al. *Achromatic phase shifters : the "mirror" approaches*. Ed. by H. Lacoste. ESA SP-522. 2002 (cit. on pp. 31–34).

[28] E. Serabyn and M. M. Colavita. "Fully symmetric nulling beam combiners". In: *Applied Optics* 40.10 (Apr. 2001), p. 1668. DOI: 10.1364/ao.40.001668. https://doi.org/10.1364/ao.40.001668 (cit. on p. 31).

[29] Y. Rabbia et al. "Review of Concepts and Constraints for Achromatic Phase Shifters". In: *GENIE - DARWIN Workshop - Hunting for Planets*. Ed. by H. Lacoste. Vol. 522. ESA Special Publication. Mar. 2003, p. 12.1 (cit. on pp. 32, 36, 39, 44).

[30] E. Serabyn et al. "Deep nulling of visible laser light". In: *Applied Optics* 38.34 (Dec. 1999), p. 7128. DOI: 10.1364/ao.38.007128 (cit. on p. 34).

[31] Eugene Serabyn. "Nulling interferometry: symmetry requirements and experimental results". In: *Interferometry in Optical Astronomy*. Ed. by Pierre J. Lena and Andreas Quirrenbach. SPIE, July 2000. DOI: 10.1117/12.390223. https://doi.org/10.1117/12.390223 (cit. on p. 34).

[32] Jean Gay et al. "Un coronographe interférentiel achromatique coaxial". In: *Comptes Rendus Physique* 6.10 (Dec. 2005), pp. 1169–1175. DOI: 10.1016/j.crhy.2005.12.001 (cit. on p. 34).

[33] P. Baudoz, Y. Rabbia, and J. Gay. "Achromatic interfero coronagraphy". In: *Astronomy and Astrophysics Supplement Series* 141.2 (Jan. 2000), pp. 319–329. DOI: 10.1051/aas:2000120 (cit. on p. 34).

[34] Jean Gay, Yves Rabbia, and Pierre Baudoz. "Le coronographe interférentiel achromatique". In: *Comptes Rendus de l'Académie des Sciences - Series IIB - Mechanics-Physics-Chemistry-Astronomy* 325.1 (July 1997), pp. 51–56. DOI: 10.1016/s1251-8069(97)83264-2 (cit. on p. 34).

[35] D. Mawet et al. "Achromatic Four Quadrant Phase Mask Coronagraph using the Dispersion of Form Birefringence". In: *EAS Publications Series* 8 (2003), pp. 117–128. DOI: 10.1051/eas:2003056. https://doi.org/10.1051/eas:2003056 (cit. on pp. 39, 57, 58).

[36] C. Hanot et al. "Fresnel rhombs as achromatic phase shifters for infrared nulling interferometry: first experimental results". In: *Techniques and Instrumentation for Detection of Exoplanets III*. Ed. by Daniel R. Coulter. Vol. 6693. International Society for Optics and Photonics. SPIE, 2007, pp. 468 –479. DOI: 10.1117/12.758405 (cit. on p. 39).

[37] ESA. *Technical Proposal - Review and discussions of APS requirements*. Ref. AO/1-3946/02/NL/JA. (cit. on pp. 41–44).

[38] Pierre Labeye. *Composants optiques intégrés pour l'Interférométrie astronomique*. Français. Optique [physics.optics]. Institut National Polytechnique de Grenoble - INPG. NNT : 2008INGP0008. tel-00870937. 2008. https://tel.archives-ouvertes.fr/tel-00870937 (cit. on pp. 43, 92).

[39] Lucas Labadie. *Optique intégrée dans l'infrarouge thermique : application à l'interférométrie en fange noire pour la recherche de planètes telluriques*. français. Astrophysique [astro-ph]. Université Joseph-Fourier - Grenoble I. tel-00011611v2. 2005. https://tel.archives-ouvertes.fr/tel-00011611v2 (cit. on pp. 43, 64, 67).

[40] Laëtitia Abel-Tiberini et al. "Transmission behaviors of single mode hollow metallic waveguides dedicated to mid-infrared nulling interferometry". In: *Optics Express* 15.26 (2007), p. 18005. DOI: 10.1364/oe.15.018005. https://doi.org/10.1364/oe.15.018005 (cit. on pp. 43, 64).

[41] Pierre Labeye et al. "Infrared single-mode hollow conductive waveguides for stellar interferometry". In: *Integrated Optics: Devices, Materials, and Technologies X*. Ed. by Yakov Sidorin and Christoph A. Waechter. SPIE, Feb. 2006. DOI: 10.1117/12.645075. https://doi.org/10.1117/12.645075 (cit. on pp. 43, 64).

[42] Pierre Riaud. "Coronographie à masque de phase: applications aux télescopes et interféromètres au sol et dans l'espace". tel-00004234. PhD thesis. Université Pierre et Marie Curie - Paris VI, Jan. 2003. https://tel.archives-ouvertes.fr/tel-00004234 (cit. on p. 44).

[43] V. Weber. *Ètude de l'interféromètre à frange noire MAII*. PhD thesis. Université de Nice-Sophia Antipolis. June 2004 (cit. on p. 47).

[44] Rhonda M. Morgan, James H. Burge, and Neville J. Woolf. "Final laboratory results of visible nulling with dielectric plates". In: *Interferometry for Optical Astronomy II*. Ed. by Wesley A. Traub. SPIE, Feb. 2003. DOI: 10.1117/12.459341 (cit. on p. 47).

[45] Arjan Lambertus Mieremet. *Nulling interferometry for exoplanet detection*. PhD thesis. Technische Universiteit Delft. 2003 (cit. on p. 47).

[46] Jeffrey L. Tosi and Kumar M. Khajurivala. *Common Infrared Optical Materials and Coatings: A Guide to Properties, Performance, and Applications*. Website regrouping informations and companies regarding optical materials. Last access on 30^{th} of May. https://www.photonics.com/Articles/Common_Infrared_Optical_Materials_and_Coatings_A/a25495 (cit. on pp. 51, 52).

[47] Liudmila Nickelson. "Rectangular Hollow Metallic Waveguides and Resonators". In: *Electromagnetic Theory and Plasmonics for Engineers*. Springer Singapore, Nov. 2018, pp. 425–543. DOI: 10.1007/978-981-13-2352-2_7. https://doi.org/10.1007/978-981-13-2352-2_7 (cit. on p. 64).

[48] Laëtitia Abel-Tiberini et al. "Transmission behaviors of single mode hollow metallic waveguides dedicated to mid-infrared nulling interferometry". In: *Optics Express* 15.26 (2007), p. 18005. DOI: 10.1364/oe.15.018005. https://doi.org/10.1364/oe.15.018005 (cit. on p. 64).

[49] Wouter J. Westerveld et al. "Extension of Marcatili's Analytical Approach for Rectangular Silicon Optical Waveguides". In: *Journal of Lightwave Technology* 30.14 (July 2012), pp. 2388–2401. DOI: 10.1109/jlt.2012.2199464. https://doi.org/10.1109/jlt.2012.2199464 (cit. on pp. 75, 76).

[50] Arman B. Fallahkhair, Kai S. Li, and Thomas E. Murphy. "Vector Finite Difference Modesolver for Anisotropic Dielectric Waveguides". In: *Journal of Lightwave Technology* 26.11 (June 2008), pp. 1423–1431. DOI: 10.1109/jlt.2008.923643. https://doi.org/10.1109/jlt.2008.923643 (cit. on pp. 75, 77).

[51] Fran cois Ladouceur. *Silica-based buried channel waveguides and devices*. London New York: Chapman & Hall, 1996. ISBN: 978-0-412-57930-1 (cit. on p. 75).

[52] C. Yeh and F. I. Shimabukuro. *The Essence of Dielectric Waveguides*. Springer US, 2008. DOI: 10.1007/978-0-387-49799-0. https://doi.org/10.1007/978-0-387-49799-0 (cit. on p. 76).

[53] Sissi Cao. *Elon Musk Reveal's SpaceX's Timeline for Landing Humans On Mars*. Article about the declarations of Elon Musk, SpaceX CEO, at the Axel Springer Award 2020. Accessed April, 20^{th}. Dec. 2020.

[54] Denis Defrère. *Characterizing extrasolar planetary systems using infrared interferometry*. PhD thesis. Université de Liège - Département d'Astrophysique, Géophysique et Océanographie. 2009.

[55] Simon-Pierre Gorza. *ELEC-H507 - Photonic Communication Systems*. Ecole Polytechnique de Bruxelles - Université Libre de Bruxelles. 2019.